

CONTROL OF FLOW STRUCTURE ON LOW SWEPT DELTA WING WITH
STEADY LEADING EDGE BLOWING

A THESIS SUBMITTED TO
THE GRADUATE SCHOOL OF NATURAL AND APPLIED SCIENCES
OF
MIDDLE EAST TECHNICAL UNIVERSITY

BY

MOHAMMADREZA ZHARFA

IN PARTIAL FULFILLMENT OF THE REQUIREMENTS
FOR
THE DEGREE OF MASTER OF SCIENCE
IN
MECHANICAL ENGINEERING

JANUARY 2015

Approval of the thesis:

**CONTROL OF FLOW STRUCTURE ON LOW SWEPT DELTA WING
WITH STEADY LEADING EDGE BLOWING**

submitted by **MOHAMMADREZA ZHARFA** in partial fulfillment of the requirements for the degree of **Master of Science in Mechanical Engineering Department, Middle East Technical University** by,

Prof. Dr. Gülbin Dural Ünver
Dean, Graduate School of **Natural and Applied Sciences**

Prof. Dr. Tuna Balkan
Head of Department, **Mechanical Engineering**

Assoc. Prof. Dr. Mehmet Metin Yavuz
Supervisor, **Mechanical Engineering Dept., METU**

Examining Committee Members:

Prof. Dr. Kahraman Albayrak
Mechanical Engineering Dept., METU

Assoc. Prof. Dr. Mehmet Metin Yavuz
Mechanical Engineering Dept., METU

Asst. Prof. Dr. Cüneyt Sert
Mechanical Engineering Dept., METU

Asst. Prof. Dr. Yiğit Yazıcıoğlu
Mechanical Engineering Dept., METU

Assoc. Prof. Dr. Oğuz Uzol
Aerospace Engineering Dept., METU

Date: 28.01.2015

I hereby declare that all information in this document has been obtained and presented in accordance with academic rules and ethical conduct. I also declare that, as required by these rules and conduct, I have fully cited and referenced all material and results that are not original to this work.

Name, Last name: MOHAMMADREZA ZHARFA

Signature:

ABSTRACT

CONTROL OF FLOW STRUCTURE ON LOW SWEEP DELTA WING WITH STAEADY LEADING EDGE BLOWING

Zharfa, Mohammadreza

M.S., Department of Mechanical Engineering

Supervisor: Assoc. Prof. Dr. Mehmet Metin Yavuz

January 2015, 86 pages

Unmanned Combat Air Vehicles (UCAVs), Unmanned Air Vehicles (UAVs) and Micro Air Vehicles are becoming extremely popular due to introducing many advantages to defense industry and aeronautical field. In line with this, the aerodynamics of these vehicles, which can be represented by simplified planforms, including delta wings, have been of considerable interest in recent years. This interest has stimulated investigation of the flow structure, as well as its control, on delta wings having low and moderate values of sweep angle. In the present study, the flow structure is characterized on a delta wing of low sweep 35° angle, which is subjected to steady leading edge blowing. The techniques of laser illuminated smoke visualization, laser Doppler anemometry (LDA), and surface pressure measurements are employed to investigate the steady and unsteady nature of the flow structure on delta wing, in relation to wing attack angle and Reynolds number. Using statistics and spectral analysis, unsteadiness of the flow

structure is studied in detail. Computer controlled air injection system is designed and applied to the delta wing used in flow characterization. Effect of steady blowing through the leading edges of the wing on flow structure is studied to delay or to prevent three-dimensional surface separation and possibly to reduce the buffeting on the wing surface. Effective blowing coefficient ranges for flow control are determined.

Keywords: Delta wing, Low sweep, Leading edge vortex, Vortex breakdown, Steady Leading Edge Blowing.

ÖZ

DÜŞÜK SÜPÜRME AÇILI DELTA KANAT ÜZERİNDEKİ AKIŞ YAPISININ HÜCUM KENARINDAN SABİT ÜFLEME İLE KONTROLÜ

Zharfa, Mohammadreza

Yüksek Lisans, Makina Mühendisliği Bölümü

Tez Yöneticisi: Doç. Dr. Mehmet Metin Yavuz

Ocak 2015, 86 sayfa

İnsansız Savaş Araçları, İnsansız Hava Araçları ve Mikro Hava Araçları, savunma sanayisi ve havacılık alanında çok sayıda avantaj sağladığı için son derece popüler hale gelmiştir. Bu doğrultuda, basitleştirilmiş platformlarla ifade edilen araçların aerodinamiği (delta kanat dahil olmak üzere) son yıllarda önemli ölçüde ilgi çekici olmaktadır. Bu ilgi, düşük ve orta dereceli süpürge açısına sahip delta kanatların akış yapısını ve akışın kontrolünü araştırmaya teşvik etmektedir. Bu çalışmada, sürekli hücum kenarı üflemeyle 35 derecelik düşük süpürme açılı delta kanadın akış yapısı incelenmiştir. Lazer aydınlatmalı akış görüntüleme, Lazer Doppler Anemometre ve yüzey basınç ölçümleri yöntemleri delta kanat üzerinde sürekli ve sürekli olmayan akış yapısını kanat hücum açısı ve Reynolds sayısına bağlı olarak incelemek için kullanılmıştır. Akış yapısının düzensizliği

üzerinde istatistiksel ve spektral analiz kullanılarak detaylı bir çalışma gerçekleştirilmiştir. Bilgisayar kontrollü hava enjeksiyon sistemi tasarlanıp delta kanadın akış karakterizasyonunda kullanılmıştır. 3 boyutlu yüzey ayrılmasını geciktirmek veya önlemek ve kanat yüzeyindeki sarsıntıları azaltmak için, kanadın hücum kenarı boyunca sabit üfleminin akış yapısına etkisi çalışılmıştır. Akış kontrolü için etkin üfleme katsayısı aralığı belirlenmiştir.

Anahtar kelimeler: Delta kanat, düşük süpürme açısı, Kanat ucu girdabı, Girdap kırınımı, sabit kanat ucu üfleme.

To My Parents

ACKNOWLEDGEMENTS

This thesis work is funded by TÜBİTAK (The Scientific and Technological Research Council of Turkey) with the project number 3501 – 111M732. I would like to express my sincere appreciation to the institution for the research assistantship I received during the study.

I would like to express my sincerest appreciation to all those people who has supported me either physically or morally throughout this study.

I am fully grateful to my supervisor Assoc. Prof. Dr. M. Metin Yavuz for his unique guidance, encouragement, support, criticism and invaluable supervision. I am also thankful to him for sharing his experiences and advices about real life with me. It was an honor for me to study with him throughout my graduate education.

I need to express my thanks to my friends: Osman Akdağ, İlhan Öztürk, Gökay Günacar and Ali Karakuş for their support in experiments. I have been very lucky to share unforgettable moments in Fluid Mechanics Lab with good friends.

I would like show my gratitude to the lab technicians Rahmi Ercan and Mehmet Özçiftçi for their invaluable help.

TABLE OF CONTENTS

ABSTRACT	v
ÖZ	vii
ACKNOWLEDGEMENTS	x
TABLE OF CONTENTS	xi
LIST OF TABLES	xiii
LIST OF FIGURES	xiv
NOMENCLATURE.....	xviii
CHAPTERS	
1. INTRODUCTION.....	1
1.1. Motivation	1
1.2. Aim of the Study	2
1.3. Literature Review	2
1.3.1. Flow structure over delta wings	3
1.3.2. Shear layer instabilities	5
1.3.3. Vortex breakdown	6
1.3.4. Flow Control	8
2. EXPERIMENTAL SETUP AND TECHNIQUES	21
2.1. Wind tunnel.....	21
2.1.1. Wind tunnel characterization	22
2.2. Wing model.....	23

2.3. Laser illuminated smoke flow visualization	25
2.4. Pressure measurements	26
2.5. Velocity measurements	28
2.6. Flow control setup	30
2.7. Analysis of experimental uncertainty	31
3. RESULTS AND DISCUSSION	43
3.1. Results in absence of flow control.....	43
3.1.1. Surface flow visualizations.....	43
3.1.2. Cross flow visualizations and pressure measurements.....	45
3.1.3. Spectral Analysis of velocity measurements	49
3.2. Results with flow control.....	51
3.2.1. Surface flow visualization	52
3.2.2. Pressure measurements.....	53
4. CONCLUSION AND FUTURE WORK	79
4.1. Conclusion	79
4.2. Recommendations for future work	81
REFERENCES	83

LIST OF TABLES

TABLES

Table 2-1 Relative uncertainty at different Reynolds numbers	33
--	----

LIST OF FIGURES

FIGURES

Figure 1-1 Schematic view of leading edge vortices over a delta wing [2]	13
Figure 1-2 Effect of increasing angle of attack on location of vortex core over slender delta wing [4]	13
Figure 1-3 Schematic streamline patterns over (a) nonslender and (b) slender delta wings [2]	14
Figure 1-4 Effect of Reynolds number on location of vortex core, $\Lambda = 50^\circ$ [7] ...	14
Figure 1-5 Instantaneous vortex structure over a $\Lambda = 50^\circ$ wing at $\alpha = 15^\circ$ [15]....	15
Figure 1-6 Vortex structure on a crossflow plane for a delta wing with $\Lambda = 50^\circ$ at $\alpha = 15^\circ$ upstream of breakdown location (a,b) and downstream of breakdown (c,d)[16]	15
Figure 1-7 Comparison of experimental flow visualization (left) and computational streakline (right) [16]	16
Figure 1-8 Vortex breakdown and flow reattachment borderline as function of sweep angle [2]	16
Figure 1-9 Leading edge control device: flaps [2]	17
Figure 1-10 Leading edge control device: variable sweep [32]	17
Figure 1-11 Tangential leading edge blowing with Coanada effect [37]	18
Figure 1-12 Time averaged near surface streamlines; $\alpha = 30^\circ$, $St = 1.5$ [1]	18
Figure 1-13 Optimal success of different blowing/suction methods from several studies in the literature [2]	19
Figure 1-14 Flow visualization without (up) and with (bottom) blowing at trailing edge [46]	19

Figure 1-15 Effect of trailing edge jet on flow structure near the wing surface [47]	20
Figure 2-1 Schematic view of wind tunnel	34
Figure 2-2 Experimental matrix	34
Figure 2-3 Average velocity and turbulence intensity of the flow field in test section with fan power	35
Figure 2-4 Uniformity of flow at low velocities along vertical and horizontal coordinates	35
Figure 2-5 Plan view and back view of the wing model showing pressure taps at three chordwise stations	36
Figure 2-6 CAD drawing of the fabricated wing model	36
Figure 2-7 Photograph of the fabricated wing model	37
Figure 2-8 Schematic view of the wing, mount and test section assembly with direction of velocity components	37
Figure 2-9 Experimental set-up of flow visualizations at cross flow planes (up) and a plane parallel to the leading edge vortex core (bottom)	38
Figure 2-10 The 16-channel pressure scanner and the cables connections.....	39
Figure 2-11 Basic working principle of LDA system [49]	39
Figure 2-12 Optical components of a LDA system [49].....	40
Figure 2-13 Schematic view of flow control system	40
Figure 2-14 Linear interrelation between voltage and outlet pressure of the pressure regulator	41
Figure 2-15 Pressure regulator (a) and its controlling analog module (b)	41
Figure 2-16 The inside wing path of injected air at $x/C = 0.16, 0.44$ and 0.66 (up) and blowing direction (bottom).....	42
Figure 3-1 Surface flow visualizations at different Reynolds numbers and at $\alpha =$ 3° angle of attack.....	55

Figure 3-2 Surface flow visualizations at different Reynolds numbers and at $\alpha = 4^\circ$ angle of attack	56
Figure 3-3 Surface flow visualizations at different Reynolds numbers and at $\alpha = 6^\circ$ angle of attack	57
Figure 3-4 Surface flow visualizations at different Reynolds numbers and at $\alpha = 8^\circ$ angle of attack	58
Figure 3-5 Surface flow visualizations at different Reynolds numbers and at $\alpha = 10^\circ$ angle of attack	59
Figure 3-6 Cross flow visualization, spanwise $-C_p$ and C_{pRMS} plots on $x/C = 0.32$ and $x/C = 0.77$ chordwise distances at $\alpha = 3^\circ$ angle of attack and different Reynolds numbers	60
Figure 3-7 Cross flow visualization, spanwise $-C_p$ and C_{pRMS} plots on $x/C = 0.32$ and $x/C = 0.77$ chordwise distances at $\alpha = 4^\circ$ angle of attack and different Reynolds numbers	61
Figure 3-8 Cross flow visualization, spanwise $-C_p$ and C_{pRMS} plots on $x/C = 0.32$ and $x/C = 0.77$ chordwise distances at $\alpha = 6^\circ$ angle of attack and different Reynolds numbers	62
Figure 3-9 Cross flow visualization, spanwise $-C_p$ and C_{pRMS} plots on $x/C = 0.32$ and $x/C = 0.77$ chordwise distances at $\alpha = 8^\circ$ angle of attack and different Reynolds numbers	63
Figure 3-10 Cross flow visualization, spanwise $-C_p$ and C_{pRMS} plots on $x/C = 0.32$ and $x/C = 0.77$ chordwise distances at $\alpha = 10^\circ$ angle of attack and different Reynolds numbers	64
Figure 3-11 Spectral analysis results of velocities measured at vortex core in x and z directions at $\alpha = 3^\circ$ angle of attack and $Re = 10^4$ (u-dir. on the left and w-dir. on the right).	65
Figure 3-12 Spectral analysis results of velocities measured at vortex core in x and z directions at $\alpha = 3^\circ$ angle of attack and $Re = 2 \times 10^4$ (u-dir. on the left and w-dir. on the right).	66
Figure 3-13 Spectral analysis results of velocities measured near the surface in x direction at $\alpha = 3^\circ$ angle of attack and $Re = 10^4$ (left) and $Re = 3.5 \times 10^4$ (right)	67
Figure 3-14 Spectral analysis results of velocities measured near the surface in z direction at $\alpha = 3^\circ$ angle of attack and $Re = 10^4$ (left) and $Re = 3.5 \times 10^4$ (right)	68

Figure 3-15 Spectral analysis results of velocities measured near the surface in x direction at $\alpha = 6^\circ$ angle of attack and $Re = 10^4$ (left) and $Re = 3.5 \times 10^4$ (right)	69
Figure 3-16 Spectral analysis results of velocities measured near the surface in z direction at $\alpha = 6^\circ$ angle of attack and $Re = 10^4$ (left) and $Re = 3.5 \times 10^4$ (right)	70
Figure 3-17 Surface flow visualization at $\alpha = 6^\circ$ angle of attack, $Re = 10^4$ and at different momentum coefficients	71
Figure 3-18 Surface flow visualization at $\alpha = 6^\circ$ angle of attack, $Re = 2 \times 10^4$ and at different momentum coefficients	72
Figure 3-19 Surface flow visualization at $\alpha = 6^\circ$ angle of attack, $Re = 3.5 \times 10^4$ and at different momentum coefficients	73
Figure 3-20 Surface flow visualization at $\alpha = 10^\circ$ angle of attack, $Re = 10^4$ and at different momentum coefficients	74
Figure 3-21 Surface flow visualization at $\alpha = 10^\circ$ angle of attack, $Re = 2 \times 10^4$ and at different momentum coefficients	75
Figure 3-22 Surface flow visualization at $\alpha = 10^\circ$ angle of attack, $Re = 3.5 \times 10^4$ and at different momentum coefficients	76
Figure 3-23 Spanwise $-C_p$ plots at $\alpha = 6^\circ$ angle of attack on chordwise distances of $x/C = 0.32$, 0.55 and 0.77 and different Reynolds numbers	77
Figure 3-24 Spanwise $-C_p$ plots at $\alpha = 10^\circ$ angle of attack on chordwise distances of $x/C = 0.32$, 0.55 and 0.77 and different Reynolds number	78

NOMENCLATURE

Λ	= sweep angle
c	= chord length
s	= semispan
\tilde{s}	= local semispan at pressure stations
α	= angle of attack
Re	= Reynolds number based on chord length
u_∞	= freestream velocity
u	= streamwise velocity
ω	= vertical velocity
x	= chordwise distance from wing apex
y	= spanwise distance from wing root
f	= frequency
St	= dimensionless frequency
p	= static pressure
\bar{p}	= average of the static pressure
p_∞	= static pressure of the flow
p_{dyn}	= dynamic pressure of the flow
$p_{R.M.S.}$	= rms value of the static pressure
C_p	= pressure coefficient
$C_{p, R.M.S.}$	= rms value of pressure coefficient
ρ	= density of the fluid
N	= number of samples in a measurement
C_μ	= momentum coefficient

CHAPTER 1

INTRODUCTION

1.1. Motivation

Due to recent increasing interest in Unmanned Combat Air Vehicles, Micro air vehicles (MAV) and unmanned air vehicles (UAV), many researchers focused on the enhancement of flow structure over low swept (non slender) delta wings which are simplified planforms of some of these air vehicles. These vehicles usually do not have regular aerodynamic control surfaces, and thus they suffer from flow instability and flight control problems. The flow structure over a low swept delta wing, having sweep angles less than 40° , significantly differs from the flow structures over high sweep angle (slender) delta wings. For slender delta wings, the literature was extensively built which includes the flow structures and their control in detail. In contrast to the slender wings, there are quite a few studies, which cover the aerodynamics, flow structure, and their control for wings having relatively low sweep angles. For these wings, the main recent research interests can be listed as: Interaction between leading edge vortices and boundary layer, leading edge vortex breakdown, surface flow separation, the effects of these structures on wing surface vibration, and flow control.

Flow structure on low sweep angle delta wings is expected to have unique flow patterns of leading edge vortices, vortex breakdown and stall. Very few studies have addressed the effects of Reynolds number and attack angles on flow

structure in detail. Thus, systematic studies for the characterization of flow structure on low swept wings are needed for broad range of Reynolds number and attack angles in terms of qualitative and quantitative representation of surface and cross flow structures. This would ultimately help to identify the regions of vortex breakdown and three-dimensional separation. In addition, practical and efficient flow control techniques can be sought to eliminate three-dimensional surface separation and to delay vortex breakdown. A very few studies investigated alternative flow control techniques which are applied to the flow control for low swept delta wings.

1.2. Aim of the Study

The purpose of this study is to characterize and to control the flow structure over a 35° swept delta wing by means of qualitative and quantitative flow measurement techniques. For the qualitative flow measurements, the laser illuminated smoke visualization is used, for the quantitative flow measurements, Laser Doppler Anemometry and surface pressure measurements are utilized. First the flow structure of a low swept wing is investigated in detail to figure out the critical attack angles for pre and post stall regimes along with the effect of Reynolds number on flow structure. Then, steady leading edge blowing is applied at different dimensionless momentum coefficients to understand the ultimate effect of blowing on flow structure particularly on three dimensional separation and vortex breakdown.

1.3. Literature Review

In literature, the most of the research efforts are devoted to high sweep angle delta wings, whereas the knowledge in flow structures and their control for low swept wings are very limited. In this chapter, although the flow structure of high and low

sweep angle wing are summarized and compared, the main attention was given to the flow structure and its control for low swept planforms.

1.3.1. Flow structure over delta wings

Flow structure over delta wing is concerned with separated flow from leading edge and the formation of free shear layer [1]. There is apparent difference between flow physics of slender and non-slender delta wings. These dissimilarities must be considered before any evaluation of probable matters in flow control.

The flow over slender delta wings is identified by two counter-rotating leading-edge vortices [2]. The formation of these vortices is because of revolving vortex sheets as shown in Figure 1-1. The separated flow arriving from leading edge of the wing makes the curved free shear layer. This flow then twirls into the vortex core. Since there are very low pressures at vortex core, the values of axial velocities are very high. This results in reproduction of extra suction called Vortex lift force. By increasing sweep angle of the wing the vortex lift contributes more [3]. Figure 1-2 schematically shows the effect of attack angle on the location of the vortex core. The vortex is placed just at the back of wing. By increasing the angle of attack, the location of the vortex moves toward the apex and the whole of the wing is covered by it [5]. Further increasing of attack angle leads to more strength vortex. Also, the vortex moves from the surface toward the wing centerline. At high angles of attack, vortex break-down occurs. Vortex break-down is the result of stagnation of jet like axial flow in the vortex core which expands very quickly [4]. Adverse pressure gradient is the reason of this stagnation. This abrupt expansion raise the levels of turbulence on the wing surface. At very high angles of attack, the location of vortex break-down is closer to the apex. As the break-down location reaches the apex the wing is called fully stalled [5]. Performed experimental and theoretical studies on vortex breakdown behavior [6] confirm that there are two dominant factors influencing on vortex

breakdown and its movement: swirl level and pressure gradient. The general difference between cross flow patterns of slender and non-slender delta wings is shown in Figure 1-3(a). For small angles of attack, the line at which primary reattachment occurs, is located near the midline of the leading-edge vortex. This point moves toward wing centerline as the angle of attack increases. At a specific incident, the flow reattaches at wing centerline [2]. For higher angles of attack, the flow does not reattach to the wing surface.

On the other hand, the shear layer separated from the leading edge of the wing, reattaches to the wing surface [6]. Low and moderate sweep angle delta wings are potentially considered more for controlling flow due to this shear layer reattachment. By increasing the angle of attack the reattachment place moves toward wing centerline. High levels of buffeting are identified as reattachment point meets wing centerline [7]. Like slender delta wings, the location of vortex break-down reaches the apex of the wing as value of incident increases [9]. For non-slender delta wings Vortex break-down is not the main reason of buffeting as it is in slender delta wings [7]. Vortex break-down does not limit the formation of lift force for non-slender delta wings [2]. It is possible that the shear layer reattaches even the break-down has approached the wing apex [2].

Dual vortex structure is an observable aspect of non-slender delta wings at low Reynolds numbers and very low incidents [4]. For a wing with 50° sweep angle, dual vortex structure has been noticed numerically [8] and experimentally [9, 10]. At low attack angles, the primary vortex is divided in to two parts by secondary vortex that makes apparent dual vortex structure. As the Reynolds number increases, the outer vortex undergoes break-down so much sooner than the inner vortex and this dual structure changes to single, larger-scale vortex. Dual vortex structure was not recognized on a 38.7° sweep angle at $\alpha = 7^\circ$ by Yaniktepe and Rockwell [11]. But, they distinguished two clearly different areas of high vortices downstream of breakdown [11]. Dissimilar to slender delta wings, non-slender delta wings are susceptible to change of Reynolds number at low angles of attack. Taylor and Gursul [7] found that effect of Reynolds number on flow structure

decreases for Reynolds higher than $Re = 3 \times 10^4$. Figure 1-4 presented by Taylor and Gursul [7], illustrates the comparison of some research results on span wise location of vortex core for different angles of attack and Reynolds numbers.

The unsteadiness of flow structure can arise from different types of physical mechanisms, including helical mode instabilities of vortex breakdown [11], which is characterized by Garg and Leibovich [12] for an internal flow. Gursul [13] also investigated for a flow over a highly swept delta wing. Other mechanisms were classified by Menke et al [14]. Study performed by Gordnier and Visbal [15] has yielded that periodic wandering of the vortex core can generate noticeable unsteadiness. This vortex wandering is result of interaction of vortices from leading edge and leeward wing surface [11].

There are very few research studies in literature, which involve force measurement for low sweep angle delta wings [16]. Non-slender delta wings have lower maximum lift coefficient and also lower stall angle compared to slender delta wings [17].

1.3.2. Shear layer instabilities

In this section the significant features of unsteady flow upstream of vortex break down are considered. The mean vortical flow structure is because of unsteady vortical flow which its structure gets evenly more complicated as the angle of attack increases. Figure 1-5 illustrates the unsteady vortex structure for $\alpha = 15^\circ$. At the upstream, there are some apparent substructures resembling a vortex outside of the shear layer generates the primary vortex. These vortices form in the arriving shear layer from leading edge of the wing and they are shed and convect downstream near primary vortex [16]. These shear layer features are wrapped by obvious vortex core detected the inside of the shear layer at upstream of the flow [15].

Contours of axial vorticity are shown in figure 1-6. Vortical structure generated in the leading edge shear layer can be identified in the figure 1-6 (a). An unsteady secondary flow with a reverse vorticity expelled from the wing surface appears along with shear layer instability. This sudden reaction of secondary flow originates from the interaction between the leading edge vortex and the surface boundary layer flow [15]. Unsteady shear layer and the secondary flow mentioned above are the reasons of the vortex core to wander significantly. The location of the vortex core change in an elliptical way with the same rotation direction of the vortex swirl. This unsteady behavior of the vortex core generates high values of fluctuating kinetic energy, k , in the vortex core before the occurrence of vortex breakdown [16], Figure 1-6 (b).

For delta wings with sweep angle of 45° and 60° , Grad-el-Hak and Black Welder [18] observed that for low Reynolds numbers, vortex sheet originating from leading edge rolls up periodically into distinct sub structures containing vortices. They linked this behavior to inviscid Kelvin-Helmholtz type of the shear layer instability. Another more recent experimental study was performed for $\Lambda = 38.7^\circ$ by Yavuz et al [19]. They presented that “regions of average vorticity indicate the existence of a co-rotating pattern of small scale vorticity concentration”. PIV measurements performed by Yaniktepe and Rockwell [15] for a delta wing with sweep angle of 38.7° yielded that dominant spectral peak increases by moving toward leading edge of the wing.

1.3.3. Vortex breakdown

A useful method of studying vortex breakdown over delta wings is visualization of streakline by means of releasing smoke or dye in the vortex prior to vortex breakdown location. This technique has been succeeded in exhibiting the special specifics of the vortex breakdown over slender delta wings [20]. Indeed, for non-slender delta wings extra efforts are needed to understand streakline visualizations because of different behavior vortex breakdown over these wings.

Spiral type vortex breakdown usually occurs over slender delta wings [6], therefore, the location of breakdown is recognized by the vortex core spiraling in the reverse direction of the vortex rotation. Studies about non-slender delta wings [7, 11], in contrast to slender delta wings, present that the shape of vortex breakdown is conical. The jet like axial flow gradually becomes wake like flow after vortex breaking down. Due to spiral behavior of vortex breakdown over slender delta wings, distinct spectral peaks are recognized in velocity fluctuations [4]. On the other hand, non-slender delta wings have tendency of broader frequency spectrum because of gradual behavior of vortex breakdown over these wings.

Figure 1-7 illustrates the comparisons of visualized streaklines for experimental observation [11] at $\alpha = 7^\circ$, $\Lambda = 39^\circ$ and numerical visualization [17] at $\alpha = 15^\circ$, $\Lambda = 50^\circ$. Apparent differences are obvious between these streaklines and the slender delta wings vortex breakdown structures. Yaniktepe and Rockwell [11] recognized three well-defined zones in the occurrence of vortex breakdown. A wavy small scale motion of vortex core is clearly identical in the region I. Gordnier and Visbal [15] attributed this helix motion to the shear layer instabilities. At region II, small scale bubble is noticed or the vortex core becomes thicker. At pith off area the vortex again thins. At region III, sudden expansion of vortex called vortex breakdown takes place. As a result, diffused particles spread out over a vast area wrapping half of the wing. Both Ol and Gharib [21] and Taylor et al [22] presented that the location of breakdown demonstrates dominant fluctuations. Contrary to more slender delta wings, high amount of fluctuations were detected [23]. Visualizing the vortex structure on a vertical plane through vortex core can be more helpful in spotting the location of onset of vortex breakdown [16].

1.3.4. Flow Control

Different types of techniques have been conducted to control flow separation, vortex formation, flow reattachment, vortex breakdown and vortex instabilities [2]. This section is not a thorough review, but it provides insight in to the aspects of approaching the phenomena mentioned above. Vortex control using different methods lead to identifiable changes in aerodynamic characteristics of delta wings specially lift and drag coefficients [25].

Polhamus [26] found that as the sweep angle decreases, the portion of vortex lift to the total lift reduces. For non-slender delta wings, vortex breakdown occurs even at low angles of attack. There is not any clear connection between vortex breakdown existence and the change in the value of lift force coefficient. Therefore, vortex breakdown may not be an obstacle phenomenon for lift force being generated over non-slender delta wings. By contrast, in any flow control approach, flow reattachment is of considerable importance. Figure 1-8 shows the reattachment line based on flow visualization observation [7] and also stall angles from refs. [27, 16]. Since no theoretical or computational predictions exist for angle reattachment, estimation of this angle is shown from performed experiments. Differences of flow behavior over slender and non-slender delta wings determine the effectiveness of each flow control technique.

Different types of control surfaces [38] have been used to control the leading-edge vortices. One type of these devices called leading edge flap, is shown in figure 1-9 [2]. Leading edge flaps have been found of use to influence the strength and structure of leading edge vortices. Downward deflected leading edge flaps improve the lift-to-drag ratio and decrease drag [29], whereas, upward deflected flaps increase lift as well as drag. This method can be used for landing or aerodynamic maneuvers. Spedding et al [30] found that upward deflected flaps can generate higher vortex lift for low angles of attack. However, flaps may cause moving of vortex breakdown location toward upstream and closer to the wing tip [31]. Yang and Gursul [32] used a variable sweep angle delta wing shown in Figure 1-10, to control leading edge vortices and vortex breakdown. Since the

relation between breakdown and sweep angle is monotonic, this method is proper for feedback control purposes.

Blowing and suction applied from different locations of a delta wing are common methods of controlling the leading edge vortices and vortex breakdown. Most common used techniques include: a) leading edge suction or blowing. b) Blowing from small aspect ratio jets along the vortex core or parallel to leading edge. c) Trailing edge blowing. Leading edge vortices arise from the line along separation from leading edge of the delta wing. Consequently, control of shear layer has influence on behavior of vortices and location of vortex breakdown.

Celik and Roberts [33] applied blowing in outward direction. In this type of blowing, the flow structure is similar to an inclined jet in cross-flow. Jet vortices may combine with leading edge vortices [33]. Margaris and Gursul [34] applied tip blowing on high ratio wing. Similar flow patterns were observed because of complex interaction of jet and wing vortices.

Generally, blowing increases the level of circulation. In a similar way, for a delta wing with sweep angle of 60° [35], leading edge vortex becomes stronger with the flux of jet momentum. The raise in level of vortex strength leads to lift enhancement at low angles of attack. However, at moderate angles of attack, it causes vortex breakdown which results in lift reduction [33]. Wood and Roberts [36] performed tangential leading edge blowing on a 60° sweep angle delta wing. They indicated that controlling primary separation give rise to major influences on the vortex flow up to angles of attack of 60° .

Greenwell and Wood [37] applied “Coanda effect” in leading edge blowing, as shown in figure 1-11. At low incidences, completely attached flow was observed in the absence of leading edge vortices. Effect of blowing on strength of vortex is not clear at moderate incidences. However, it can be said that interaction of phenomena such as vortex strength, distance of vortex from wing surface and vortex from wing surface and vortex breakdown location can form significant rolling moment. The effect of blowing on normal force coefficient at low and

moderate incidences is not considerable. Lift enhancement is noticed in post-stall region. This is because of the fact that the separated shear layer is energized by the leading edge blowing.

Gu et al. [39] studied on effects of suction, blowing and alternate suction-blowing applied on a rounded leading edge delta wing. The direction of suction and blowing was tangent to leading edge of the wing. They investigated the change in the structure of vortex break down and stall. They found that the location of vortex break down can be changed suddenly by alternate suction-blowing with period of alteration which is about convective time scale (chord/U_∞). No change in the value of lift and drag were observed. But, they assumed that there would be rise in lift to drag ratio due to the change in vortex break down location.

Williams et al. [1] investigated effects of unsteady blowing at the leading edge of a 50° swept angle delta wing by utilization of pressure measurements and particle image velocimetry measurements. Considerable delay in stall was observed. Also, increase in the upper surface suction force was detected. They discovered an optimal momentum coefficient for each angle of attack. Applying higher momentum coefficients than optimal one had negligible effect. For the post stall region, the optimal momentum coefficient was increased by increasing the angle of attack. Velocity measurements showed that flow reattachment is developed by the effect of leading edge blowing. Figure 1-12 shows the time averaged near surface streamlines for $\alpha = 30^\circ$. In the absence flow control, a large region of reversed flow is apparent. By conducting blowing excitation, flow reattaches near wing center line. This surface flow patterns resembles the pattern for lower angle of attack before stall presented by Taylor et al. [7]. A novel technique of blowing called “recessed angled spanwise blowing” was performed by Johari et al. [40]. They presented that blowing from the ports downstream of a no-control vortex breakdown, delayed the vortex breakdown, whereas blowing from upstream prompted the break down.

Suction eliminates vorticity shed from the leading edge. For this reason, strength and swirl level is reduced by suction. McCormick and Gursul [40] observed alteration in

location of shear layer and vortex by implementation of suction. Detailed measurements [40] also yielded that suction reduced maximum swirl angle and vorticity in the core. This reduction results in moving of location of vortex breakdown toward downstream. Of particular importance is that thick rounded leading edges are not needed in suction technique, therefore without use of Coanda effect control of vortices is achievable.

Figure 1-13 presented by Gursul et al. [2] shows the effectiveness of different blowing suction techniques from various studies published in the literature. The vertical axis represents the effectiveness where Δx_{bd} is change in the location of vortex breakdown, c is the length of wing chord and C_μ is the momentum coefficient. It is evident that blowing along the vortex core is the most dominant technique to postpone vortex breakdown. It can be concluded that effect of pressure gradient on vortex core is significant.

Many studies have been devoted to investigation of effect of trailing edge blowing on the structure of flow over delta wings. Trailing edge blowing refines the external pressure gradient and postpones vortex breakdown. Figure 1-14 illustrates conductive consequence of a trailing-edge jet [46]. The effectiveness of trailing edge technique relies on the sweep angle of delta wing [47]. Delaying vortex break down is more difficult by decreasing wing sweep angle. Vortex breakdown exists for low sweep angle delta wings even at low incidences. The breakdown method is less efficient for non-slender delta wings because of unfavorable external pressure gradient over these wings. The result of trailing edge blowing is considerable despite the fact that it is difficult to delay vortex breakdown over non-slender delta wings. Velocity and near surface streamlines of a wing with $\Lambda = 50^\circ$ at $\alpha = 20^\circ$ are shown in Figure 1-15 [47]. The flow pattern with reattachment near wing centerline has been changed with blowing. Two distinct reattachment lines are observable. Due to experiments largest change of lift force is noticed around the stall angle [47]. Yavuz and Rockwell [24] investigated trailing-edge controlled flow structure on delta wing with $\Lambda = 35^\circ$. They presented that “even though the jet blowing is at the trailing, it has a

remarkable, global influence on the surface patterns located well up stream; at high angle of attack, it leads to eradication of large-scale, three dimensional separation in the vicinity of the apex.”

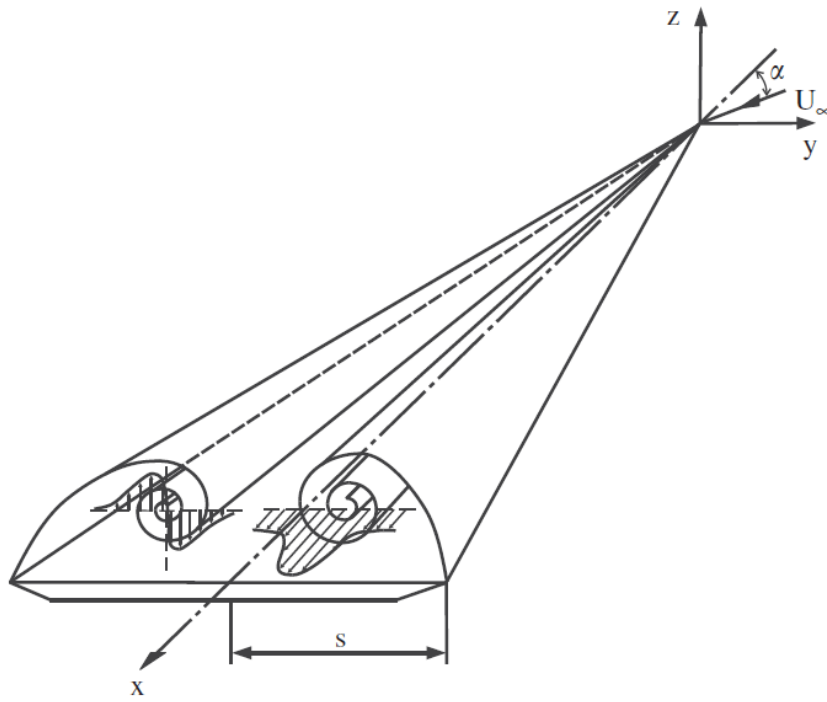


Figure 1-1 Schematic view of leading edge vortices over a delta wing [2]

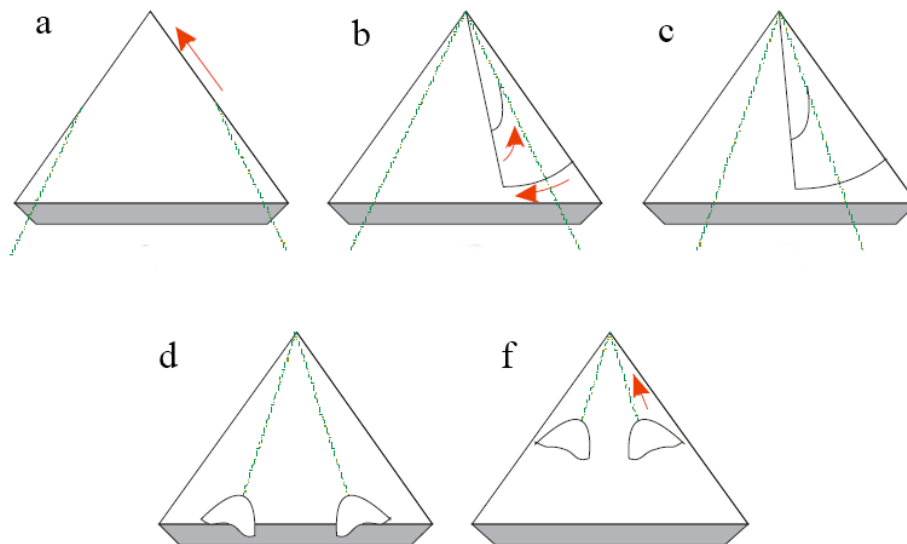


Figure 1-2 Effect of increasing angle of attack on location of vortex core over slender delta wing [4]

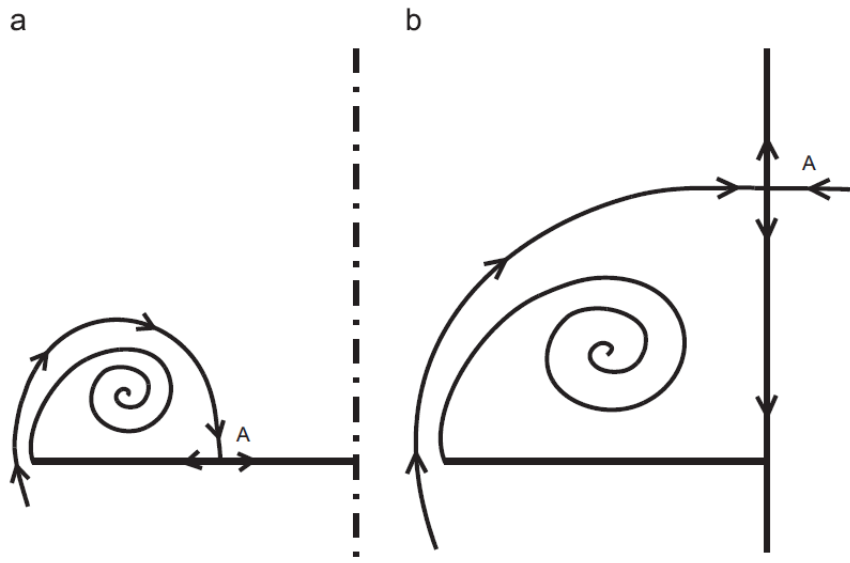


Figure 1-3 Schematic streamline patterns over (a) nonslender and (b) slender delta wings [2]

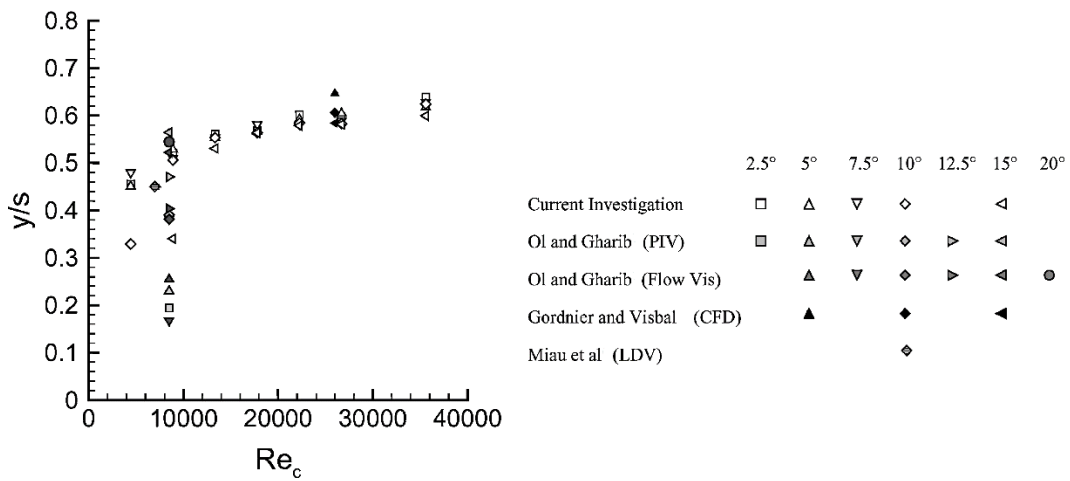


Figure 1-4 Effect of Reynolds number on location of vortex core, $A = 50^\circ$ [7]

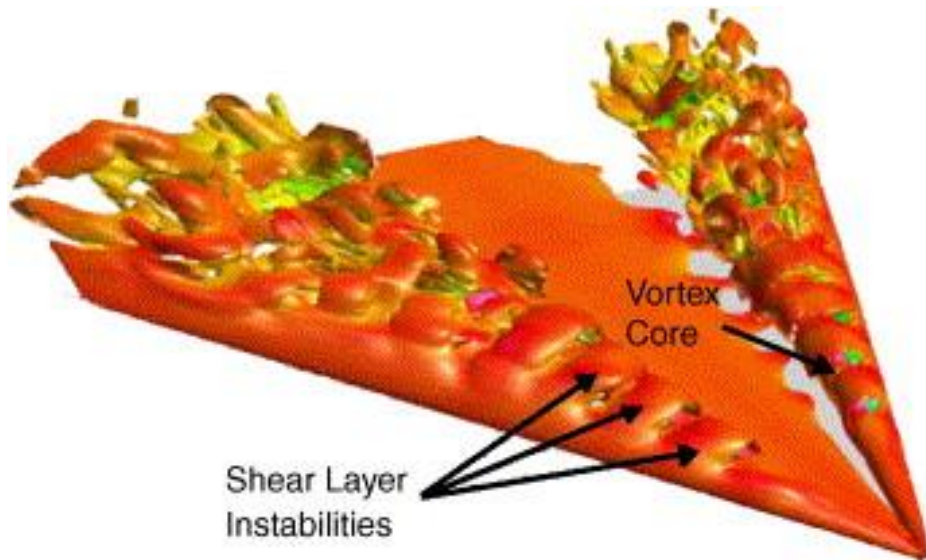


Figure 1-5 Instantaneous vortex structure over a $\Lambda = 50^\circ$ wing at $\alpha = 15^\circ$ [15]

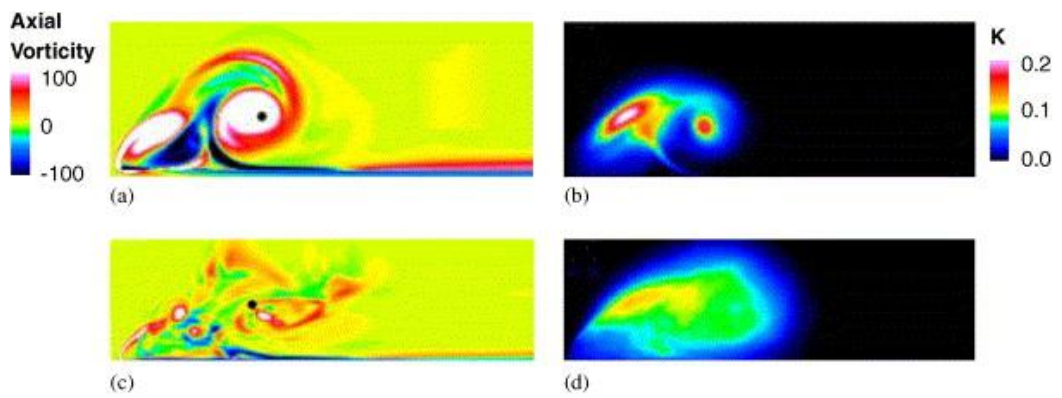


Figure 1-6 Vortex structure on a crossflow plane for a delta wing with $\Lambda = 50^\circ$ at $\alpha = 15^\circ$ upstream of breakdown location (a,b) and downstream of breakdown (c,d)[16]

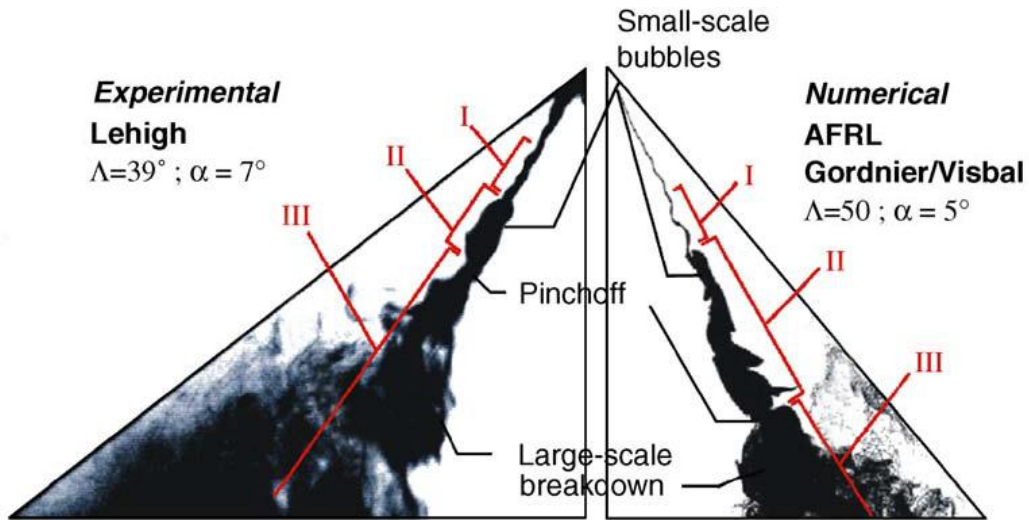


Figure 1-7 Comparison of experimental flow visualization (left) and computational streakline (right) [16]

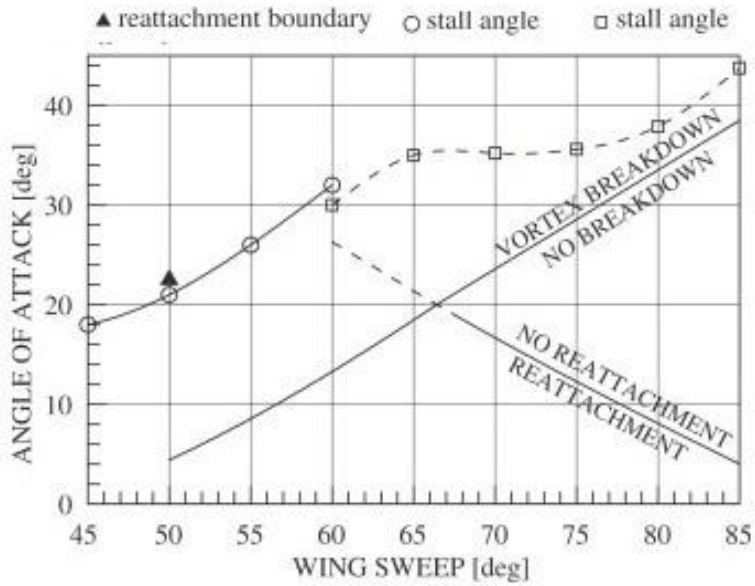


Figure 1-8 Vortex breakdown and flow reattachment borderline as function of sweep angle [2]

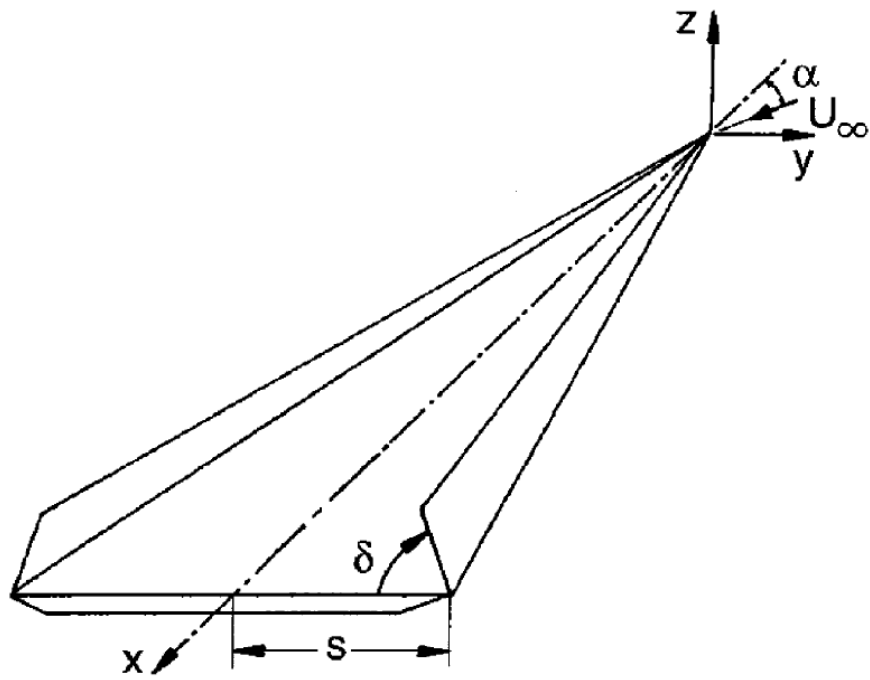


Figure 1-9 Leading edge control device: flaps [2]

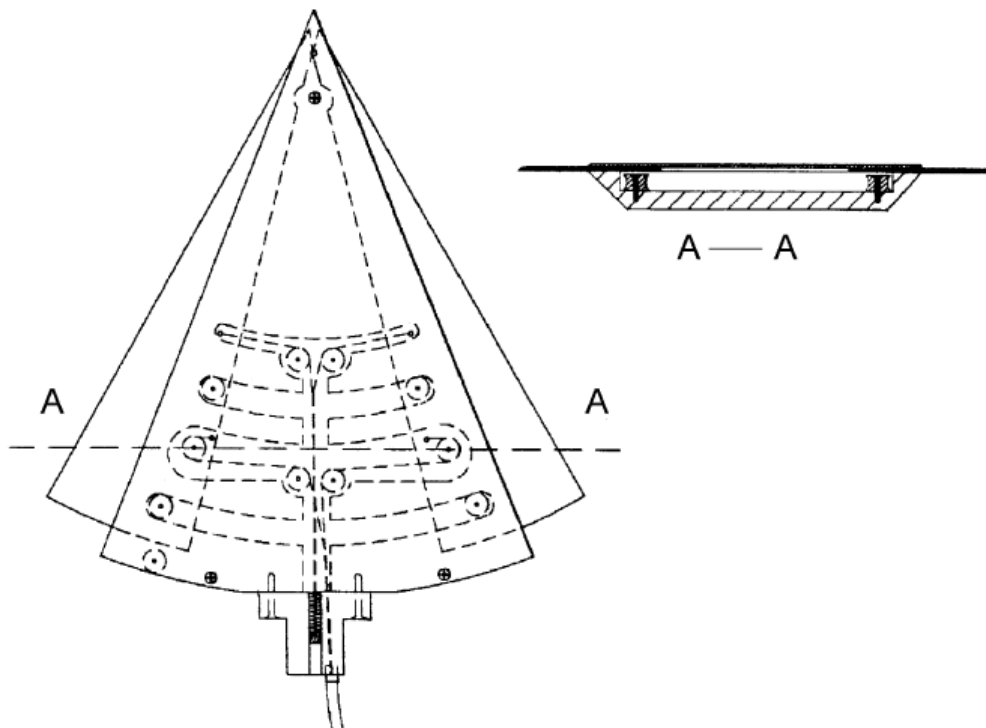


Figure 1-10 Leading edge control device: variable sweep [32]

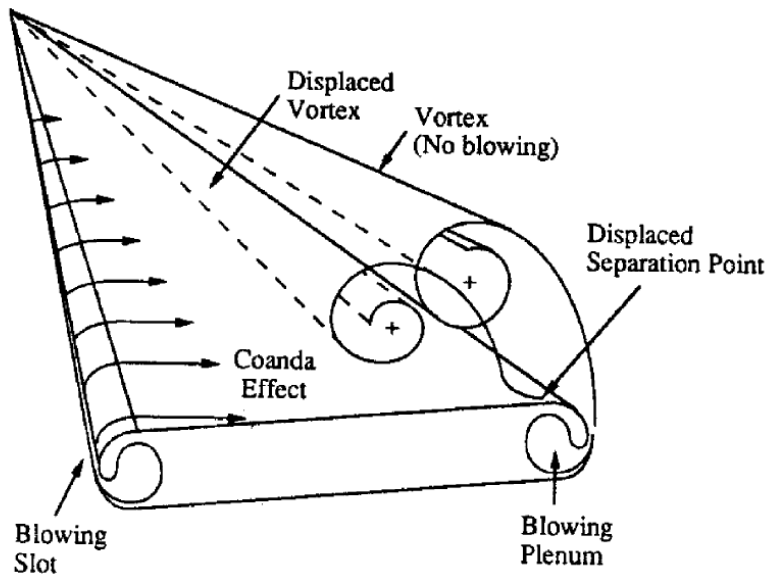


Figure 1-11 Tangential leading edge blowing with Coanada effect [37]

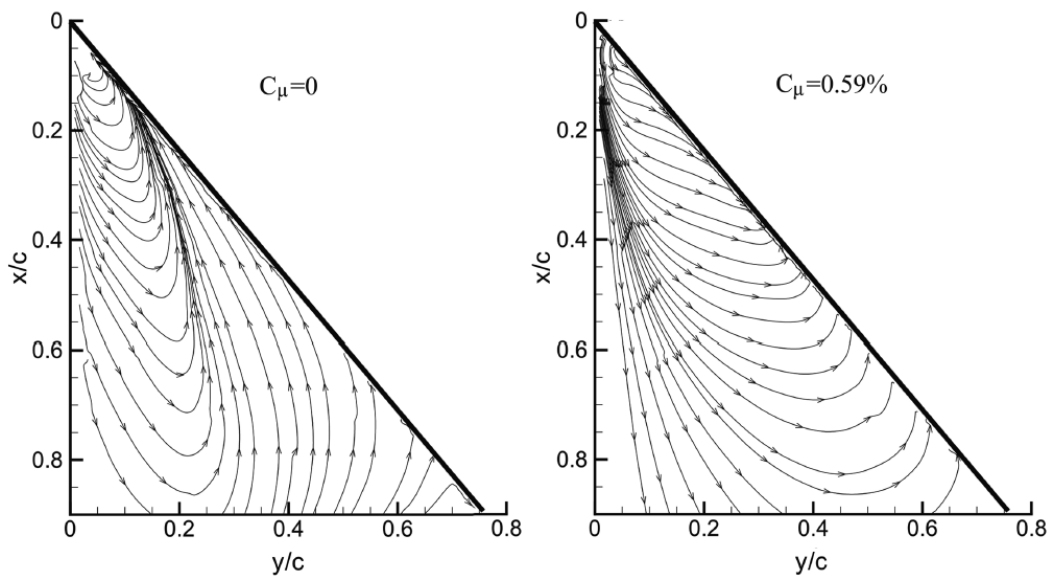


Figure 1-12 Time averaged near surface streamlines; $\alpha = 30^\circ$, $St = 1.5$ [1]

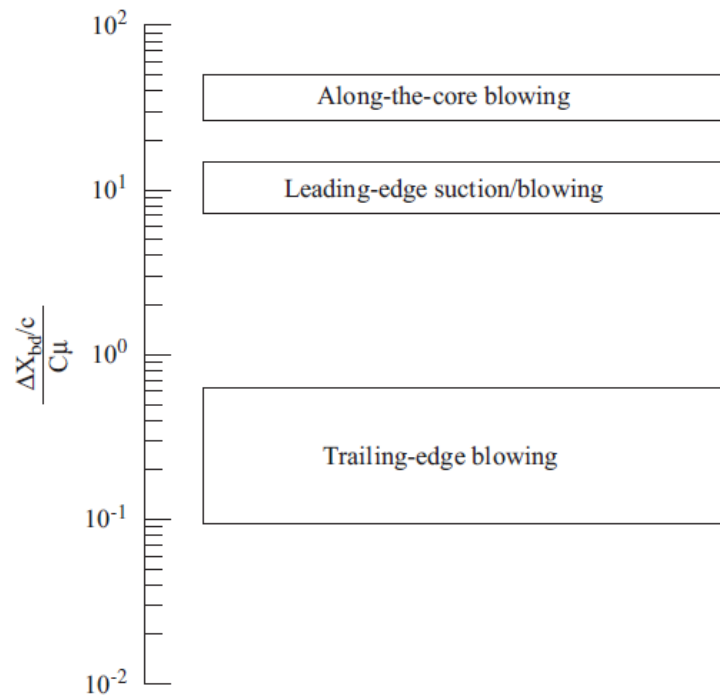


Figure 1-13 Optimal success of different blowing/suction methods from several studies in the literature [2]

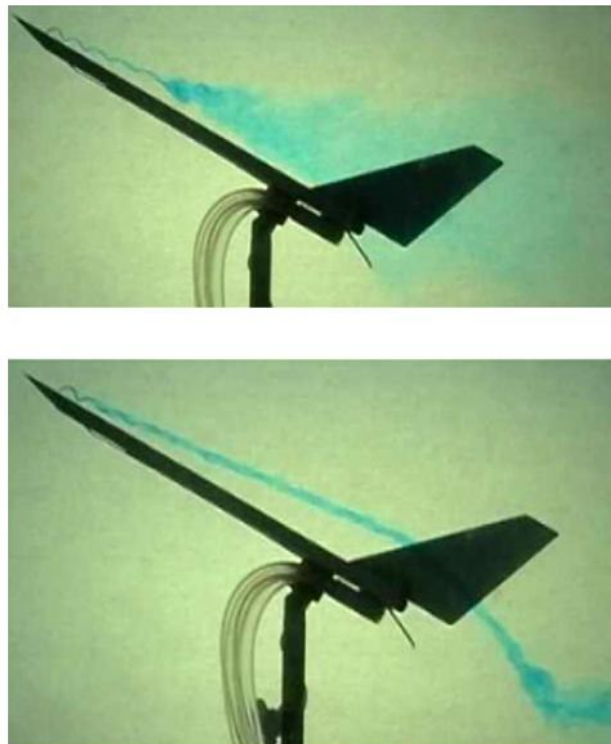


Figure 1-14 Flow visualization without (up) and with (bottom) blowing at trailing edge [46]

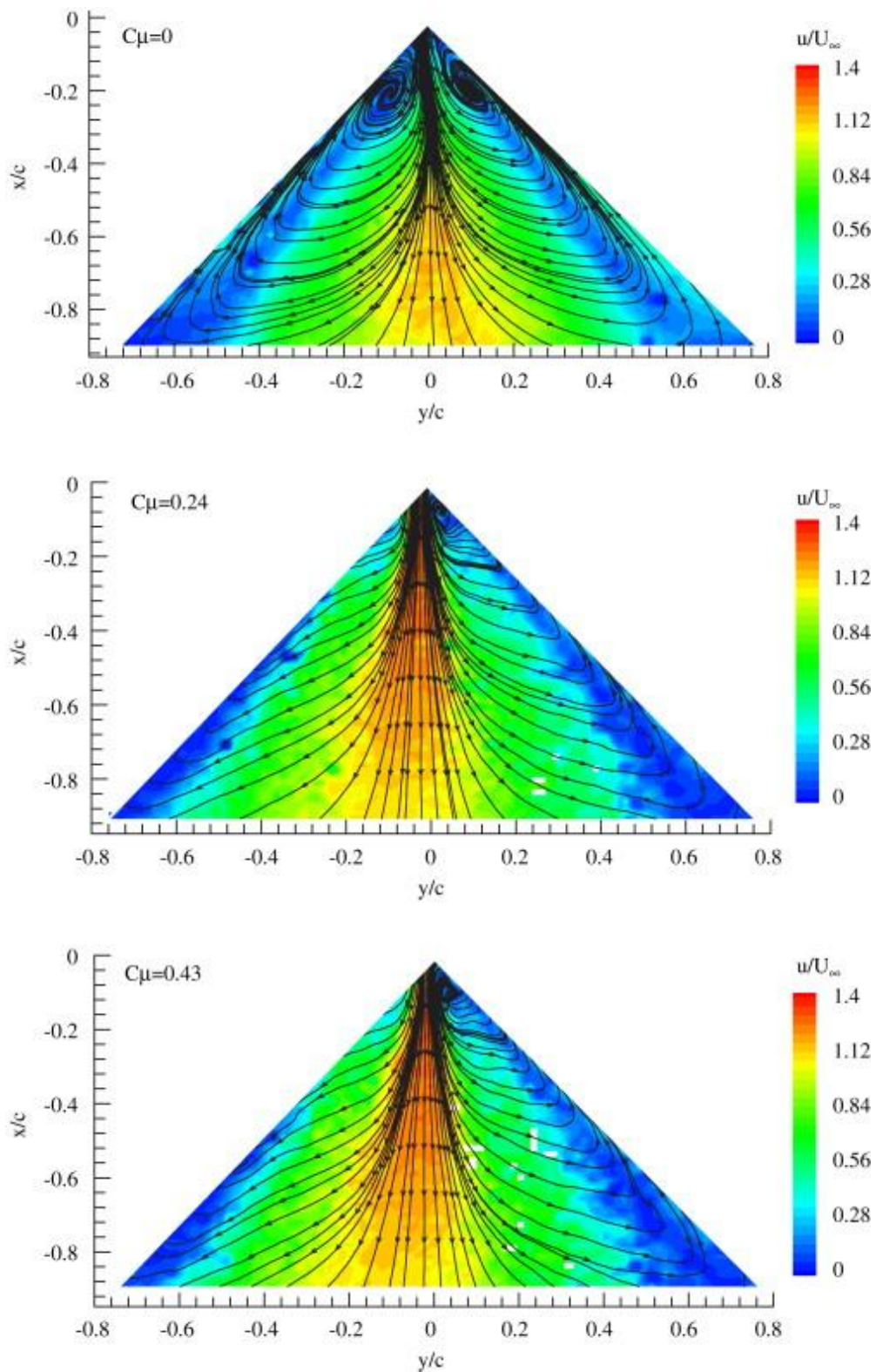


Figure 1-15 Effect of trailing edge jet on flow structure near the wing surface [47]

CHAPTER 2

EXPERIMENTAL SETUP AND TECHNIQUES

2.1. Wind tunnel

Experiments were conducted in a low speed, suction type, and open circuit wind tunnel located in Fluids Mechanics Laboratory of Mechanical Engineering Department at Middle East Technical University. This type of a wind tunnel is composed of five main parts including; settling chamber, contraction, test section, diffuser and drive section (fan), which is schematically illustrated in Figure 2-1.

Air enters to the tunnel through two inlet sections. The total length of entrance section is 2700 mm. A honeycomb and three fine grids are utilized in this section in order to obtain a more uniform flow field and to reduce the turbulence intensity in the test section.

Contraction part, which is located between the settling chamber and the test section, causes significant area reduction, which in turn results significant increase in free stream velocity before entering to the test section. The contraction part is 2000 mm long and has a contraction ratio of 8:1.

Due to optical transparency requirement in laser illuminated flow visualization technique, a fully transparent, Plexiglas, test section has been constructed with the dimensions of 750 x 510 x 2000 mm. The test section has access through the side,

bottom, and top walls, which allows easy working environment for setting up the experiments.

Diffuser is a part of wind tunnel in which relatively high speed air leaving test section gradually expands. The reduction in the pressure of flow field leads to reduction of the power required to drive the tunnel facility. The total length of the diffuser is 7300 mm and the cone angle is 3°. A frequency controlled axial fan assembled at the exit part of the wind tunnel was used via a remote control unit to obtain desired free stream velocity in the test section.

The desired Reynolds numbers based on chord of the wing correspond to free stream velocities range from 1 m/s to 15 m/s. Equation 2-1 is used to calculate Reynolds numbers.

$$Re = \frac{U_{\infty} C}{\nu} \quad (2-1)$$

Where U_{∞} is free stream velocity. C is the wing chord and ν is Kinematic viscosity.

The maximum free stream velocity can be obtained in the test section is 30 m/s. The experiments of the study were performed at different angles of attack and wide range of Reynolds numbers. The experimental matrix is shown in Figure 2-2.

2.1.1. Wind tunnel characterization

The velocity measurements in the test section were performed at different fan powers directly by Laser Doppler Anemometry (LDA) and by Pitot-static tube pressure measurements using both inclined manometer and pressure scanner to calibrate the wind tunnel before doing any experiment. For the calculation of velocities from the dynamic pressures obtained from Pitot-static tube, the ambient temperature, humidity, and the geographic elevation of the lab were taken into account. In addition, LDA technique was used to determine the velocities in the

wind tunnel, which showed 3 % variation in measured velocities compared to pitot tube measurements. Therefore, averaging of velocity values obtained from LDA and pressure measurements for the corresponding fan powers was performed to determine the velocity values in the test section. Considering the fan power and the corresponding velocities in the test section, the calibration curve was found to be linear for almost the whole velocity range. Average velocity vs. fan power is shown in Figure 2-3. In addition, LDA measurements provided turbulence intensity values, which are also illustrated in Figure 2-3. As seen in this figure, the turbulence intensity of the test section hardly exceeds 1 %. Therefore, it can be said that turbulence intensity in the test section of the wind tunnel is less than 1 % particularly within the velocity ranges, which the experiments are performed.

To complete the characterization of the wind tunnel, the uniformity of the free stream velocity in test section was also checked. The test section was traced at different free stream velocity conditions along the vertical and horizontal centerlines of the cross-section. A sample result of this measurement is shown in Figure 2-4. The maximum difference in velocity at the points indicated in the figure does not exceed 5.7 % at the lowest free stream velocity where the maximum percent deviations are obtained.

2.2. Wing model

A delta wing with sweep angle of $\Lambda=35^\circ$ has been investigated. The wing has a chord of 105 mm and span of 300 mm. The thickness of the wing is 15 mm. The material used in manufacturing the wing is fine polyamide PA2200. The bevel angle of the leading edge of the wing is 45° . Figure 2-5 illustrates the sketch of the wing from three different views. The blockage ratio has been considered in determining the dimensions of the wing. The maximum blockage ratio is at the highest attack angle of $\alpha = 10^\circ$ and does not exceed 0.7 %. The quantity and locations of pressure tabs are determined to achieve high resolution in pressure measurements. The diameter of the pressure tabs at the surface of the wing is 0.5

mm, which is the minimum value that can be obtained during manufacturing process of the wing without any issues. With preliminary test, it is also confirmed that the size of diameter of the pressure tab does not cause notable disturbance in the flow structure over the wing surface if it is in the range of 0.5 mm to 1 mm. The designed wing has 40 pressure tabs which are symmetrically distributed to three spanwise stations located at chordwise distances of $x/C = 0.32, 0.55$ and 0.77 as seen in Figure 2-5.

The process of flow visualization using smoke demands injection holes on the wing surface to introduce the smoke. The purpose of these holes is to create streaklines to detect leading edge vortices and visualize flow structures over the wing.

Due to complicated structure of the designed wing as shown in Figure 2-6, it was not possible to manufacture it by traditional materials and techniques. 3-D printing (Rapid prototyping) seemed to be the proper method for manufacturing of the wing. Quite successful wings were fabricated using 3-D printing considering the quality of the surfaces, the dimensional tolerances, and structural integrity. The picture of the wing used in the experiments is shown in Figure 2-7.

Rapid prototyping can be described as group of techniques used in fabrication of scale model of a part or assembly using three dimensional computer aided design (CAD) data in a very short period of time. Rapid prototyping has also been mentioned as solid free surface form manufacturing, computer automated manufacturing and layered manufacturing. RP models can be used for testing like an airfoil shaped body put in to a wind tunnel. Rapid prototyping technique decreases costly mistakes and development time by allowing corrections to a product to be made early in the process. At this method the part is divided in to small divisions, which are fabricated layer by layer. There are different available RP techniques such as Stereolithography, Laser Sintering, Fused Deposition Modeling and Solid Ground Curing. The investigated model in this study is fabricated by Laser Sintering based Rapid Prototyping machine branded EOSINT P380.

A mount mechanism was designed and manufactured to maintain stability of the wing in the test section without disturbing the upstream flow. With the designed wing mount, required angle of attack, yaw and roll angles can easily be applied. The wing, mount and test section assembly is shown in Figure 2-8.

2.3. Laser illuminated smoke flow visualization

Flow visualization is relatively simple and inexpensive method, to obtain general flow structure. For flow visualization, it is essential to feed traceable materials including but not limited to vapor, bubble, oil, smoke, and dye. Tropea et al. [48] stated that those substances are not buoyant tracers because of significant density difference with air, but the buoyancy effect can be neglected since the particles are in the order of 1 μm in diameter.

Using vaporized oils is a common approach in laboratory experiments and most commercial smoke generators use this concept. The smoke generator used in this study is based on the vaporizing of kerosene (paraffin) mist. It is made up of a heating element and a device that mixes the mist with pressurized carbon dioxide. The flow rate of smoke can be set by changing the pressure of carbon dioxide gas enters to the smoke generator.

A great amount of light is needed to brighten the smoke introduced to the flow field. An illuminated plane sheet should be used to visualize particular flow structures like wakes, vortices and separation, and this can be performed by a laser light sheet generated by a laser source and optics. A Diode-pumped solid-state (DPSS) green laser with 532 nm wavelength and 400 mW power output was used. The laser beam was converted to laser sheet by means of a cylindrical lens. Two different flow visualizations, cross flow and surface flow, were performed, where the light sheet plane was located perpendicular to the test section at $x/C = 0.32$, 0.55 and 0.77 and parallel to leading edge vortices, respectively. C represents the chord of the wing. The images were captured by DSLR camera. For cross flow visualization, a mirror was located further downstream of the wing with an angle

of 45° to free stream to take cross flow pictures by the camera located outside of the test section. Preliminary tests were performed to ensure that the located mirror has no influence upstream in the flow over the wing. For surface flow visualization the camera was located under the test section. The sketches of experimental set up for cross flow and surface flow visualizations are shown in Figure 2-9.

2.4. Pressure measurements

Pressure measurements were carried out by using a 16-channel pressure scanner which is Netscanner 9116 Intelligent and integrates 16 silicon piezoresistive pressure sensors with a range of 0 – 2.5 kPa. The device is factory calibrated over the identical pressure and temperature spans and is ready to use. The calibration data is stored in the EEPROM (Electrically Erasable Programmable Read-Only Memory) of each transducer. Microprocessor of the device compensates transducer outputs for offset, nonlinearity, sensitivity and thermal effects before transferring data to the computer. The compensation is conducted by utilizing the calibration data and the temperature data acquired from temperature sensors incorporate with pressure sensors. The manufacturer of this device guarantees the measurement resolution of ± 0.003 % FS (full scale), ± 0.15 % FS accuracy for values that are less than 17 kPa including the combined errors due to non-linearity, hysteresis and non-repeatability.

As stated earlier, there were 40 pressure tabs on the wing surface. The measurements were applied in 3 sets to cover all pressure tabs. A couple of experiments were conducted using all the pressure tabs where a complete symmetrical pattern was observed. Once a complete symmetrical pattern was ensured, the rest of the measurements were performed using the pressure tabs located only one side of the wing where two sets of measurements were enough to acquire data from those pressure tabs. The samples were obtained at 500 Hz and

the data was acquired for 10 seconds. The pressure scanner and the connections to the wing are shown in Figure 2-10.

Dimensionless pressure coefficients, C_p , using Equation 2-2 are calculated from pressure data of each pressure tab in order to display the relative pressure distribution on the surface of the wing at three different spanwise locations. C_p values were plotted as $-C_p$ distribution on the surface of the wing at the following results sections. The calculations of root mean square (RMS) for pressure fluctuations and corresponding C_p fluctuations are shown in Equation 2-3 and 2-4, which provide information about unsteady variation of pressure distribution on the wing surface.

$$C_p = \frac{p-p_\infty}{\frac{1}{2}\rho u_\infty^2} = \frac{p-p_\infty}{p_{dyn.}} = \frac{\Delta p}{p_{dyn.}} \quad (2-2)$$

p : measured pressure

p_∞ : static pressure of the flow

$p_{dyn.}$: Dynamic pressure of the flow

ρ : density of the fluid

u_∞ : free stream velocity

$$p_{R.M.S} = \sqrt{\frac{\sum_{i=1}^N [(p_i - \bar{p})^2]}{N}} \quad (2-3)$$

N : number of samples in the measurement

p : measured pressure at an instant

\bar{p} : Average of the measured pressure values

$$C_{p,R.M.S.} = \frac{p - p_\infty \pm p_{R.M.S.}}{p_{dyn.}} = C_p \pm \frac{p_{R.M.S.}}{p_{dyn.}} = C_p \pm \frac{\sqrt{\frac{\sum_{i=1}^N [(p_i - \bar{p})^2]}{N}}}{p_{dyn.}} \quad (2-4)$$

2.5. Velocity measurements

Laser Doppler anemometry (LDA) is a non-intrusive, pointwise velocity measurement technique that has extensive applications including laminar and turbulent flows, subsonic and supersonic flows, and combustion. The technique gets its name from Doppler effect known as the change in the frequency of a wave while there is a relative velocity between an observer and the source. This technique requires seeding particles that scatter light which is collected by photo detector for processing to obtain the velocity measurement using the Doppler effect. There is no need for calibration and it provides absolute velocity measurement. The basic configuration of an LDA system is composed of:

- A continuous wave laser.
- Transferring optics including beam splitter and focusing lenses.
- Receiving lenses consist of focusing lenses, interface filter and a photo detector.
- A signal conditioner and a signal processor. [49]

Basic working principle of an ordinary LDA system and its optical parts are illustrated in Figures 2-11 and 2-12.

An argon-ion laser with the power of 750 mW was used to generate continuous laser beam. A beam splitter considered as an optical unit has the ability to split the laser beam into three different wavelengths and creates two laser beams at each wavelength. One pair of fiber manipulators is installed for each pair of laser beams. These manipulators transmit the laser light from optical unit to the laser probe through fiber cables. A pair of manipulators and so laser beams is required for each velocity components. The LDA system used in this study has one pair of fiber manipulators, thus it was possible to measure only one component of velocity at a time. The second component of velocity was obtained by rotating the laser probe and so laser beams 90° . In addition, the system has a Bragg cell which applies 40 MHz frequency shift to wavelength of one of the laser beam to prevent directional ambiguity on measured velocity.

A commercial fog generator supplied seeding particles in to the flow during experiments. Glycerin based smoke liquids were used to generate required seeding fog. Different types of liquids, medium and high density, were used depending on the required data acquisition rates. When higher sampling rates are required, high-density liquid was used for smoke generation since seeding particles from this liquid provides better reflection.

The LDA system used in this study, is equipped with a Dantec F60 signal processor. The optics and the laser of the LDA system are connected to the processor. A workstation computer which has BSA flow software is also connected to the signal processor. The processor analyses the signal that comes from photo detector for corresponding light scatters from seeding particles passing through the measurement volume.

BSA Flow Software is the interface used to acquire and post process the velocity data. The data rate depends on the burst detection and the output is velocity data with unequally spaced timed intervals. The software can calculate mean value, root mean square (RMS) of the velocity components and their equivalent turbulence intensity. Uncertainty on reference velocity is stated as 0.04 %.

Due to the working principle of LDA, the data collection is random and the time intervals between consecutive velocity measurements are not equal. Power Spectral Densities of the velocity data obtained from the LDA measurements were calculated by running Lomb-Scargle Normalized code [50] on MATLAB program. Since the velocity data do not have equal time steps, using MATLAB's built in FFT function was not applicable. For pressure data the same analysis was also applied. In addition, a MATLAB code was written to resample the unequal LDA data and to generate equally spaced data, in order to be able to apply MATLAB built in function to the velocity measurements. Power spectral densities from both methods were also compared.

2.6. Flow control setup

The schematic overview of flow control setup is shown in Figure 2-13. An ED02 pressure regulator was used to control the flow rate of the air blown from leading edge of the wing model. ED stands for Electropneumatic pressure regulator that can be directly controlled. The ED02 pressure regulator is a pneumatic device with integrated electronics that is designed to regulate pneumatic pressure. The pressure regulator mainly consists of a solenoid valve, inlet and outlet connection, and exhaust air connection with silencer. The ED02 pressure regulator can be continuously adjusted once the electrical and pneumatic supplies are connected on it. To do this, the ED02 pressure regulator is controlled via a controller or potentiometer using a set point. The electronics compare the set point with the outlet pressure, which is measured by a pressure sensor, and generate a control variable that is used to control both of the 2/2-way valves with U/I convertors and proportional magnets. This sets the stipulated pressure. Depending on the model, the set point can be controlled by the current, voltage, or a potentiometer. The characteristic curves depict the linear interrelation between voltage and outlet pressure. The curve is presented in Figure 2-14. The device must be fed by supply voltage of 24 V DC ($\pm 20\%$). Maximum 8 bar supply pressure also is needed. The outlet pressure changes from 0 to 6 bar by changing the set point voltage.

In this study, an analogue output module NI 9263 made by National Instruments Corp. was used. The analogue output varies from -10 V to +10 V. It has a 10-terminal, detachable screw-terminal connector that provides connections for 4 analog output channels. Each channel of the NI 9263 has an AO terminal and a common terminal, COM, and there is an additional COM terminal at the bottom of the connector. All of the COM terminals are internally connected to the isolated ground reference of the module. Each channel also has a digital-to-analogue converter (DAC) that produces a voltage signal. When the module powers on, the channels output the startup voltage. Figure 2-15 shows the used pressure regulator (a) and its controlling analog module (b).

A code and a user interface were built in Labview program to be able to adjust the output voltage of the NI 9263 to control the flow rate of the leading edge blowing. Three different dimensionless blowing coefficients, $C_\mu = 0.0001, 0.001$ and 0.01 were applied in the experiments. The momentum coefficient was calculated as follows:

$$C_\mu = \frac{(V_j^2 \times A_j)}{U^2 \times A_s} \quad (2-5)$$

in which V_j is the mean velocity of blowing at leading edge, A_j is the total area of blowing holes, A_s is the surface area of the planform, and U is the free stream velocity.

Figure 2-16 shows the drawing of the wing to clarify the blowing holes and the access of the holes from the trailing edge of the wing. The air is blown from 6 holes with 2 mm diameter which are located near leading edge of the wing model. The distance between the center of injection holes and the leading edge of the wing is 1 mm. The holes are at three sections, $x/C = 0.16, 0.44$ and 0.66 corresponding to the distances of 17 mm, 46 mm and 70 mm from the wing apex. Figure 2-16 also demonstrates the blowing direction, which is normal to the leading edge line and parallel to the bevel surface of the wing.

2.7. Analysis of experimental uncertainty

Experimental data are often considered as a supplementary component that improves engineering analysis. The experimental data should be validated before using the test results for analysis and design. Uncertainty analysis is the procedure used to check this validity and accuracy.

When we report measured value of some parameter, X , it is written as

$$X = X_{best} \pm \Delta X \quad (2-6)$$

where X_{best} represents the best estimate of the measured parameter, and ΔX is the absolute uncertainty associated with experiments. The ratio of the absolute uncertainty to the best estimate ($\Delta X / X_{best}$) is referred to as the fractional or relative uncertainty.

Error always exists while performing experimental measurements. Experimental error may comprise two types: Fixed (or systematic) error and Random error (nonrepeatability). Fixed error can be removed by proper calibration and correction, however, random error cannot be removed. The purpose of uncertainty analysis is to estimate potential random error in the results of the experiments.

Uncertainty estimation of random errors has three steps [51], including the estimation of the uncertainty interval for each quantity, defining the confidence limit and analyzing the propagation of uncertainty in calculations. Since engineering works are mostly single sample experiment, uncertainty interval due to random error is usually plus or minus half the measuring resolution (the least count) of the device [52]. The confidence limit is based on the standard deviation for a normal distribution. Applying error propagation for the Equation (2-2) give the following Equation:

$$x_{c_p} = \pm \left[\left(\frac{\Delta p}{c_p} \frac{\partial c_p}{\partial p} x_{\Delta p} \right)^2 + \left(\frac{p_{dyn.}}{c_p} \frac{\partial c_p}{\partial p_{dyn.}} x_{p_{dyn.}} \right)^2 \right] \quad (2-7)$$

where $x_{\Delta p}$, $x_{p_{dyn.}}$ and x_{c_p} are the relative uncertainties of corresponding variables caused by uncertainties of independently measured quantities. It should be noted that

The calculated relative uncertainty is presented in Table 2-1 for different Reynolds numbers.

Table 2-1 Relative uncertainty at different Reynolds numbers

Reynolds number	$x_{\Delta p}$	$x_{p_{dyn.}}$	x_{C_p}
10000	0.084	0.141	0.164
14000	0.052	0.084	0.098
20000	0.024	0.060	0.064
35000	0.0064	0.015	0.0162
50000	0.003	0.007	0.0076
75000	0.00128	0.0032	0.0034
100000	0.0007	0.0014	0.00156

There are also other noise generating causes from the electrical components in the experimental system that leads to high uncertainty at $Re = 10^4$. For this reason, the pressure results for this Reynolds number are not presented here.

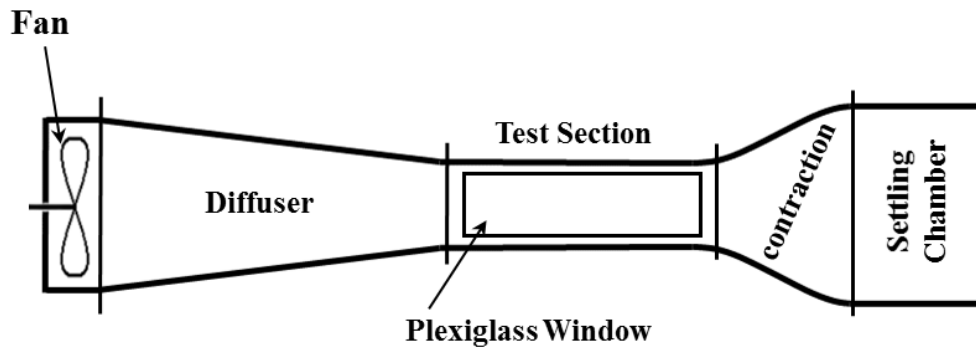


Figure 2-1 Schematic view of wind tunnel

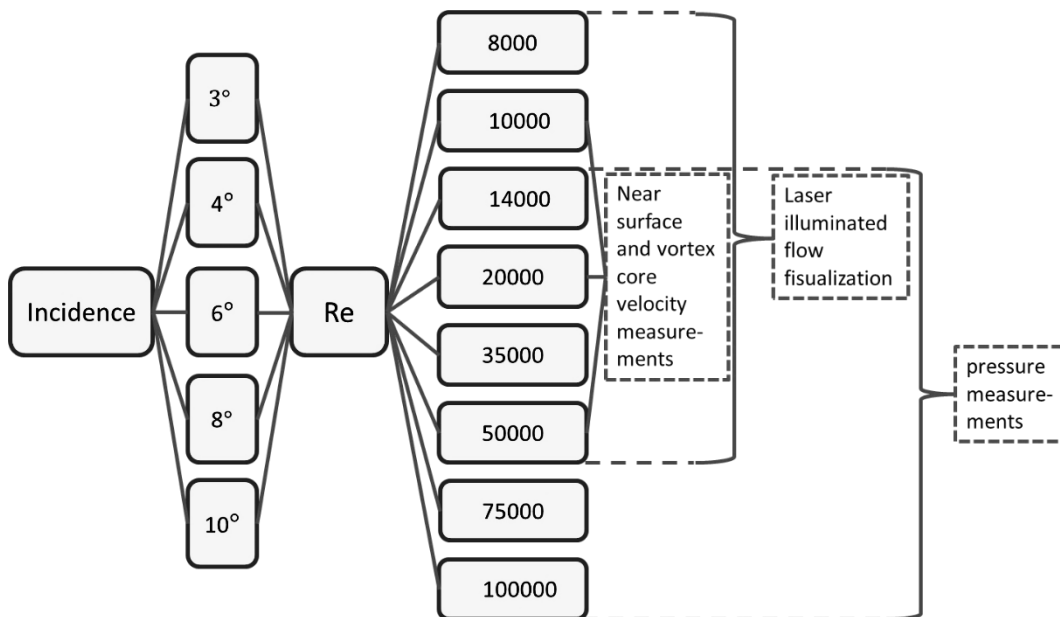


Figure 2-2 Experimental matrix

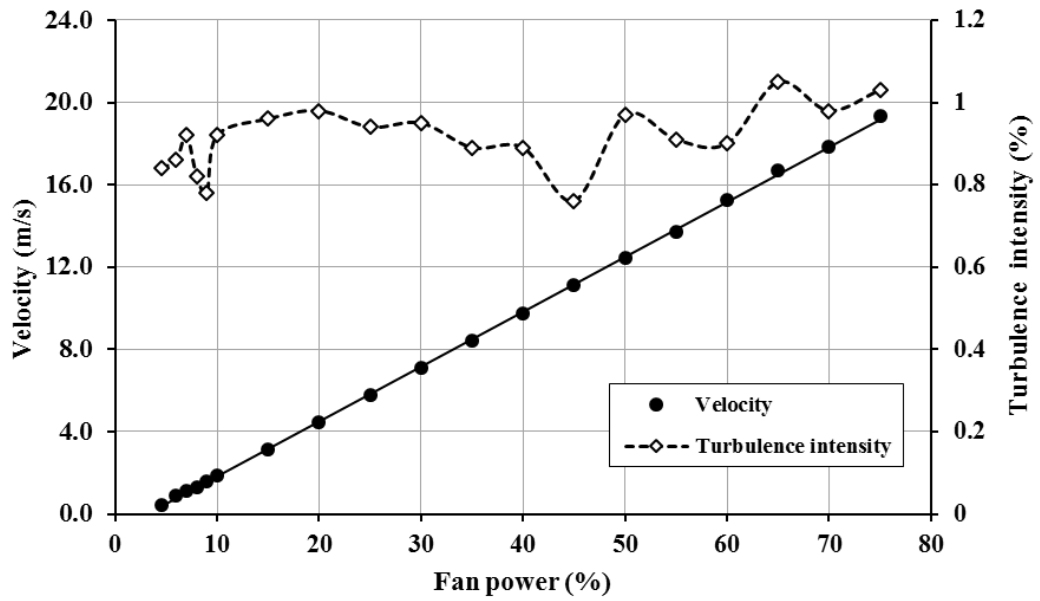


Figure 2-3 Average velocity and turbulence intensity of the flow field in test section with fan power

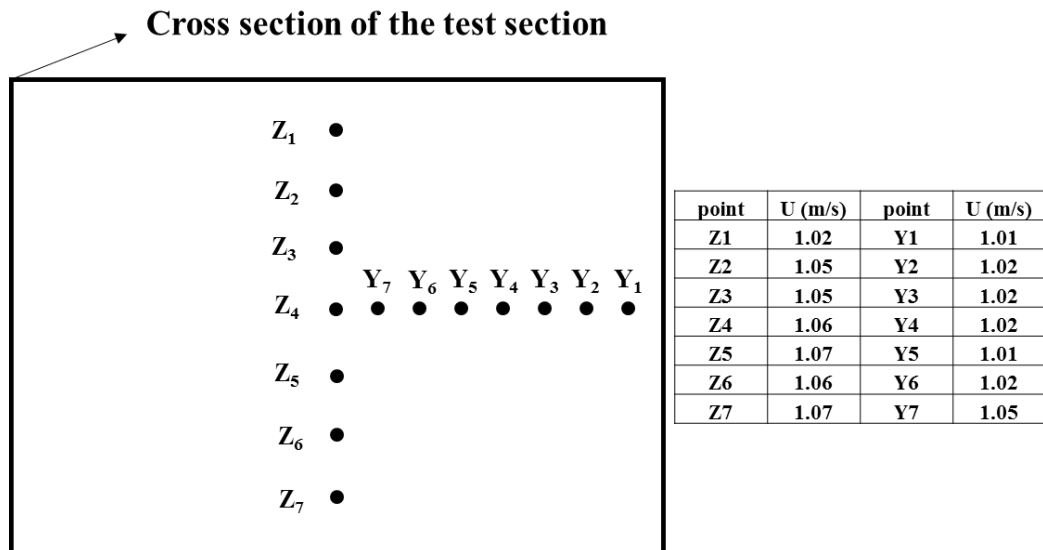


Figure 2-4 Uniformity of flow at low velocities along vertical and horizontal coordinates

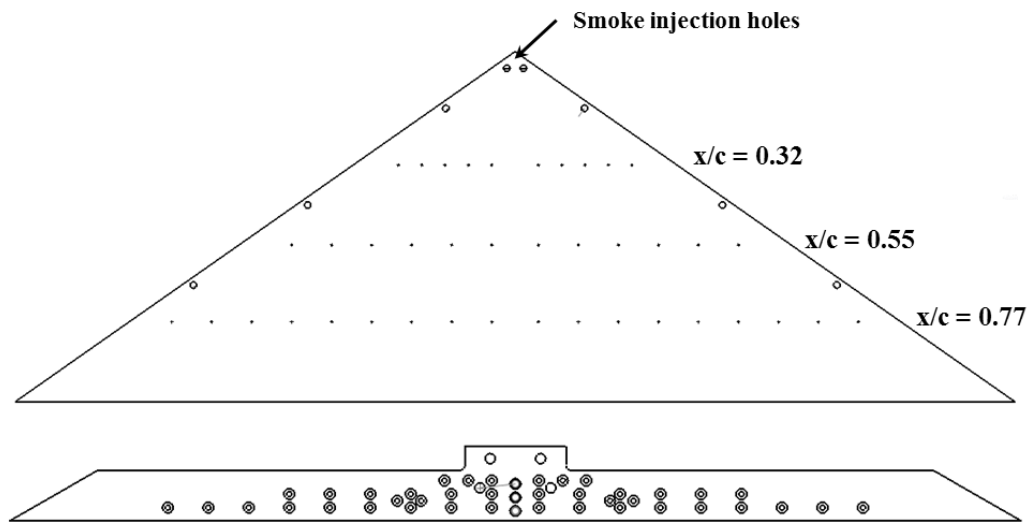


Figure 2-5 Plan view and back view of the wing model showing pressure taps at three chordwise stations

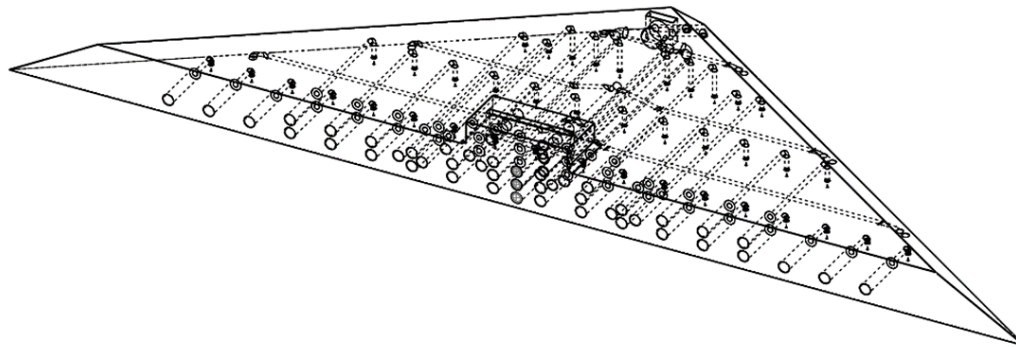


Figure 2-6 CAD drawing of the fabricated wing model



Figure 2-7 Photograph of the fabricated wing model

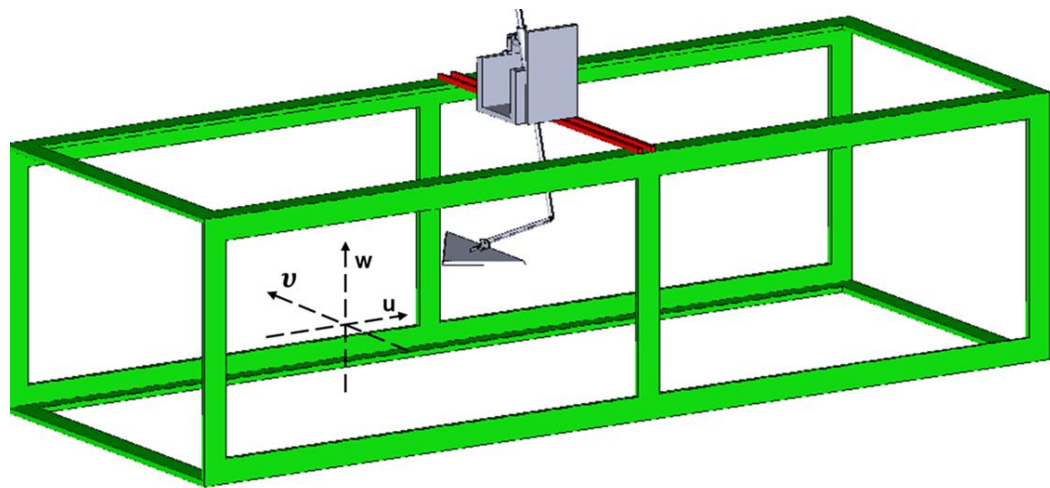


Figure 2-8 Schematic view of the wing, mount and test section assembly with direction of velocity components

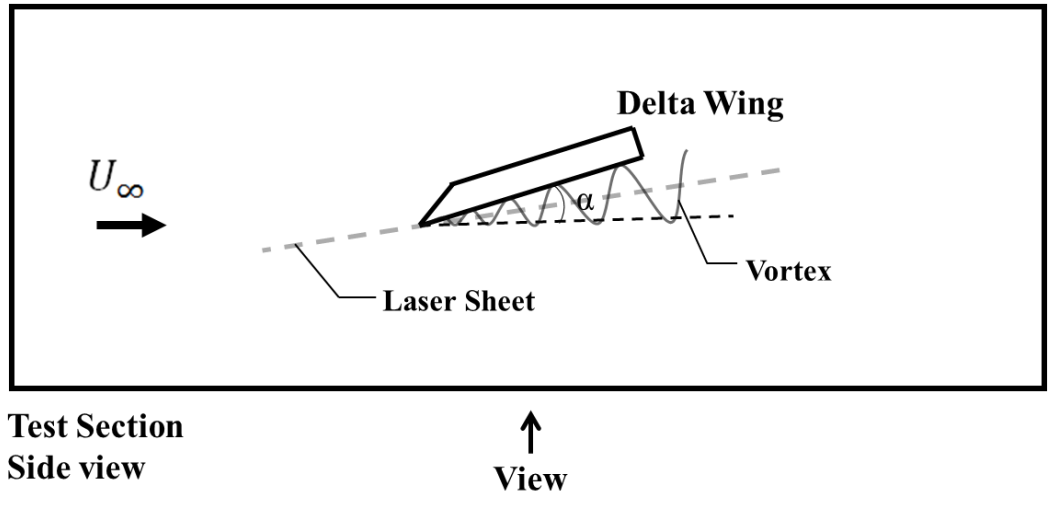
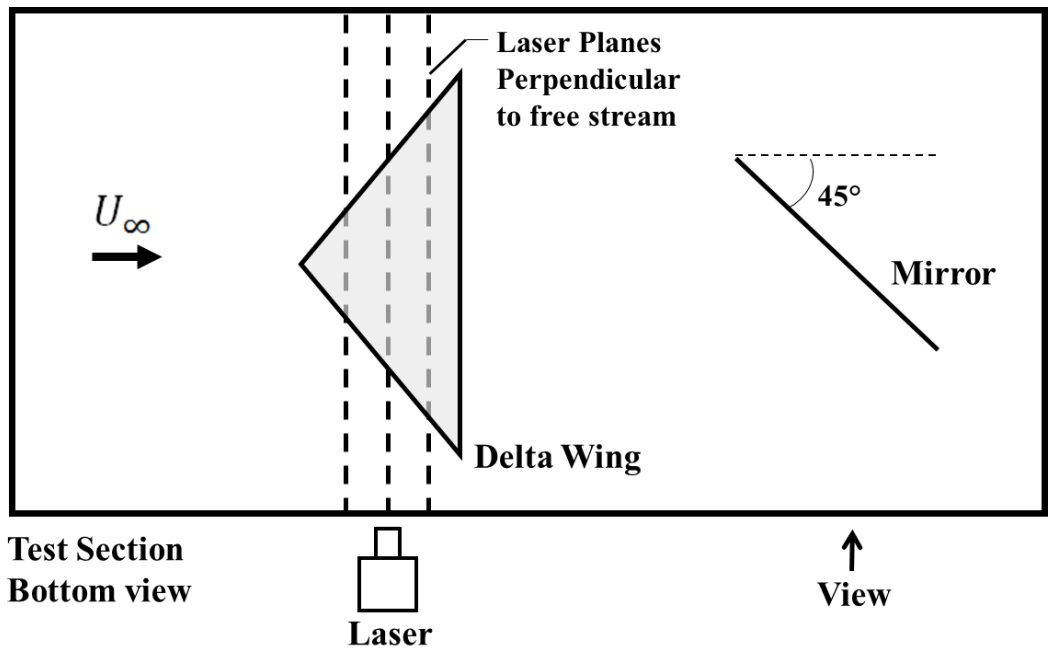


Figure 2-9 Experimental set-up of flow visualizations at cross flow planes (up) and a plane parallel to the leading edge vortex core (bottom)

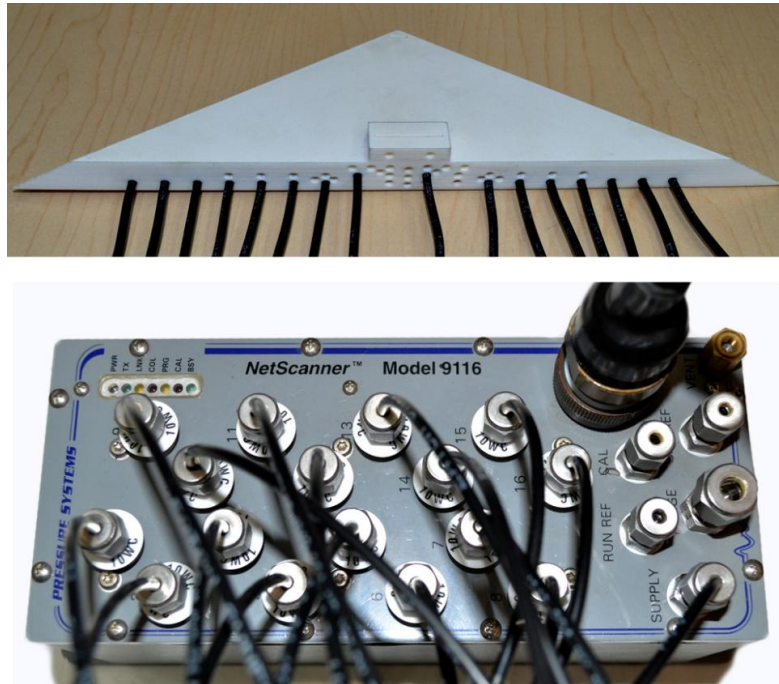


Figure 2-10 The 16-channel pressure scanner and the cables connections

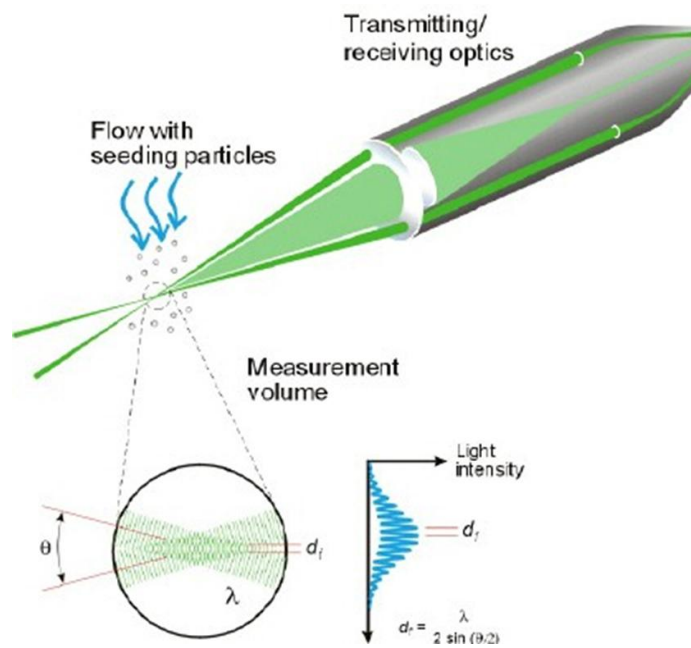


Figure 2-11 Basic working principle of LDA system [49]

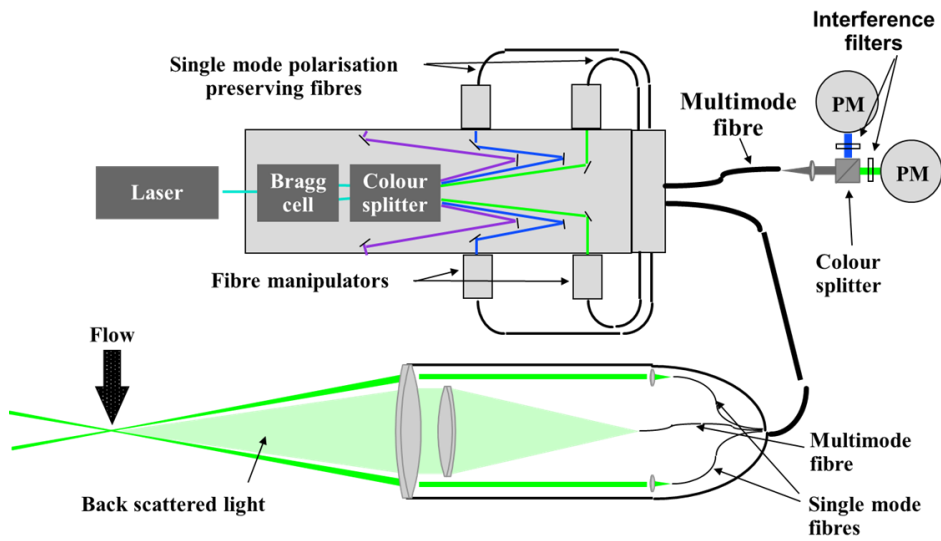


Figure 2-12 Optical components of a LDA system [49]

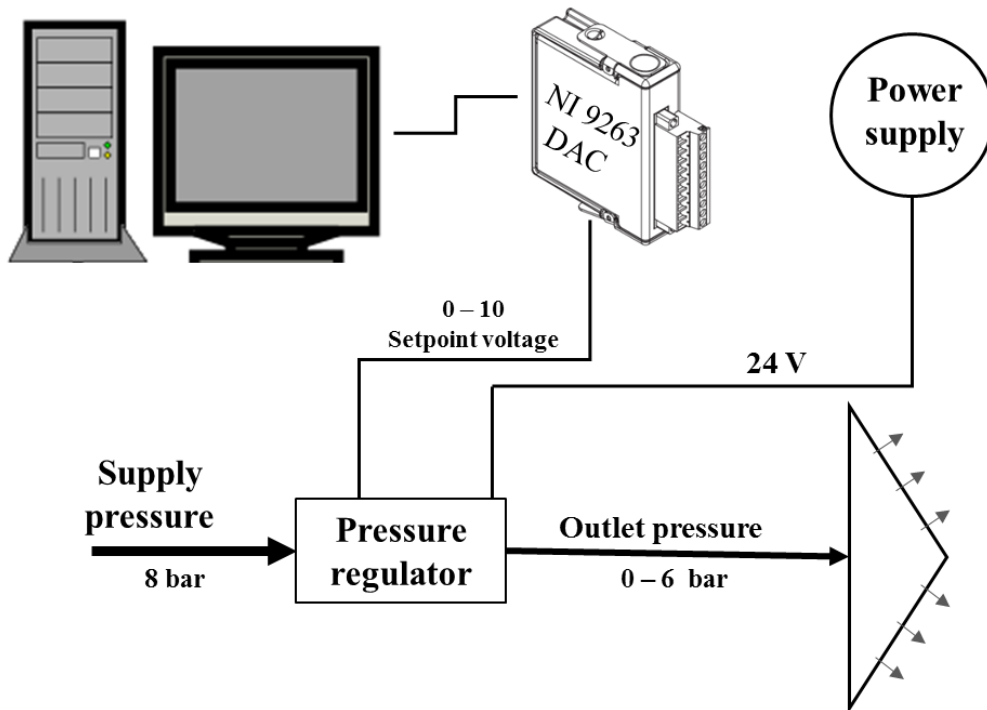


Figure 2-13 Schematic view of flow control system

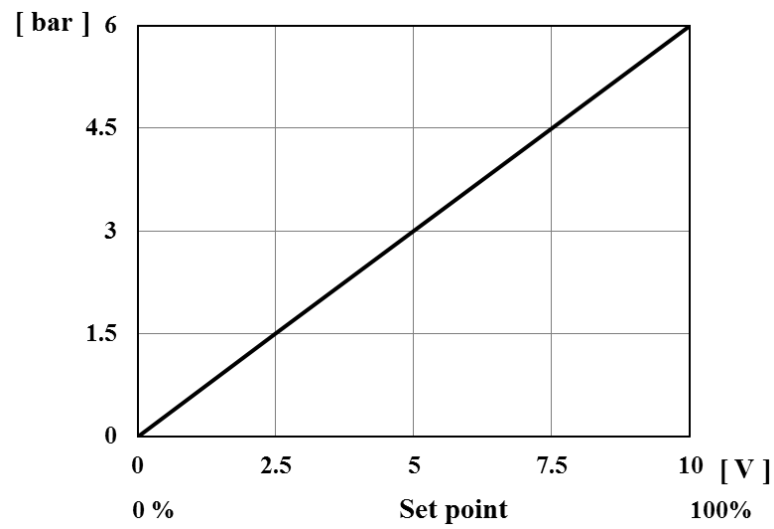


Figure 2-14 Linear interrelation between voltage and outlet pressure of the pressure regulator

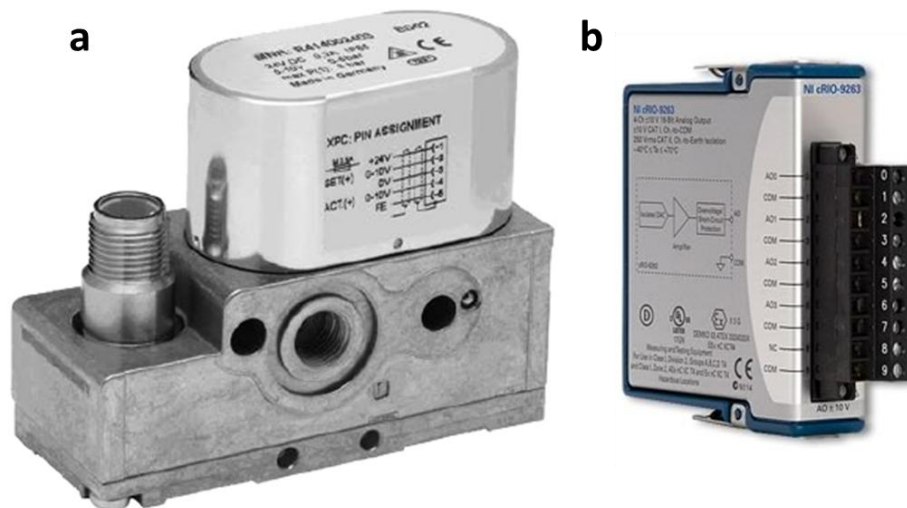


Figure 2-15 Pressure regulator (a) and its controlling analog module (b)

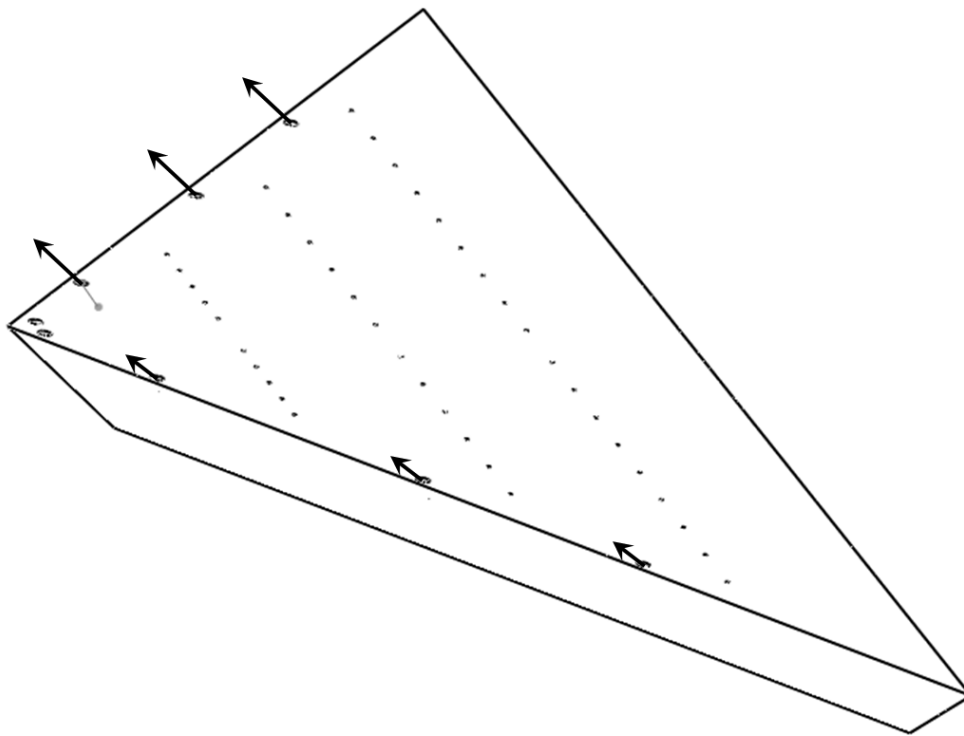
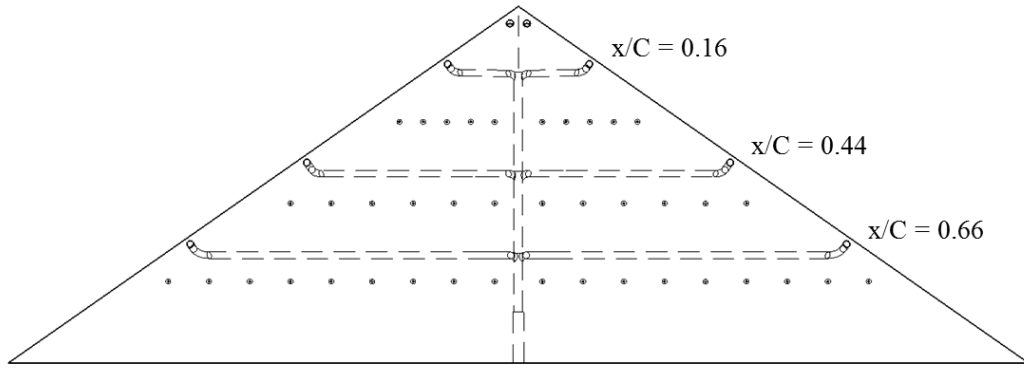


Figure 2-16 The inside wing path of injected air at $x/C = 0.16, 0.44$ and 0.66 (up) and blowing direction (bottom)

CHAPTER 3

RESULTS AND DISCUSSION

The results of the experiments are presented and discussed in this chapter. This section is mainly composed of two subsections corresponding to the results of flow structure on low swept wing in absence and presence of flow control technique, respectively.

3.1. Results in absence of flow control

3.1.1. Surface flow visualizations

The results of flow visualizations on a plane at vortex axis are presented in Figure 3-1, Figure 3-2, Figure 3-3, Figure 3-4, and Figure 3-5, at different Reynolds numbers for attack angles $\alpha = 3^\circ, 4^\circ, 6^\circ, 8^\circ$ and 10° , respectively. For each figure layout, Reynolds number varies from 10000 to 50000 from top to bottom.

The effect of Reynolds number at $\alpha = 3^\circ$ on the flow structure on a plane parallel to leading edge vortices is illustrated in Figure 3-1. At $Re = 10^4$, shown in the top image of the figure, a pair of leading edge vortices with clear indication of vortex breakdown location is apparent. Downstream of the vortex breakdown location, the flow spreads over the wing and covers the wide area of it. By increasing the Reynolds number to 1.4×10^4 , the location of the vortex breakdown moves

upstream. With further increase in Reynolds number the vortex breakdown location reaches to proximity of the wing apex. At $Re = 3.5 \times 10^4$ the breakdown occurs almost at the apex of the wing, and no noticeable change is witnessed with further increase in Reynolds number.

Figure 3-2 represents the flow visualization results for 4° angle of attack. At $Re = 10^4$, upstream of vortex breakdown, there is an indication of dispersion of smoke which can be explained as deterioration of the leading edge vortices. In addition, the type of vortex breakdown is quite different compared to the case at angle of attack 3° shown in Figure 3-1. At $Re = 1.4 \times 10^4$, the flow structure shows substantial changes. There is no clear indication of traditional form of leading edge vortex and its breakdown, instead, aforementioned deterioration in leading edge vortices spatially expands and covers the region close to the apex of the wing. As seen at $Re = 2 \times 10^4$ and 3.5×10^4 , this pattern moves toward apex as the Reynolds number increases. Once this pattern reaches to the apex, no significant change in flow structure is witnessed with further increase in Reynolds number.

Reynolds number effect on flow structure at 6° angle of attack is shown in Figure 3-3. At $Re = 10^4$, a well-defined swirl pattern is evident and there is no indication of leading edge vortex and its breakdown, which is primarily due to the three-dimensional separation from the wing surface. The swirling structure becomes smaller by increasing the Reynolds number and moves upstream. At $Re = 3.5 \times 10^4$, the pattern reaches to the proximity of the apex and covers a small area of the wing tip. No changes are witnessed with further increase in Reynolds number.

Similar flow structure and its trend response to the change in Reynolds number can also be seen at attack angles of 8° and 10° , which are shown in Figures 3-4 and 3-5, respectively. As shown in Figure 3-4 for the case of 8° attack angle, the swirl pattern has relatively larger in spatial extent compared to the flow structure of 6° attack angle shown in Figure 3-3. The swirl pattern reduces in size and moves toward apex as the Reynolds number increases. For the 10° attack angle shown in Figure 3-5, at $Re = 10^4$, nearly the whole wing surface is covered by the swirling flow structure caused by three-dimensional separated flow. For this

attack angle, the trend in transition of flow structure as the Reynolds number increases is almost identical with the attack angles of 6 and 8° shown in Figures 3-3 and 3-4, respectively. Considering all three attack angles where the three dimensional surface separation is evident, it can be stated that, as the attack angle increases, the scale of the separated region gets larger and becomes less sensitive to increase in Reynolds number.

Overall, considering the surface flow smoke visualization results as a whole, it can be stated that increase in attack angle from 3° to 4° yields a significant change in leading edge vortex structure and its breakdown. For both angles, increase in Reynolds number causes movement of breakdown location toward the apex of the wing. Further increase in attack angles, causes three-dimensional surface separation in large-scale swirl form covering the whole planform. This structure moves toward apex and gets smaller as the Reynolds number increases. It is important to note that, as the attack angle increases, it gets harder for flow structure to be affected by Reynolds number.

3.1.2. Cross flow visualizations and pressure measurements

Figures 3-6, 3-7, 3-8, 3-9 and 3-10 show the cross flow visualizations at different Reynolds numbers for attack angles of $\alpha = 3^\circ, 4^\circ, 6^\circ, 8^\circ$ and 10° , respectively. Steady and unsteady pressure measurements are also embedded on the corresponding figures to obtain comprehensive understanding of the flow structure and to give one-to-one comparison of pressure measurements with smoke visualization results. Since smoke diffusion problems are encountered at high Reynolds numbers, cross flow visualization results are given for the Reynolds numbers varying from 10^4 to 5×10^4 . Pressure measurements are not presented for $Re = 10^4$ due to uncertainty issues as explained in Chapter 2. In addition, Reynolds numbers 1×10^5 is added for the results of pressure measurements. For each figure, the layouts are constructed in the same format. The first and second columns represent the results for chordwise distance of $x/C =$

0.32 and $x/C = 0.77$, respectively. Each row corresponds to a different Reynolds number, which are listed in increasing order from top to bottom. The pressure measurements are embedded to figures as $-C_p$ and C_{pRMS} values where the calculations of these parameters are described in Chapter 2. The left axis of the chart in the first column represents $-C_p$ values and the right axis of the chart in the second column represents C_{pRMS} values where the solid and dash lines are used for the values of corresponding parameters, respectively. Horizontal axis represents y/s , nondimensional spanwise distance from the wing center.

The results for 3° angle of attack are shown in Figure 3-6. Overall comparisons of smoke visualizations with pressure measurements indicate that smoke visualization results are inline with pressure measurements. The highest $-C_p$ values represent highest suction areas whereas lowest $-C_p$ values present the places at which flow reattaches to the wing surface. The point corresponding to the vortex core in smoke visualization has highest values of $-C_p$. At $Re = 10^4$ and $x/C = 0.32$, a well-defined leading edge vortex pattern can be seen. At $x/C = 0.77$, absence of vortical structure is evident which indicates that vortex breakdown has already taken place upstream of this chordwise distance. At $Re = 1.4 \times 10^4$, although the spanwise location of the vortex core is remained unchanged, the vortex seems weaker due to more dispersion of the smoke. Flow reattachment is obvious at $x/C = 0.77$ at spanwise distance of 0.3. Considering the pressure fluctuations, at $x/C = 0.32$, the maximum value of C_{pRMS} is at same spanwise location as the vortex core.. At $Re = 2 \times 10^4$, highest value of $-C_p$ is increased to 0.9 at $x/C = 0.32$, also, highest surface pressure fluctuations occur at $y/s = 0.3$ which is between vortex core and reattachment location. The pressure distribution at $x/C = 0.77$ remains unchanged and amount of pressure fluctuations have been increased. Increasing Reynolds number to 3.5×10^4 leads to a more distributed vortex to flow field at $x/C = 0.32$. Pressure distribution pattern is similar to the lower Reynolds number. At $x/C = 0.77$, the flow field has been moved toward wing leading edge. Further increasing Reynolds number to $Re = 5 \times 10^4$ causes a slight rise in the highest value of $-C_p$ at $x/C = 0.32$. At chordwise distance of $x/C = 0.77$, the flow structure and pressure distribution shape is identical to the

previous Reynolds number. At $Re = 10^5$, pressure distribution and pressure fluctuation are very similar to the $Re = 5 \times 10^4$ except the highest value of $-C_p$ at $x/C = 0.32$ that has reached 1.5 which is the maximum value in 3° angle of attack. Moreover, at this angle of attack and for the Reynolds numbers that leading edge vortices exist and breakdown occurs, maximum values of C_{pRMS} 's happens between reattachment point and vortex core. In addition, at $x/C = 0.32$, as Reynolds number increases, vortex moves toward leading edge.

Figure 3-7 provides effect Reynolds number on the cross flow structure and pressure distribution at 4° angle of attack. Since the flow structure contains leading edge vortex and breakdown, aforementioned discussions for the results of 3° angle of attack shown in Figure 3-6 are also valid. An apparent leading edge vortex structure can be seen at $Re = 10^4$ and $x/C = 0.32$. Non-vortical structure of the flow at $x/C = 0.77$ is a clear indication of the occurrence of vortex breakdown upstream of this chordwise distance. Increasing the Reynolds number to 1.4×10^4 results in weaker vortex core which disperses and covers wider flow region at $x/C = 0.32$. The flow at $x/C = 0.77$ has an expected structure downstream of a vortex breakdown. At $Re = 2 \times 10^4$ and $x/C = 0.32$, the location of the highest value of pressure fluctuation is between the minimum and maximum pressure values. At $x/C = 0.77$, obvious change in pressure distribution and flow structure is not recognized. Further increase of Reynolds number to 3.5×10^4 leads to a slight increase in highest value of $-C_p$ at $x/C = 0.32$. Also, the flow reattachment causes zero value of $-C_p$ at $y/s = 0.3$. On the other hand, the flow structure is still unchanged at $x/C = 0.77$. Beyond $Re = 3.5 \times 10^4$, increasing of Reynolds number does not affect the flow behavior considerably.

Effect of Reynolds number on flow structure at 6° angle of attack is illustrated in Figure 3-8. At $Re = 10^4$ and $x/C = 0.32$, the reattachment location of the flow is almost the same as the wing centerline. At $x/C = 0.77$, the flow field has covered the whole wing. A slight increase in Reynolds number moves the reattachment location outboard at $x/C = 0.32$. Due to lack of leading edge vortices, variations in C_p distributions are less. At $x/C = 0.77$, the flow field has moved outboard. At Re

$= 2 \times 10^4$, the pressure distribution is still flat but the value of $-C_p$'s have been increased to 0.9 at $x/C = 0.32$. Also, a considerable increase in pressure fluctuations is apparent. Further increasing Reynolds number and reaching $Re = 3.5 \times 10^4$ gives rise to a significantly different pressure distribution over wing surface at $x/C = 0.32$. This kind of pressure distribution which is similar to a vortical type pressure distribution may be because of the fact that high speed separated flow from the leading edge of the wing tries to generate vortices in interaction with three-dimensional separated flow from the wing surface. The reattachment point at both chordwise distances has been moved outboard. Highest value of pressure distribution is located between maximum and minimum value of $-C_p$. At $Re = 5 \times 10^4$, reattachment point move further from the wing centerline. It can be said that for Reynolds numbers beyond 3.5×10^4 , pressure and its fluctuation distribution over the wing surface are entirely identical.

Figure 3-9 shows the flow behavior over the wing with angle attack of 8° at different Reynolds numbers. The trend of change in flow structure is similar to 6° incidence. However, the reattachment location of the flow remains same and is around the wing centerline. Increasing Reynolds number from 1.4×10^4 to 2×10^4 leads to a rise in $-C_p$ value from 0.6 to 0.9. In addition, it causes a considerable rise in the amount of pressure fluctuations at $x/C = 0.32$. At $Re = 3.5 \times 10^4$, a transmission from even to vortical pattern is evident in pressure distribution at $x/C = 0.32$. It could be said that pressure distribution and flow structure does not change at the Reynolds numbers exceeding 5×10^4 .

Figure 3-10 shows the Reynolds number effect on flow structure at $\alpha = 10^\circ$. The flat pattern of pressure distribution does not change even at high Reynolds numbers. The rotating structure remain unchanged in interaction with separated flow from wing leading edge even at high Reynolds numbers. Change in Reynolds number from 1.4×10^4 to 2×10^4 leads to an increase from 0.6 to 0.9 in $-C_p$ values at $x/C = 0.32$. No evident change in pressure distribution is observed at $x/C = 0.77$.

3.1.3. Spectral Analysis of velocity measurements

Power spectral densities of the velocities measured at the core of leading edge vortices at 3° of attack angle are presented in Figure 3-11 and Figure 3-12 for Reynolds numbers of $Re = 10^4$ and $Re = 2 \times 10^4$, respectively. The intersection points of the dashed lines represent the measurement locations at three chordwise distances of $x/C = 0.32, 0.55$ and 0.77 . For each figure, the left columns are assigned to streamwise (u) components whereas the right columns are for transverse (w) components of velocities measured by LDA technique. The figures demonstrate the velocity spectrum density over dimensionless frequency, Strouhal number $St = fc/U_\infty$.

Figure 3-11 shows u and w components of spectrum density of LDA velocity measurements for $Re = 10^4$ at attack angle of 3° . Two strong frequency peaks can be seen upstream of vortex breakdown, at $x/C = 0.32$, at both u and w components which are between $St = 0$ and $St = 1$. For the corresponding peaks, comparing the spectrums of u and w component velocities, although the amplitudes show variations, identical frequencies are detected. Moving downstream results in broad spectrum distributions. Weaker peaks at various St values can be seen at $x/C = 0.55$. We can attribute this broad spectrum to the fact that fluctuations happen at various frequencies and amplitude without any distinctive peaks downstream of vortex breakdown. At $x/C = 0.77$ which corresponds to a region further downstream of vortex breakdown location, an even spectrum unaccompanied by any considerable peak can be seen. The amplitude of peaks in both u and w components significantly decreases by moving from apex toward trailing edge of the wing.

Velocity spectrums for $Re = 2 \times 10^4$ at attack angle of 3° is presented in Figure 3-12. Dominant peaks cannot be identified, and spectrum patterns in u component of velocity at $x/C = 0.55$ and 0.77 are nearly similar to the spectrum pattern upstream at $x/C = 0.32$. Unlike u component, spectrum densities in w component at downstream chordwise distances differ from densities at $x/C = 0.32$. Wide spectrum with very low amplitudes is observed.

Figures 3-13, 3-14, 3-15 and 3-16 show the spectrum of velocity results measured on wing surface at Reynolds numbers of $Re = 10^4$ and $Re = 3.5 \times 10^4$ for attack angles of $\alpha = 3^\circ$ and $\alpha = 6^\circ$. The LDA velocity measurements were performed at a normal distance of 5 mm from the wing surface in streamwise and vertical components. Surface flow visualizations along with spectral density charts are demonstrated. The figures are constructed with the following approach. At the center of figure layouts, the surface flow visualization results for two different Reynolds number case are superposed where one half of the wing represents $Re = 10^4$ and the other half represents $Re = 3.5 \times 10^4$ case.

Figure 3-13 illustrates the u component of velocity spectrums at angle of attack 3° . The measurement points which are located at spanwise distance of $y/s = 0.5$ of three chordwise distances. Corresponding spectrums of $Re = 10^4$ case are demonstrated on the left hand side of the figure whereas the right hand side of the figure corresponds to $Re = 3.5 \times 10^4$ case. At $Re = 10^4$ and $x/C = 0.32$, a dominant frequency peak at $St = 2$ can be seen. At $x/C = 0.55$, not distinct but low amplitude weak peaks are widely distributed over the broad range of St number varying from 0 to 3. At $x/C = 0.77$, broad spectrum with comparatively lower peak amplitudes can be seen. At $Re = 3.5 \times 10^4$ (right hand side), all spectrum corresponding to the three chordwise distances have broad spectrum with density amplitudes clearly less than the spectrum densities at $Re = 10^4$.

Figure 3-14 shows the w component of velocity spectrums at 3° angle of attack. At $Re = 10^4$ and $x/C = 0.32$, distinctive peaks which are spread around $St = 0.5$ and $St = 2$ can be noticed. At $x/C = 0.55$, a dominant peak occurs at $St = 2$. Some lower amplitude peaks can also be seen at $St = 1$ and $St = 3$. Likewise velocity spectrums in u component at $Re = 3.5 \times 10^4$, the spectrum in w direction lack any significant peaks at the all of the three chordwise distances. Furthermore, amplitudes of the fluctuation are lower compared to the corresponding Reynolds number in w direction.

Near surface velocity spectrums for 6° angle of attack at $Re = 10^4$ and $Re = 3.5 \times 10^4$ are presented in Figures 3-15 and 3-16, respectively. Figure 3-15 shows the

spectrum charts for velocity at u component. The white points dividing span of the wing into three equal parts are measurement locations at three chordwise distances. At the points corresponding to $Re = 10^4$, all of the spectrums are broad. At the point adjacent to the center of three-dimensional separated pattern, relatively noticeable peaks are around $St = 0.5$. It can be said that by moving further downstream of the swirl pattern, the spectrum densities decrease and the spectrums get broader. This trend can also be seen at $Re = 3.5 \times 10^4$. In comparison to u component velocities, the spectrum densities are lower for w component.

Figure 3-16 illustrates velocity spectrums of 6° angle of attack at w component at $Re = 10^4$ and $Re = 3.5 \times 10^4$. At $Re = 10^4$, most dominant peak are recognized at the point near the swirling structure of the three-dimensional separated flow. The same trend of decreasing in the magnitude of fluctuations is also apparent here by moving downstream. The spectrum densities are significantly low at $x/C = 0.77$. At $Re = 3.5 \times 10^4$, no significant peak is detected at all measurement points. The fluctuations are less powerful compared to the lower Reynolds number case. Furthermore, the spectrums remain broad and do not change with moving toward downstream.

3.2. Results with flow control

In this section the effect of blowing from wing leading edge on flow structure and pressure distribution is presented and is compared with flow in absence of flow control. Three momentum coefficients including $C_\mu = 0.0001$, 0.001 and 0.01 have been applied at different Reynolds numbers. Blowing from the wing leading edge has been selected for 6° and 10° angles of attacks in order to understand effect of the control technique on three-dimensional separated surface flow. Surface and cross flow visualization and pressure measurements were applied.

3.2.1. Surface flow visualization

The effect of steady leading edge blowing with momentum coefficients including $C_\mu = 0.0001$, 0.001 and 0.01 on flow structure were investigated in the present study. Figures 3-17, 3-18, 3-19, 3-20, 3-21 and 3-22 illustrate the effect of C_μ on surface flow visualizations at different Reynolds numbers and angles of attack.

The effect of leading edge blowing at $Re = 10^4$ and attack angle of 6° is shown in Figure 3-17. There is not any obvious difference between the flow structure of no control and control with the momentum coefficient of $C_\mu = 0.0001$. A slight decrease in the size of three-dimensional separated flow can be seen at $C_\mu = 0.001$. Further increase in the amount of blowing momentum causes formation of leading edge vortices over the wing surface. The leading edge vortices are evident at $C_\mu = 0.01$. However, it is important to note that the breakdown of these vortices at a chordwise distance are very close the wing apex.

Figure 3-18 shows the trend of change in flow structure by increasing the momentum coefficient of blowing at $Re = 2 \times 10^4$ and $\alpha = 6^\circ$. Likewise lower Reynolds number, the blowing from the wing leading edge at dimensionless blowing corresponding to $C_\mu = 0.0001$ does not exert an influence on the flow structure. At $C_\mu = 0.001$, the flow visualization appears to suggest that the three-dimensional separated pattern has been started to change to generate leading edge vortices. Further increase in the flow rate to reach to the corresponding momentum coefficient of $C_\mu = 0.01$ gives rise to formation of well-defined leading edge vortices. Compared to $Re = 10^4$ shown in Figure 3-17, transition from three-dimensional separated region to leading edge vortex happens at smaller momentum coefficients. In addition, relatively stronger leading edge vortex is obtained at $Re = 2 \times 10^4$ at $C_\mu = 0.01$ compared to $Re = 10^4$.

For the flow structure at $Re = 3.5 \times 10^4$ and $\alpha = 6^\circ$, which is shown in Figure 3-19, the same trend in transition from three dimensional separation to leading edge vortex pattern, witnessed in lower Reynolds number cases shown in Figures 3-17 and 3-18, is also evident. Compared to lower Reynolds number cases, at $Re = 3.5$

$x 10^4$, the flow structure is more sensitive to the blowing through leading edge which in turn shows drastic changes in flow structure at relatively lower momentum coefficients.

The effect of leading edge blowing at $\alpha = 10^\circ$ is shown in Figure 3-20 for $Re = 10^4$. Three-dimensional separated flow, which covers the entire area of the wing surface, is hardly affected by the blowing. Strong swirling pattern gets smaller and shifts toward the apex of the wing with increasing momentum coefficient. There is no indication of switching to leading edge vortex pattern. Similar trend is also witnessed at $Re = 2 \times 10^4$ and $Re = 3.5 \times 10^4$ cases shown in Figure 3-21 and Figure 3-22, respectively. Although the significant changes in flow structure are seen at $C_\mu = 0.01$ including the decrease in the spatial extent of the swirling pattern and the shift in the location of the core of the swirl, there is no footprint of reoccurrence of leading edge vortex at the tested blowing coefficients.

3.2.2. Pressure measurements

The results of pressure measurements are presented as $-C_p$ versus spanwise distance (y/s) plots in Figures 3-23 and 3-24. The plots are presented in three rows and columns. The rows represent three different Reynolds numbers including $Re = 2 \times 10^4$, $Re = 3.5 \times 10^4$ and $Re = 5 \times 10^4$ from top to bottom, respectively, whereas, the columns are assigned to chordwise distances of $x/C = 0.32$, $x/C = 0.55$ and $x/C = 0.77$, from left to right, respectively. The blue, red, green and black lines represent the distributions for momentum coefficients of $C_\mu = 0.0$, $C_\mu = 0.0001$, $C_\mu = 0.001$ and $C_\mu = 0.01$, respectively.

Figure 3-23 illustrates pressure distribution at different Reynolds numbers and chordwise distances for attack angle of 6° . At $Re = 2 \times 10^4$, the pressure distribution at all chordwise distances are similar for $C_\mu = 0.0$ and 0.0001 which indicate that blowing at this low momentum coefficient does not affect the flow structure over the wing. Starting from $C_\mu = 0.001$, the effect of blowing becomes evident. Remarkable changes in pressure distribution are witnessed at highest

blowing coefficient of $C_\mu = 0.01$. Particularly, at $x/C = 0.32$, an increase in highest value along with a decrease in lowest value of $-C_p$'s can be identified. As getting closer to the trailing edge, the flat pressure distributions are obtained. At $Re = 3.5 \times 10^4$, the distributions are similar to the lower Reynolds number except for the cases $C_\mu = 0.0001$ and 0.001 at $x/C = 0.32$. At $Re = 7.5 \times 10^4$, an increase in highest value of $-C_p$ can be seen at $x/C = 0.32$ for $C_\mu = 0.01$. Also, the highest value of $-C_p$ that is believed to be the indication of the vortex core shifts toward the leading edge. Similarly, highest value of $-C_p$ at $x/C = 0.55$ increases just for the case for $C_\mu = 0.01$. The pressure distribution at $x/C = 0.77$ for all of the Reynolds numbers seems to be not affected significantly by the increase in momentum coefficients.. The pressure distribution at $C_\mu = 0.01$ has the minimum lowest value of $-C_p$ which possibly indicates a stronger reattachment of the flow to the wing surface.

Figure 3-24 shows the pressure distribution of flow field over the wing surface at $\alpha = 10^\circ$ at three different Reynolds numbers. A clear increase in values of $-C_p$ can be seen by the increase of blowing coefficient at $Re = 2 \times 10^2$ and $x/C = 0.32$. At higher Reynolds numbers for the same chordwise distance, pressure distributions are similar. For $C_\mu = 0.01$, pressure distribution variations are more compared to the lower momentum coefficients. Also, the values of $-C_p$'s at $C_\mu = 0.01$ are considerably higher than the values at lower momentum coefficients. At $x/C = 0.55$, pressure distributions are almost the same for different Reynolds numbers. For all of the Reynolds numbers, maximum and minimum $-C_p$ values happen at $C_\mu = 0.01$. At $x/C = 0.77$ and $Re = 2 \times 10^4$, increasing the momentum coefficient decreases the $-C_p$ values near the wing centerline region. At higher Reynolds numbers, pressure distributions are almost identical for $C_\mu = 0, 0.0001$ and 0.001 .

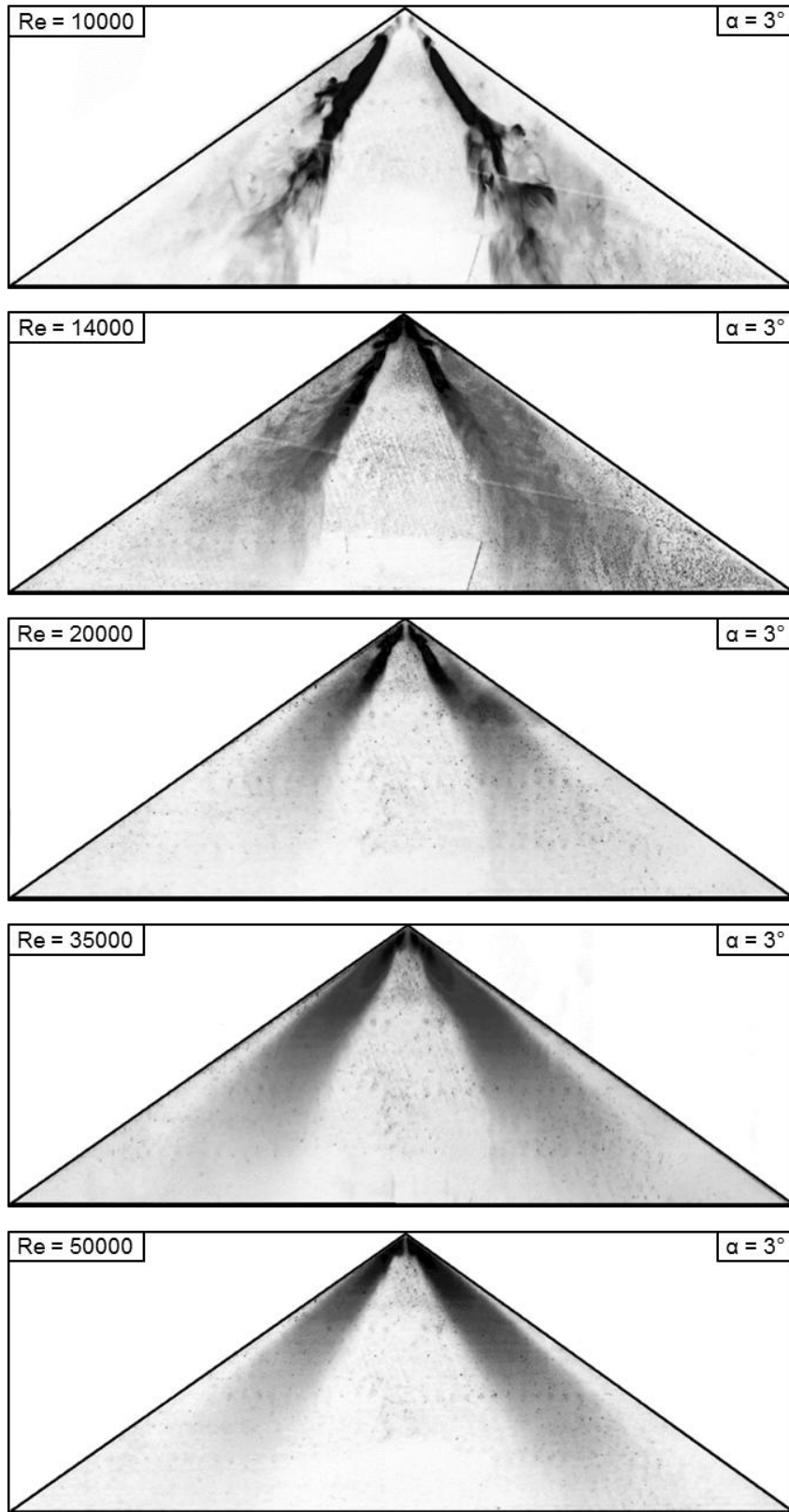


Figure 3-1 Surface flow visualizations at different Reynolds numbers and at $\alpha = 3^\circ$ angle of attack

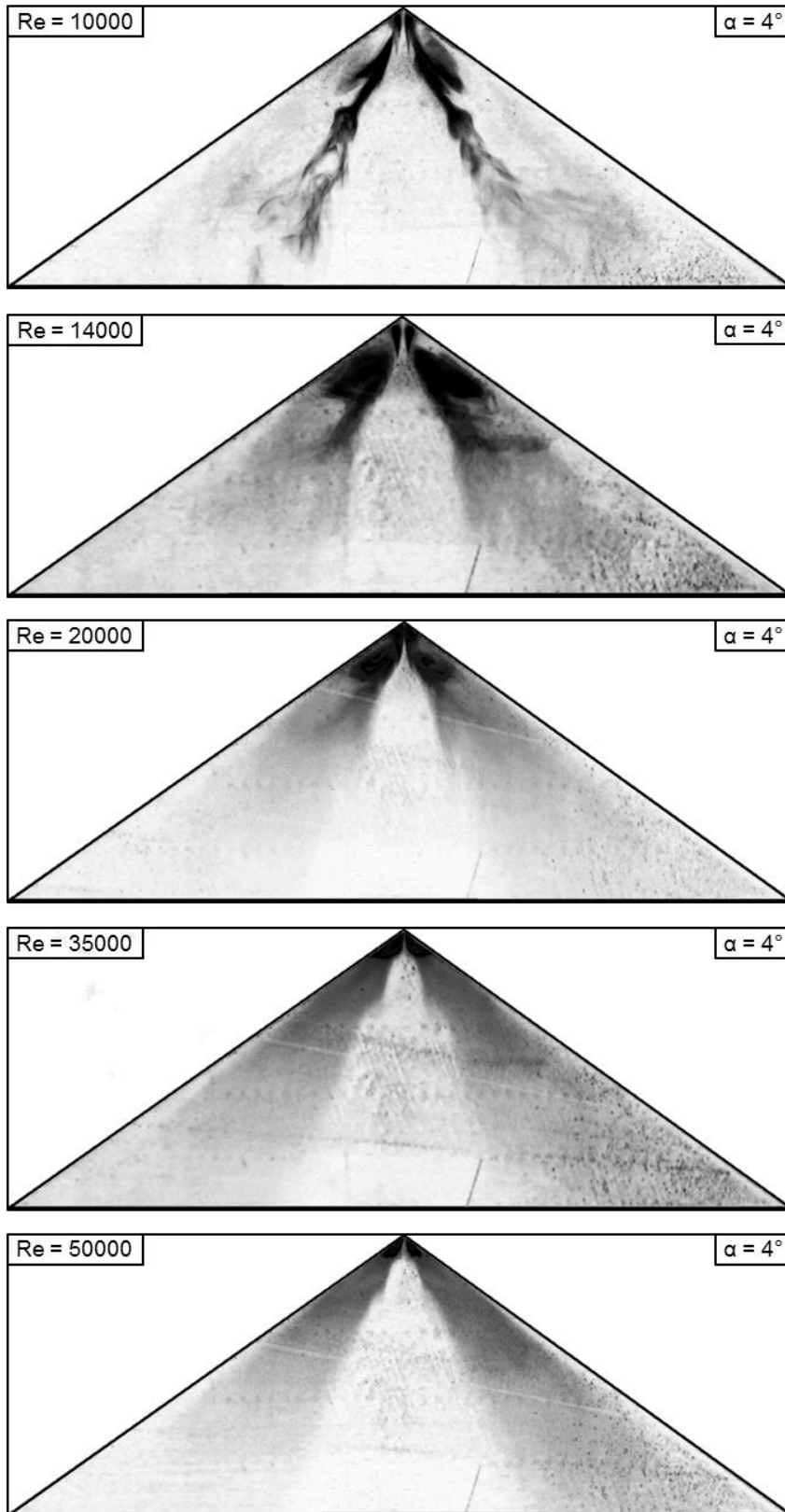


Figure 3-2 Surface flow visualizations at different Reynolds numbers and at $\alpha = 4^\circ$ angle of attack

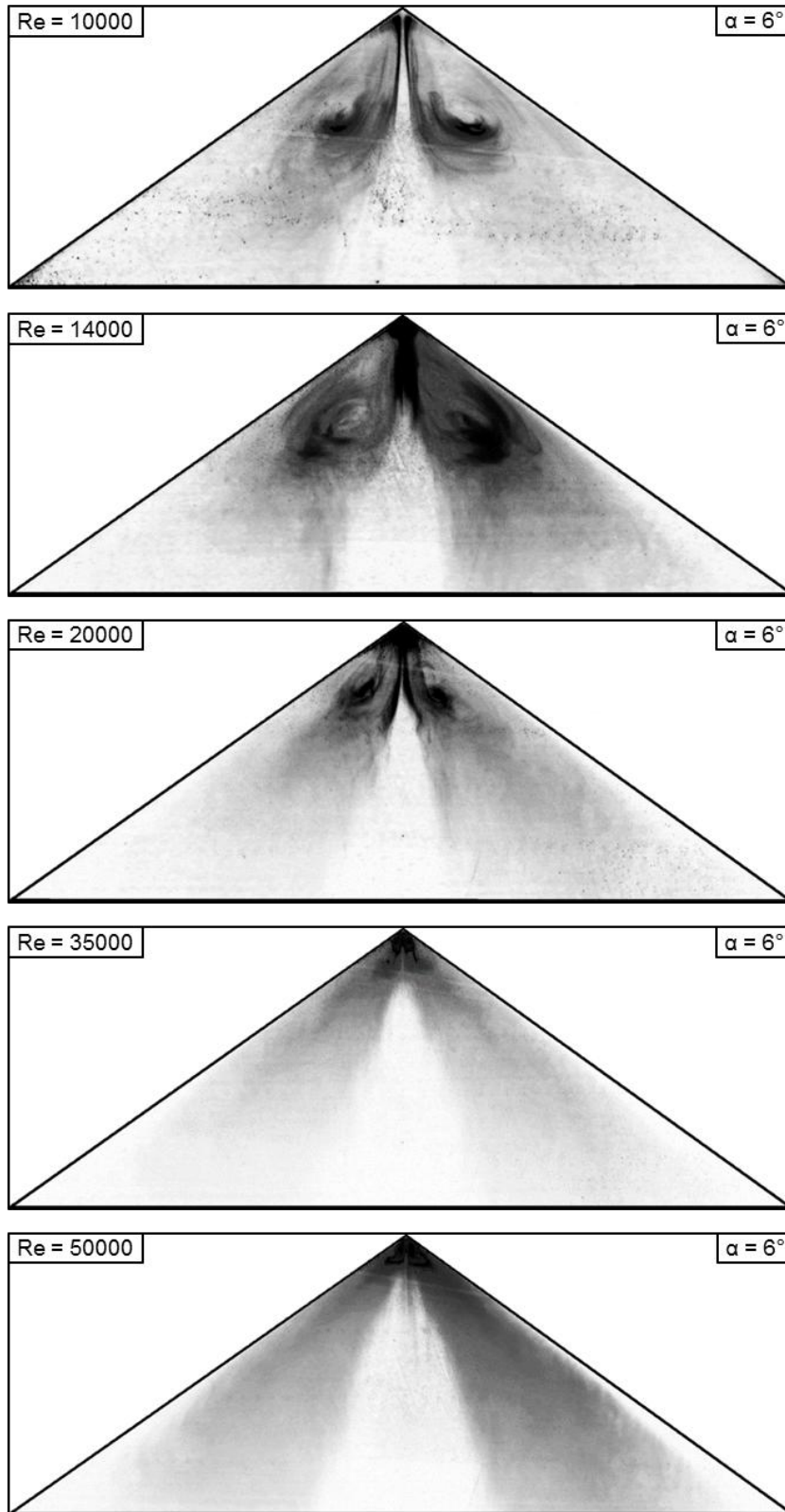


Figure 3-3 Surface flow visualizations at different Reynolds numbers and at $\alpha = 6^\circ$ angle of attack

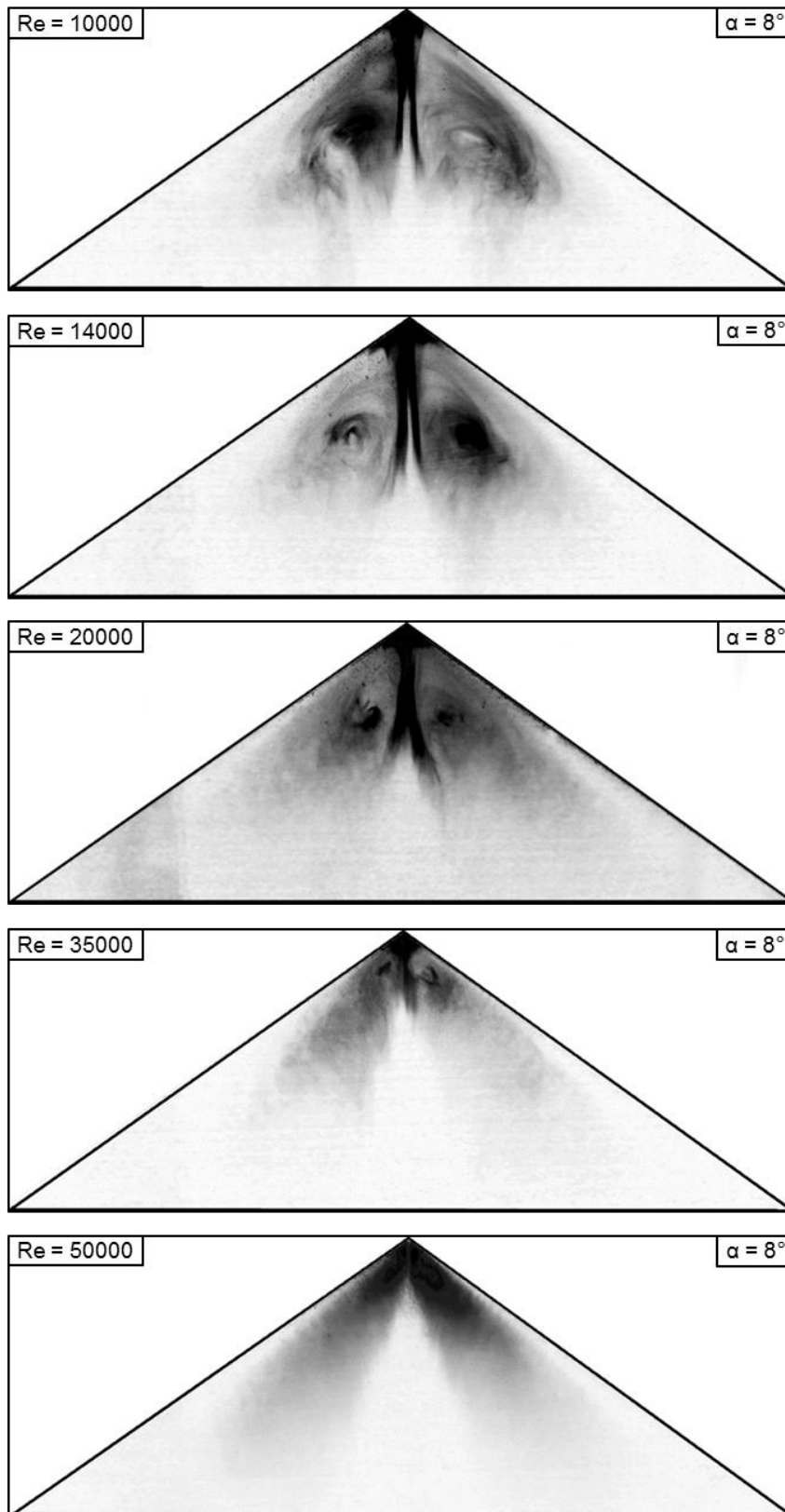


Figure 3-4 Surface flow visualizations at different Reynolds numbers and at $\alpha = 8^\circ$ angle of attack

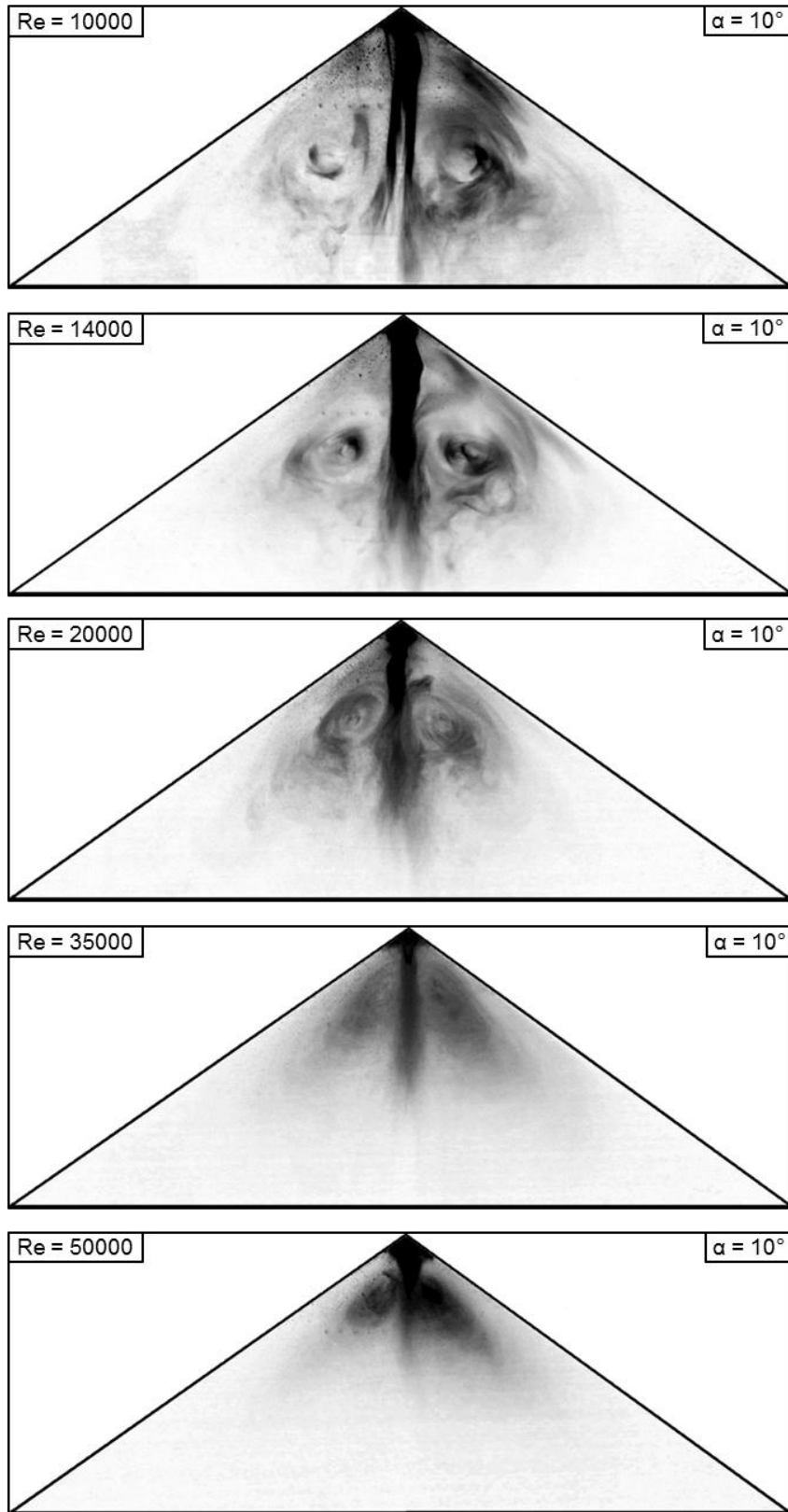


Figure 3-5 Surface flow visualizations at different Reynolds numbers and at $\alpha = 10^\circ$ angle of attack

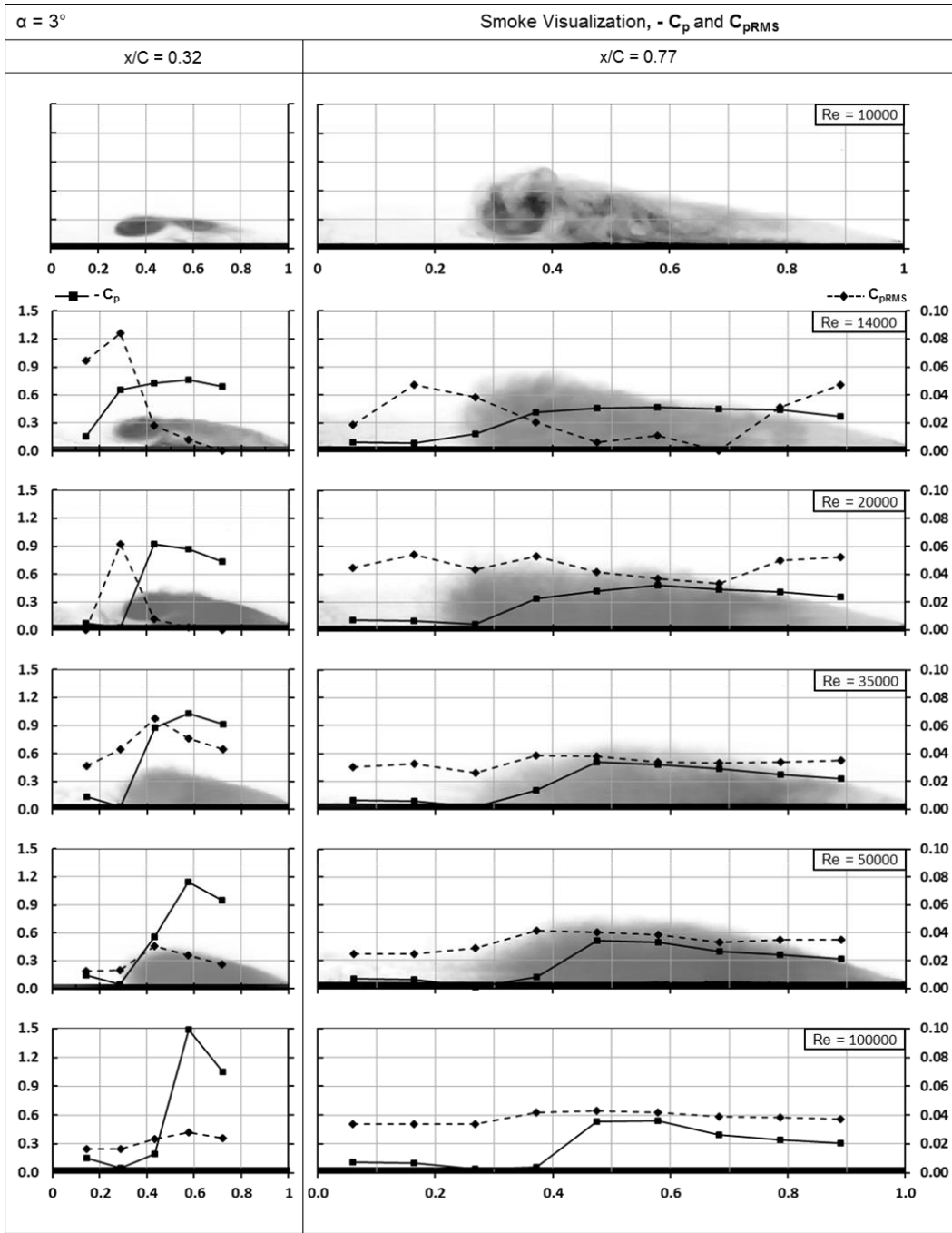


Figure 3-6 Cross flow visualization, spanwise $-C_p$ and C_{pRMS} plots on $x/C = 0.32$ and $x/C = 0.77$ chordwise distances at $\alpha = 3^\circ$ angle of attack and different Reynolds numbers

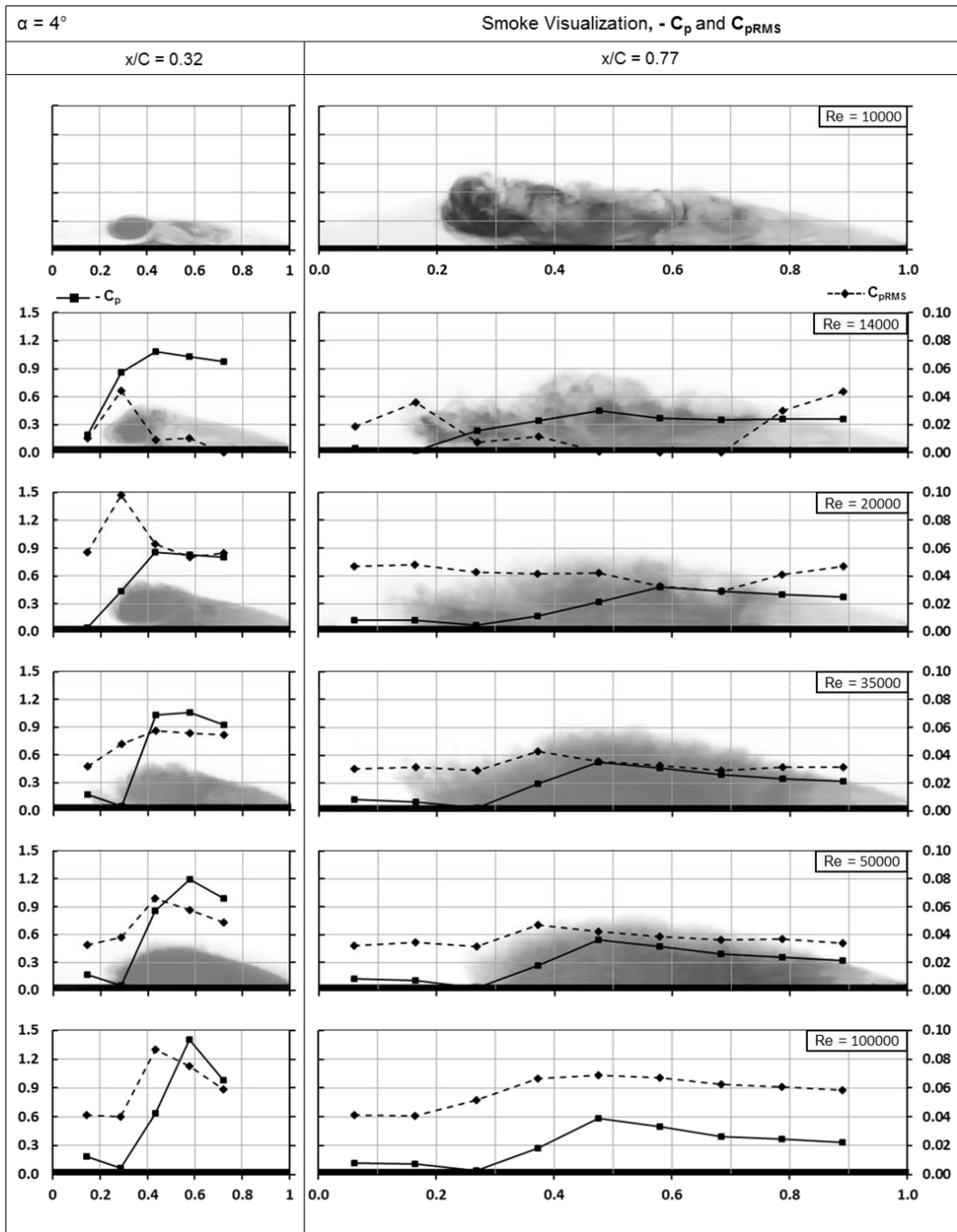


Figure 3-7 Cross flow visualization, spanwise $-C_p$ and C_{pRMS} plots on $x/C = 0.32$ and $x/C = 0.77$ chordwise distances at $\alpha = 4^\circ$ angle of attack and different Reynolds numbers

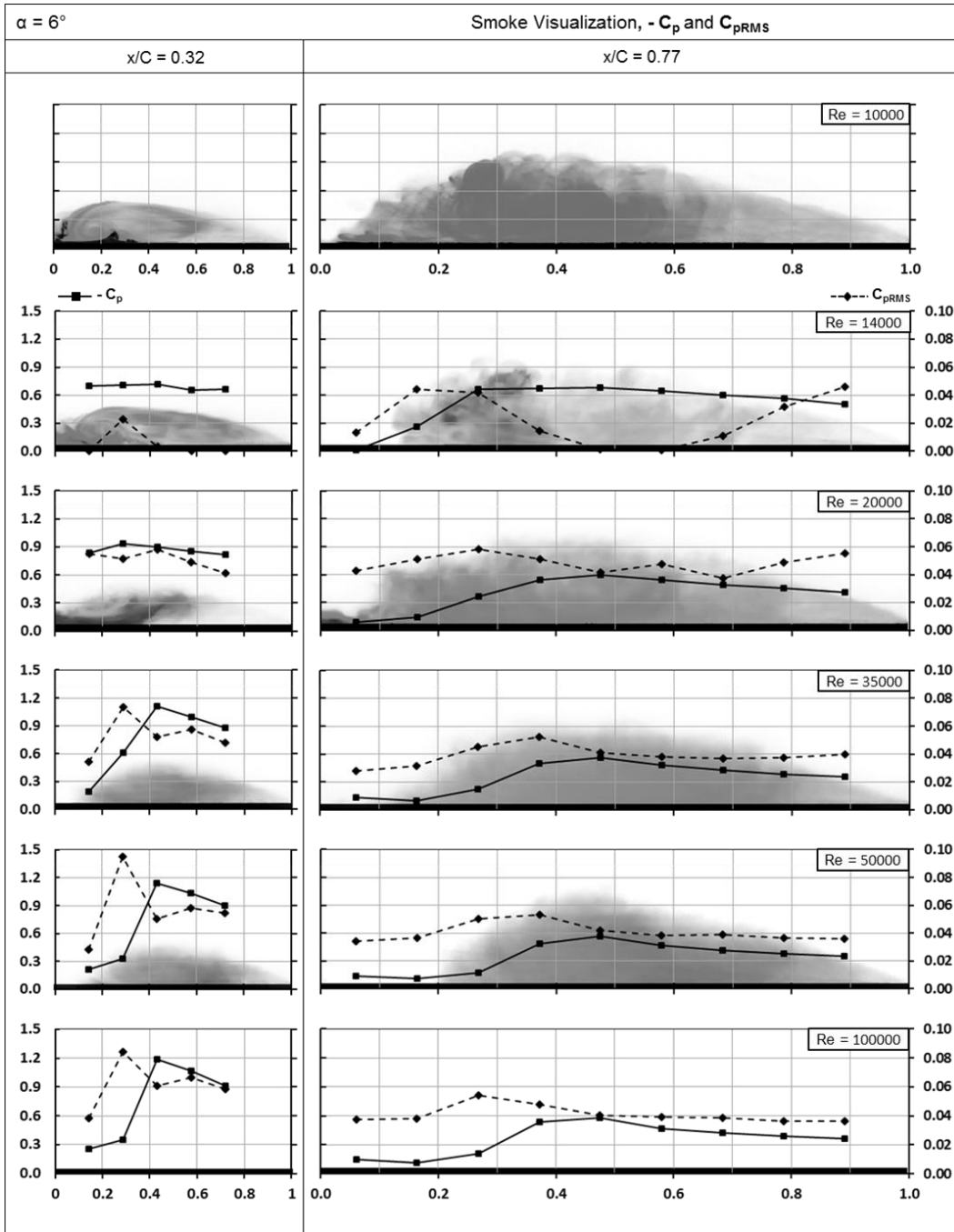


Figure 3-8 Cross flow visualization, spanwise $-C_p$ and C_{pRMS} plots on $x/C = 0.32$ and $x/C = 0.77$ chordwise distances at $\alpha = 6^\circ$ angle of attack and different Reynolds numbers

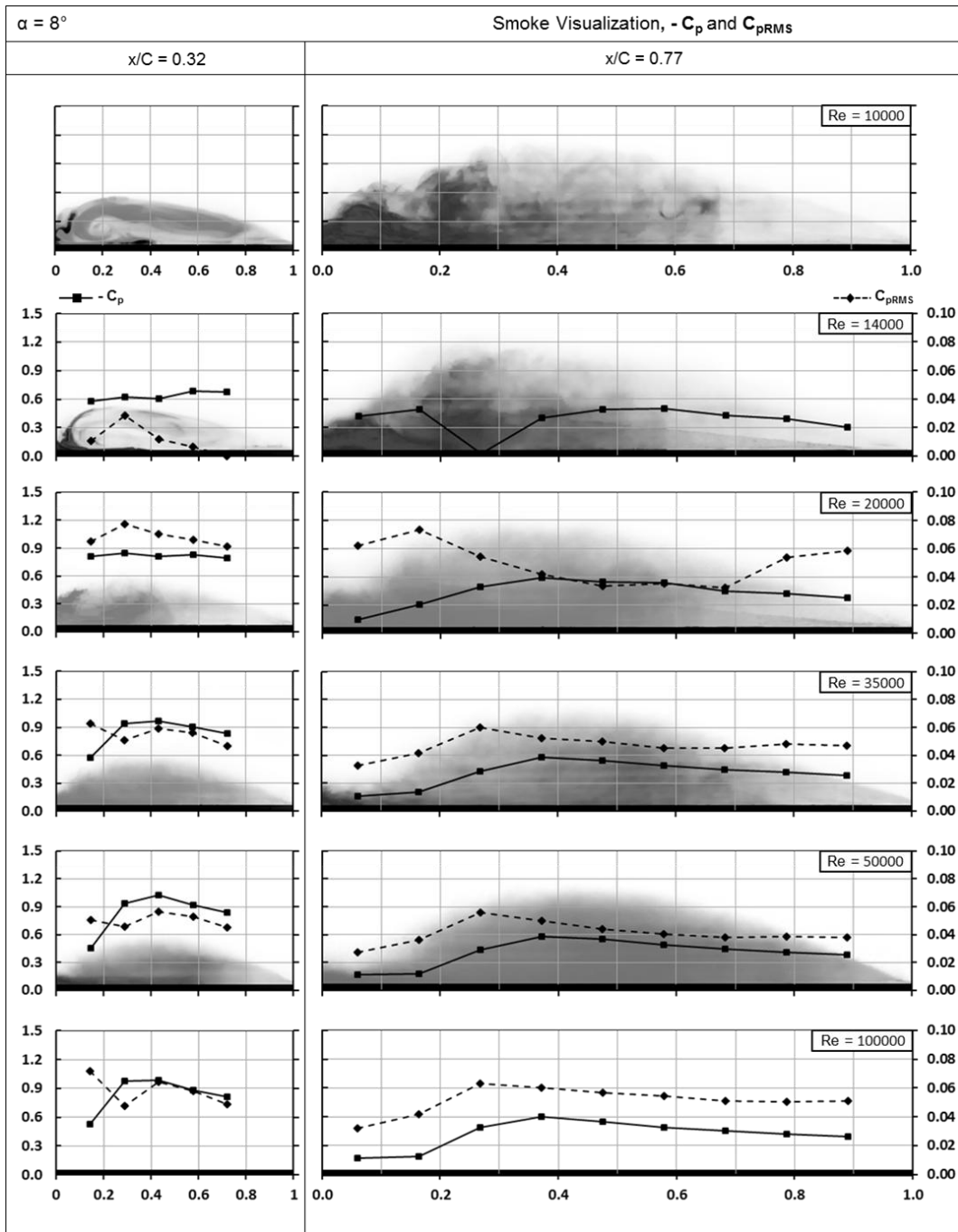


Figure 3-9 Cross flow visualization, spanwise $-C_p$ and C_{pRMS} plots on $x/C = 0.32$ and $x/C = 0.77$ chordwise distances at $\alpha = 8^\circ$ angle of attack and different Reynolds numbers

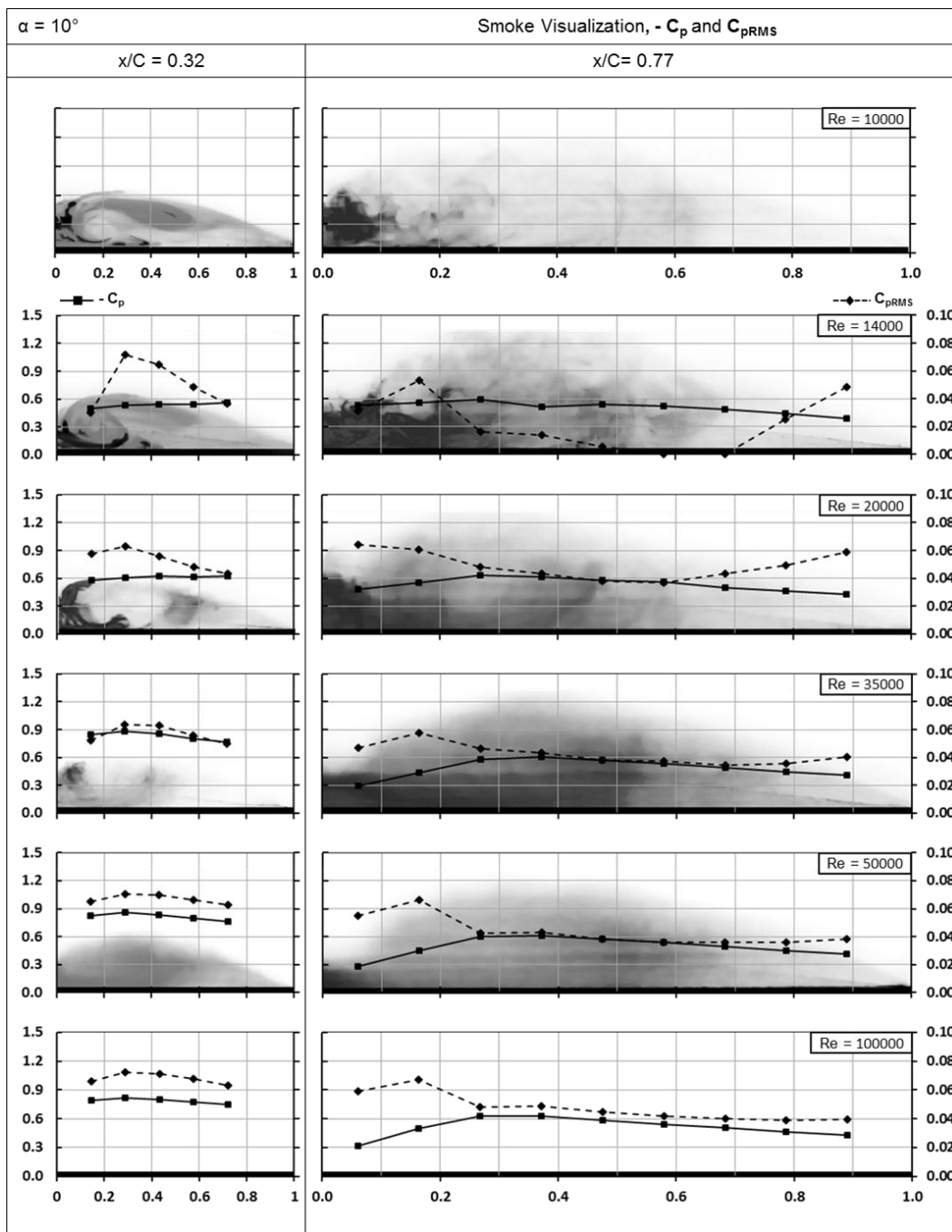


Figure 3-10 Cross flow visualization, spanwise $-C_p$ and C_{pRMS} plots on $x/C = 0.32$ and $x/C = 0.77$ chordwise distances at $\alpha = 10^\circ$ angle of attack and different Reynolds numbers

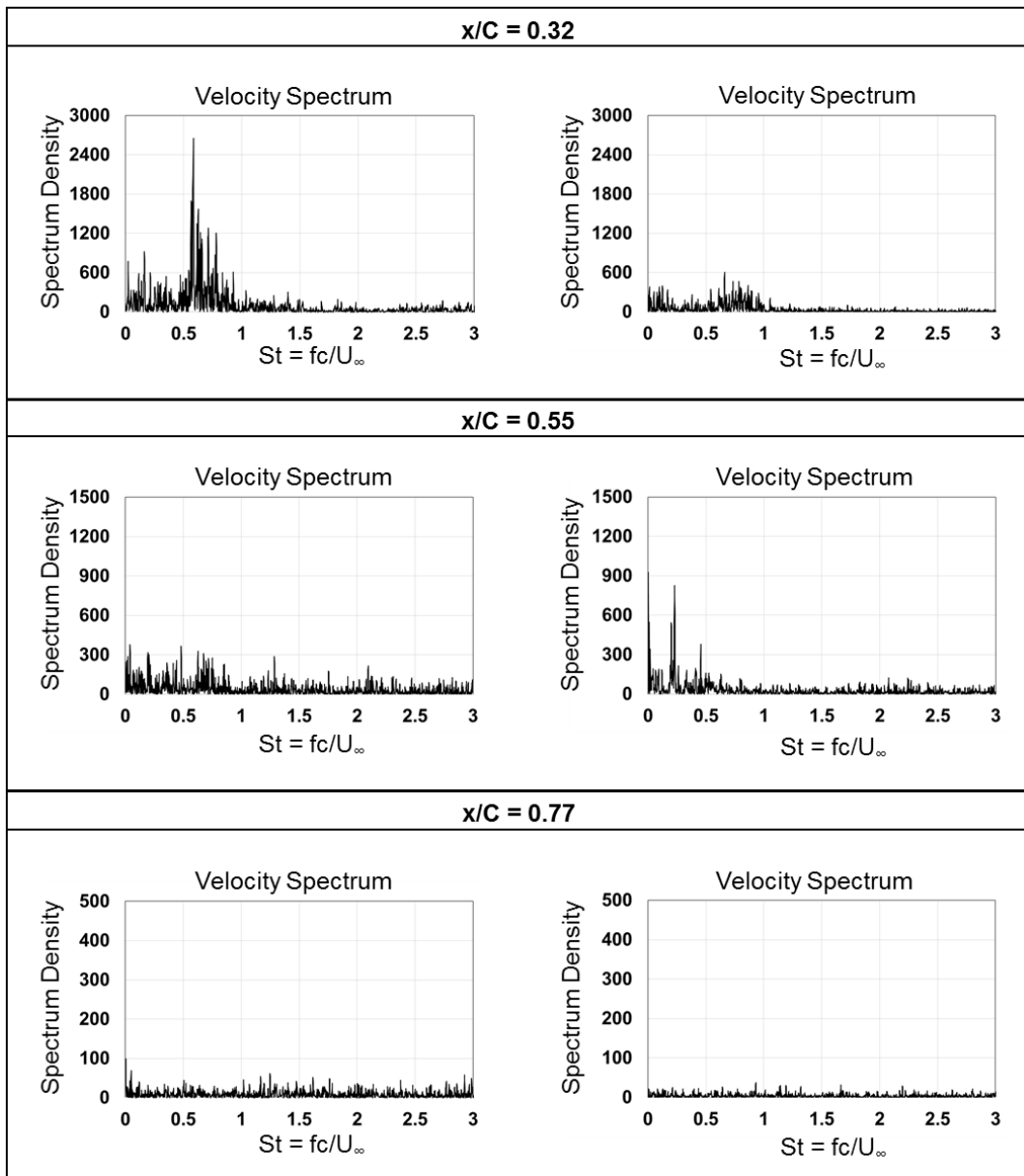
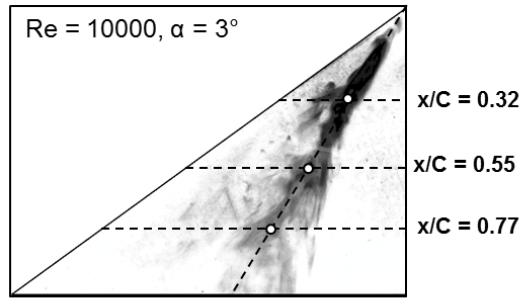


Figure 3-11 Spectral analysis results of velocities measured at vortex core in x and z directions at $\alpha = 3^\circ$ angle of attack and $Re = 10^4$ (u-dir. on the left and w-dir. on the right).

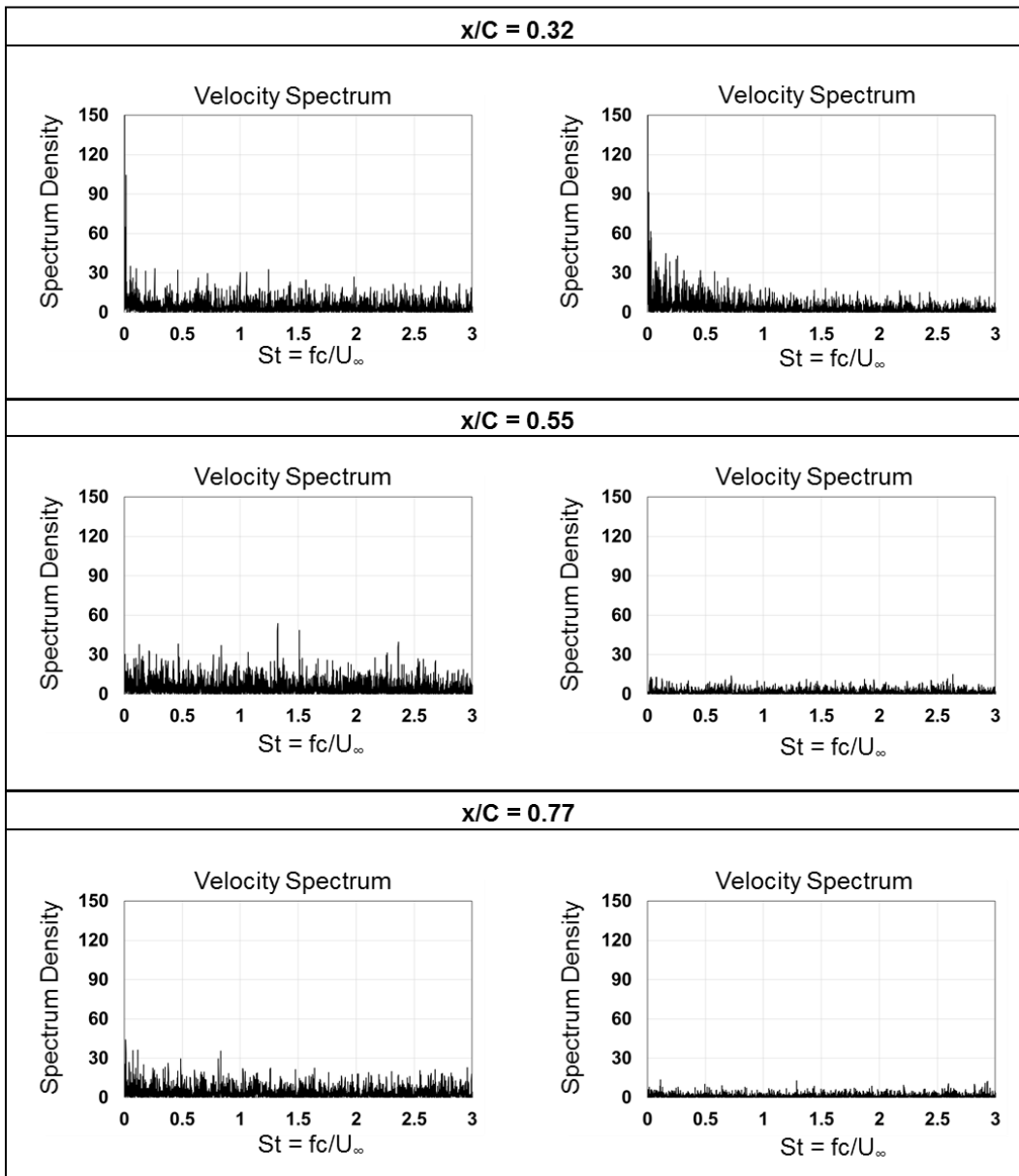
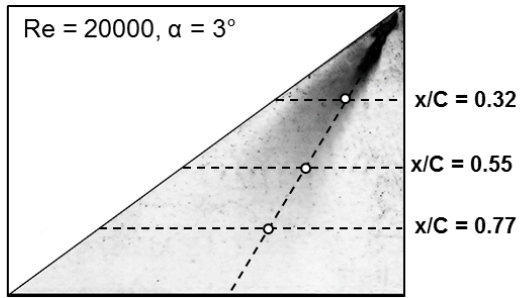


Figure 3-12 Spectral analysis results of velocities measured at vortex core in x and z directions at $\alpha = 3^\circ$ angle of attack and $Re = 2 \times 10^4$ (u-dir. on the left and w-dir. on the right).

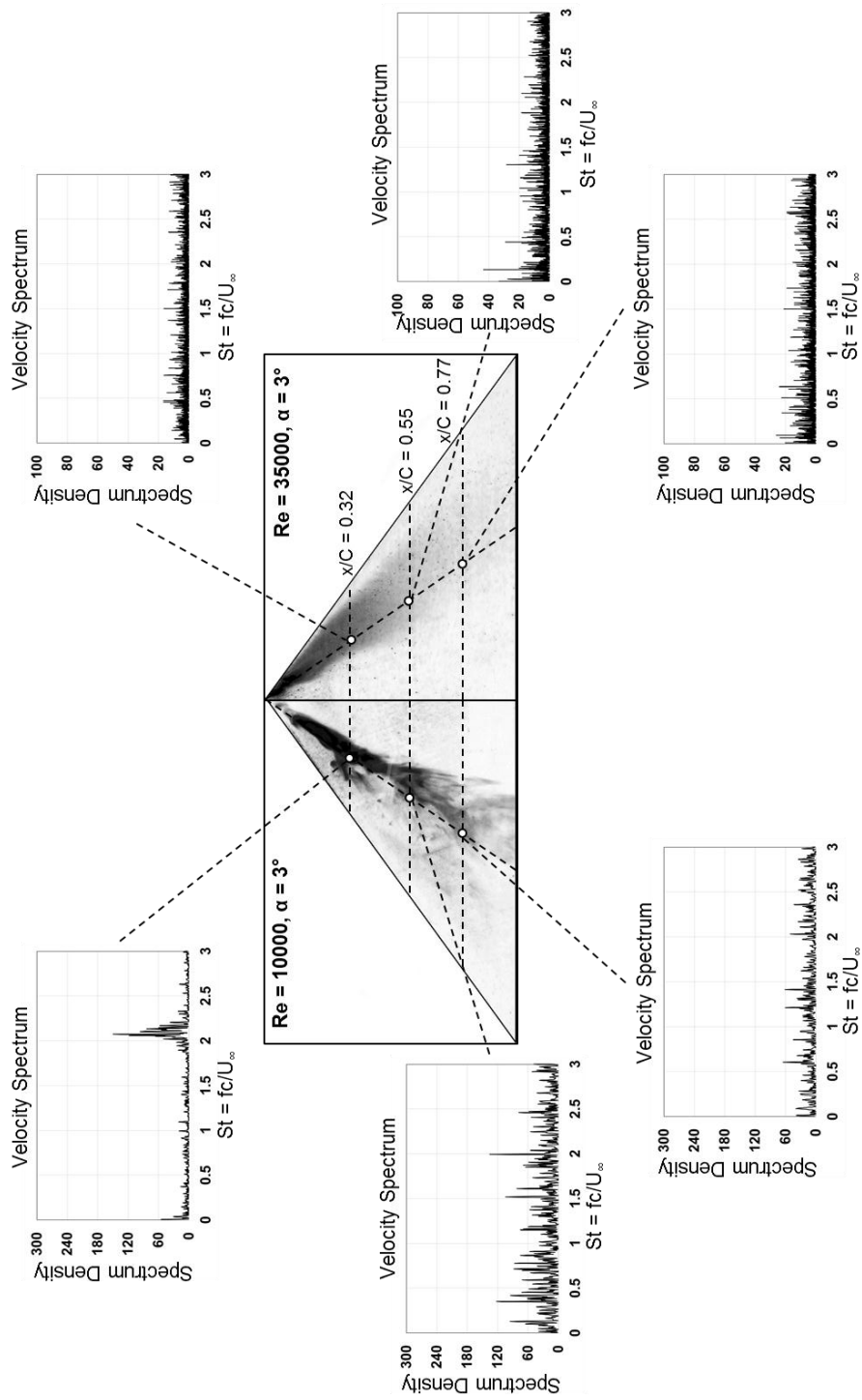


Figure 3-13 Spectral analysis results of velocities measured near the surface in x direction at $\alpha = 3^\circ$ angle of attack and $Re = 10^4$ (left) and $Re = 3.5 \times 10^4$ (right)

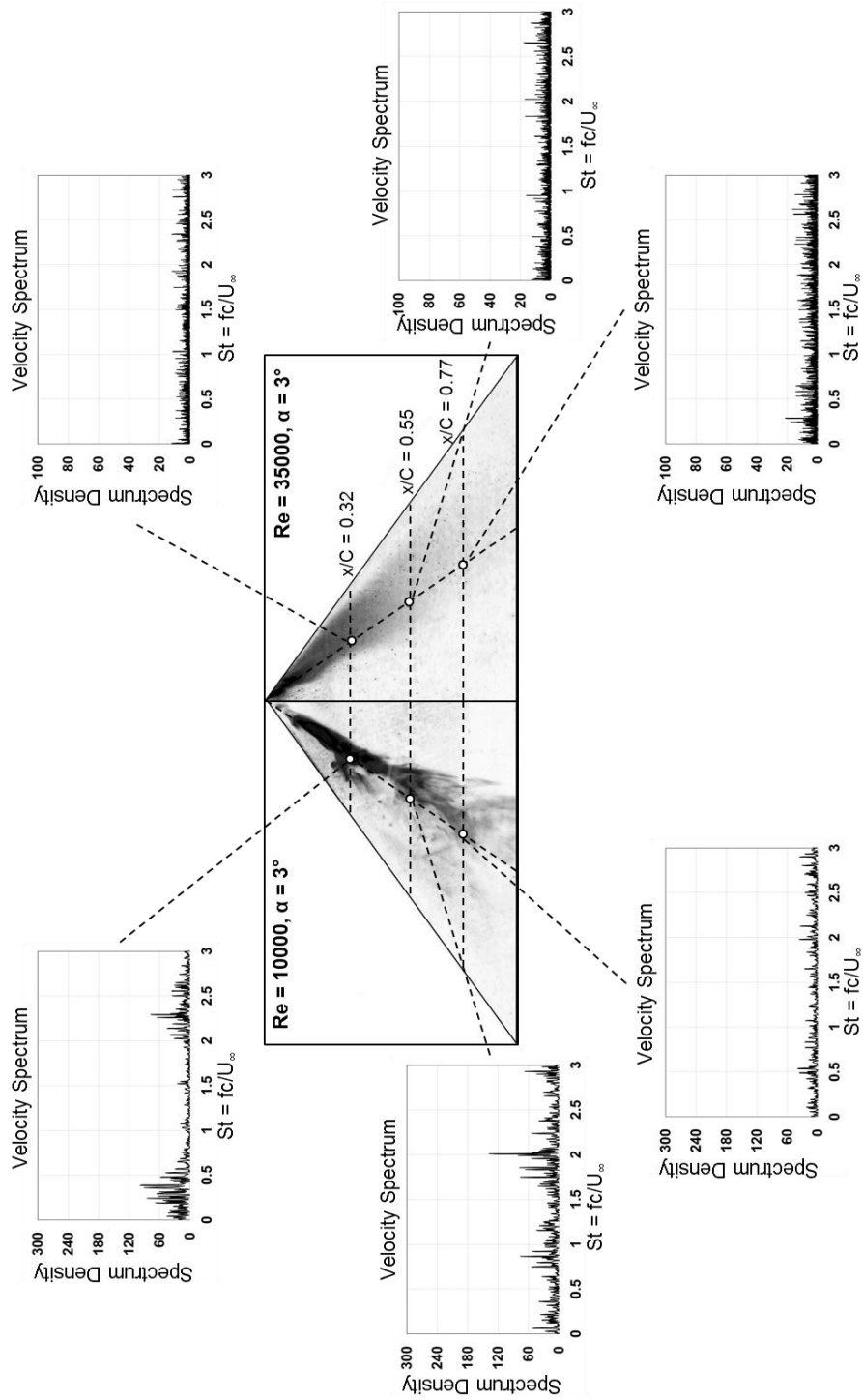


Figure 3-14 Spectral analysis results of velocities measured near the surface in z direction at $\alpha = 3^\circ$ angle of attack and $Re = 10^4$ (left) and $Re = 3.5 \times 10^4$ (right)

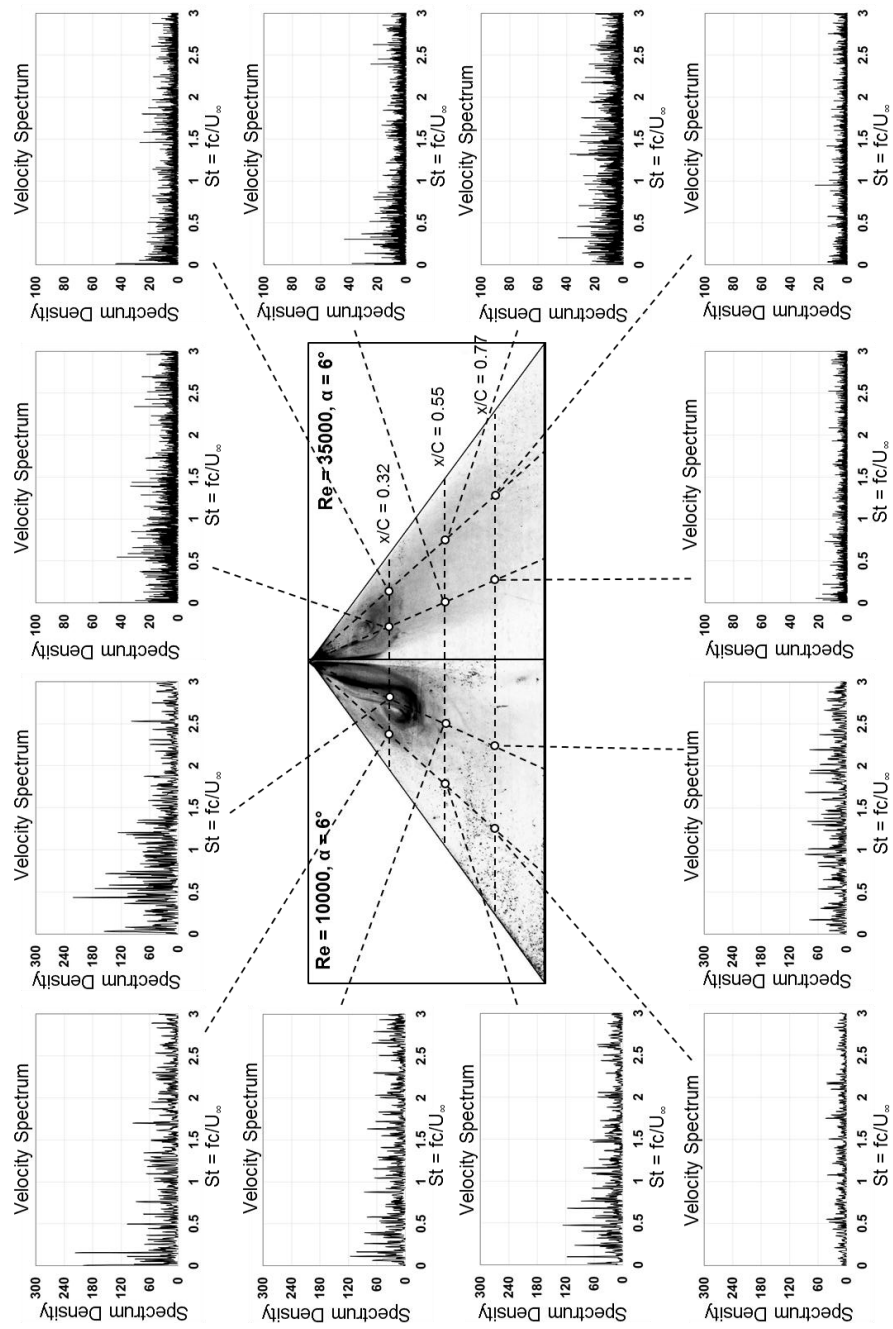


Figure 3-15 Spectral analysis results of velocities measured near the surface in x direction at $\alpha = 6^\circ$ angle of attack and $Re = 10^4$ (left) and $Re = 3.5 \times 10^4$ (right)

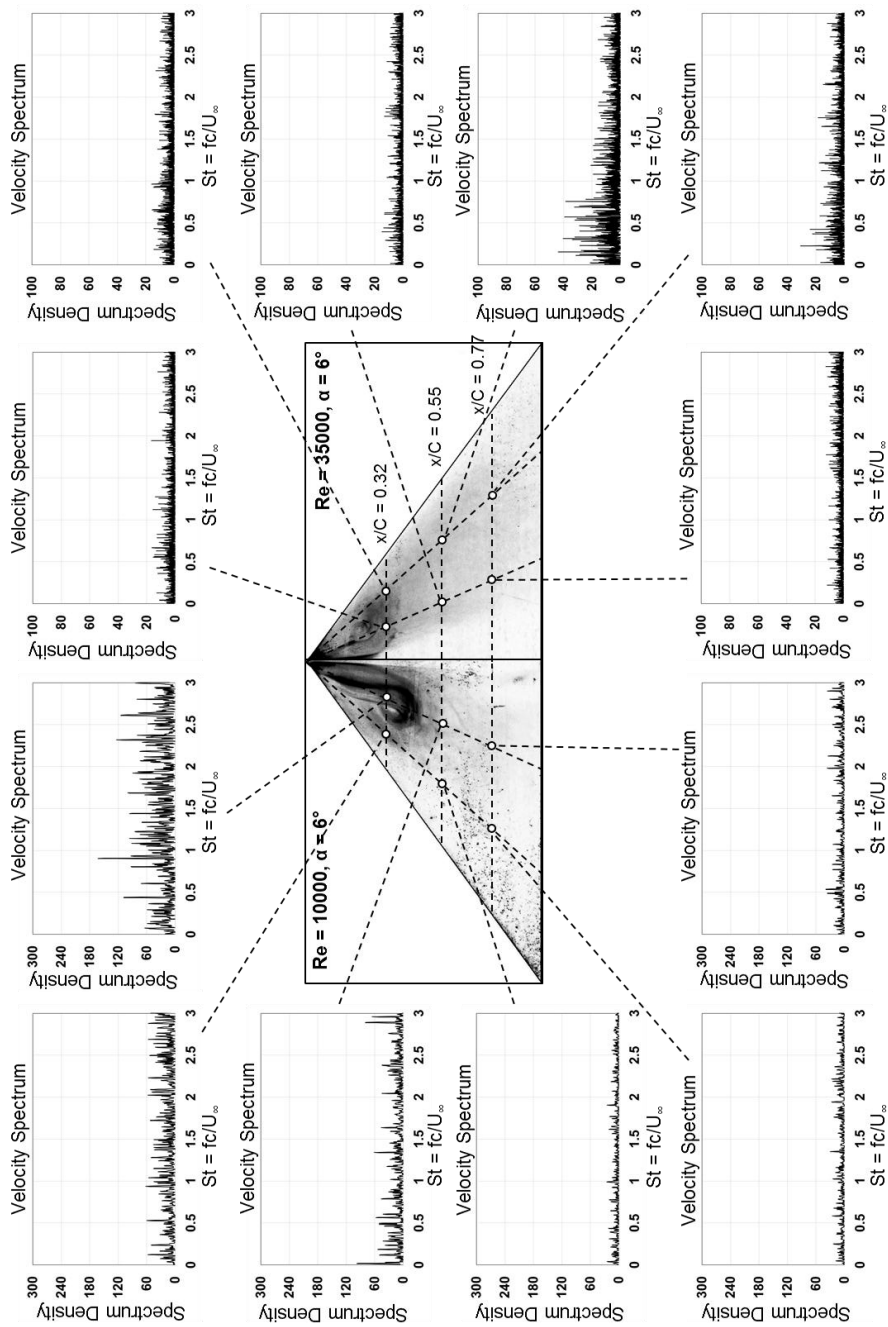


Figure 3-16 Spectral analysis results of velocities measured near the surface in z direction at $\alpha = 6^\circ$ angle of attack and $Re = 10^4$ (left) and $Re = 3.5 \times 10^4$ (right)

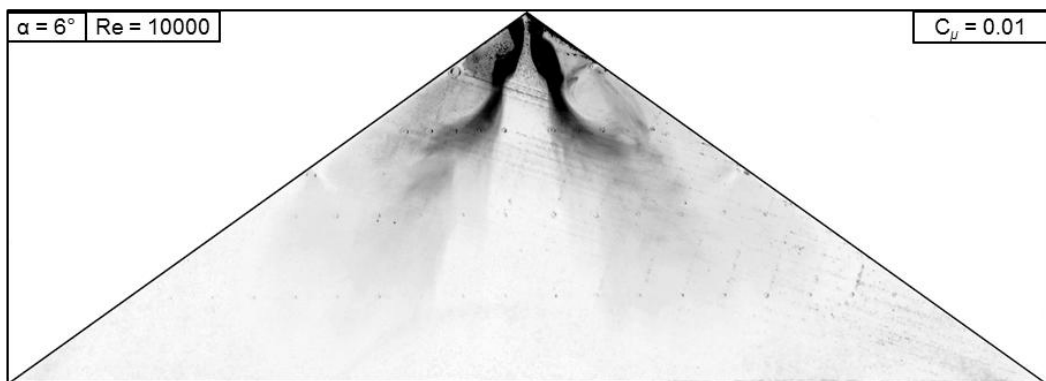
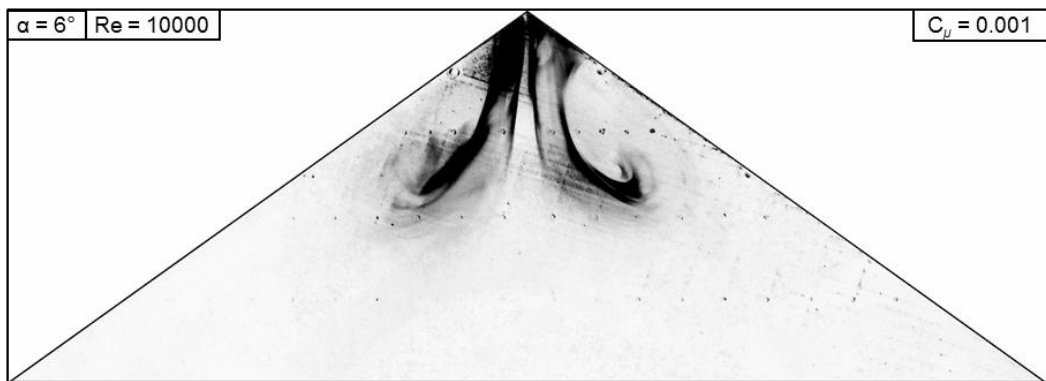
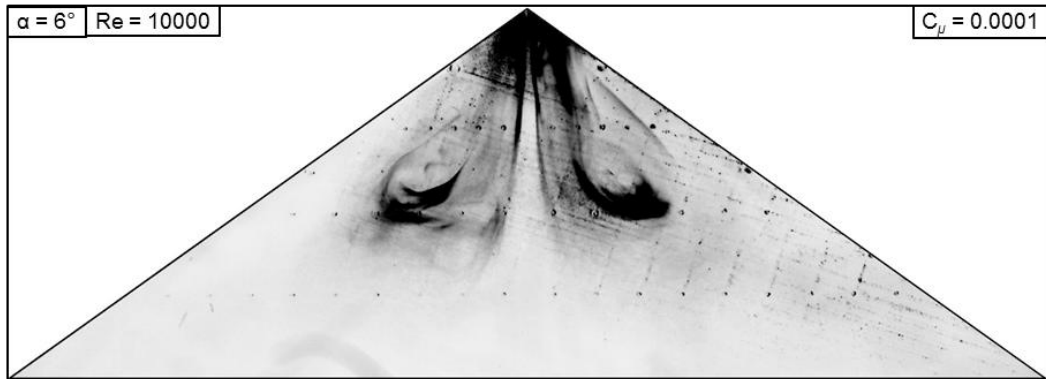
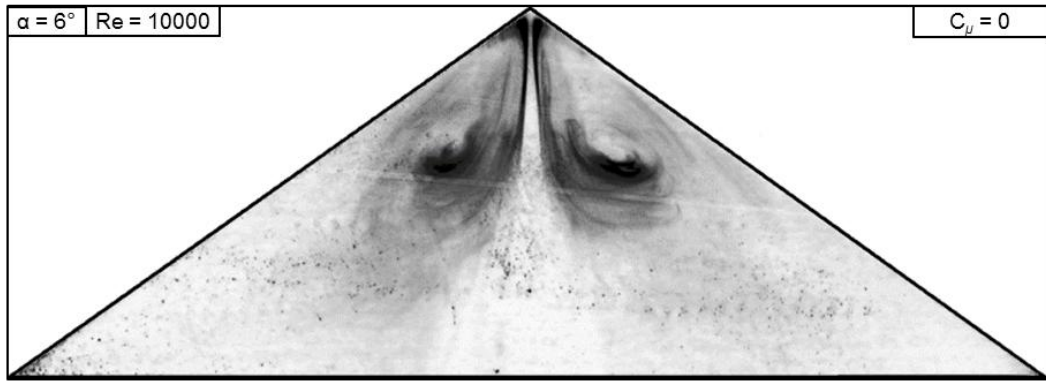


Figure 3-17 Surface flow visualization at $\alpha = 6^\circ$ angle of attack, $Re = 10^4$ and at different momentum coefficients

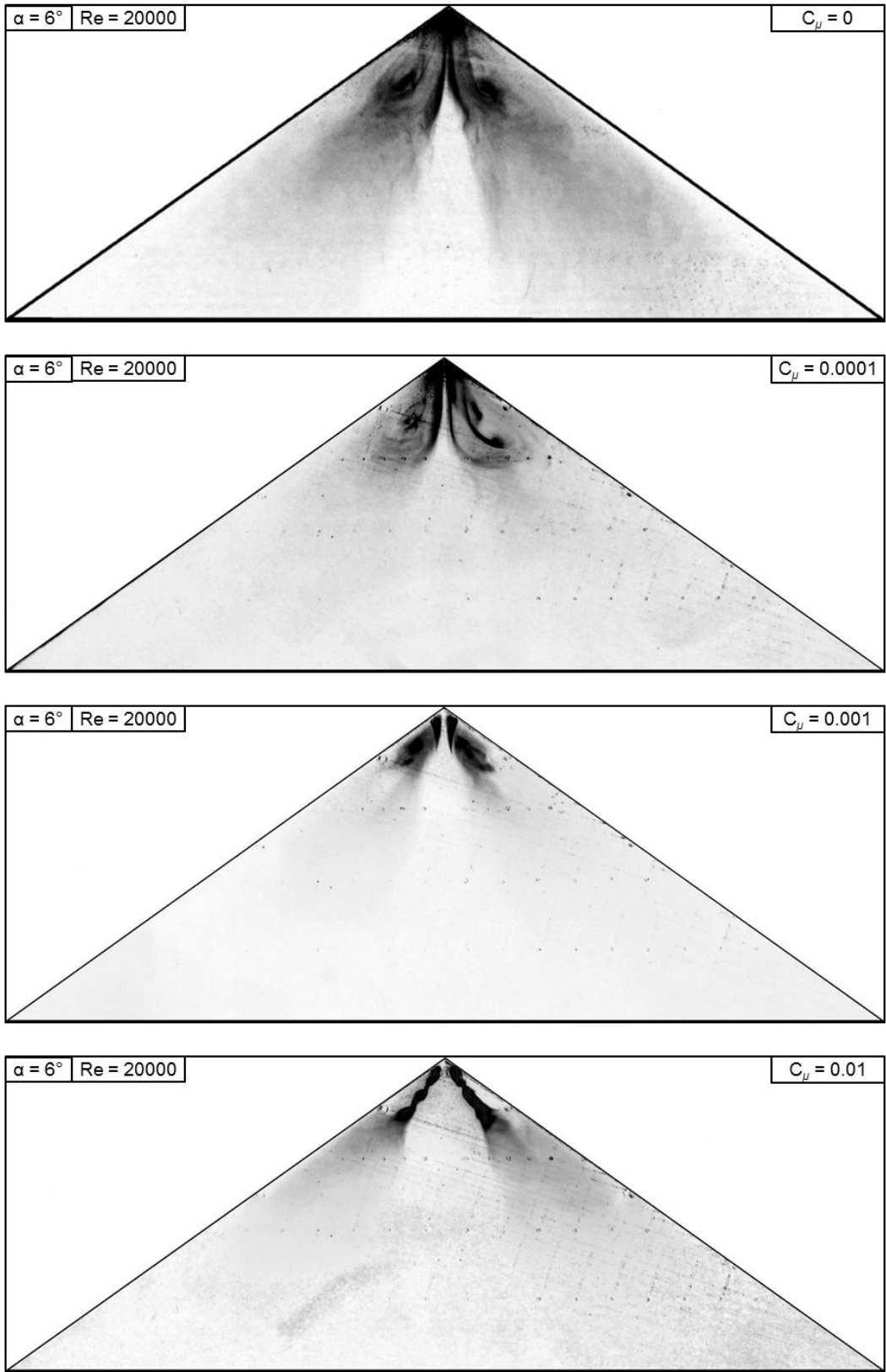


Figure 3-18 Surface flow visualization at $\alpha = 6^\circ$ angle of attack, $Re = 2 \times 10^4$ and at different momentum coefficients

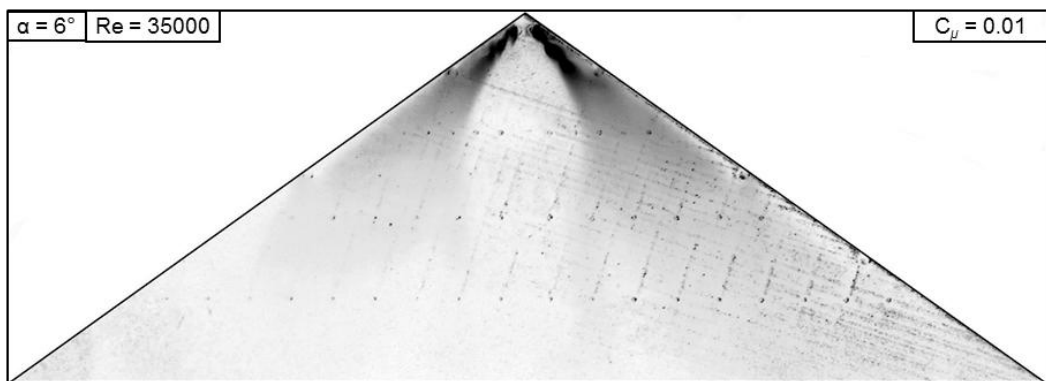
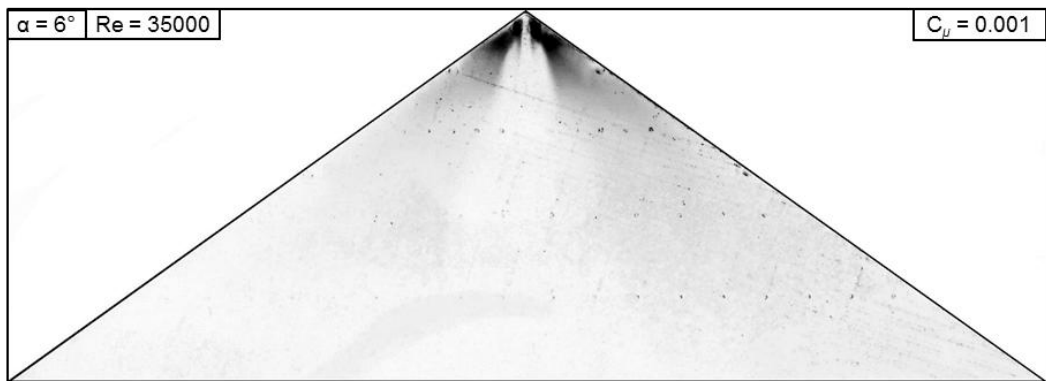
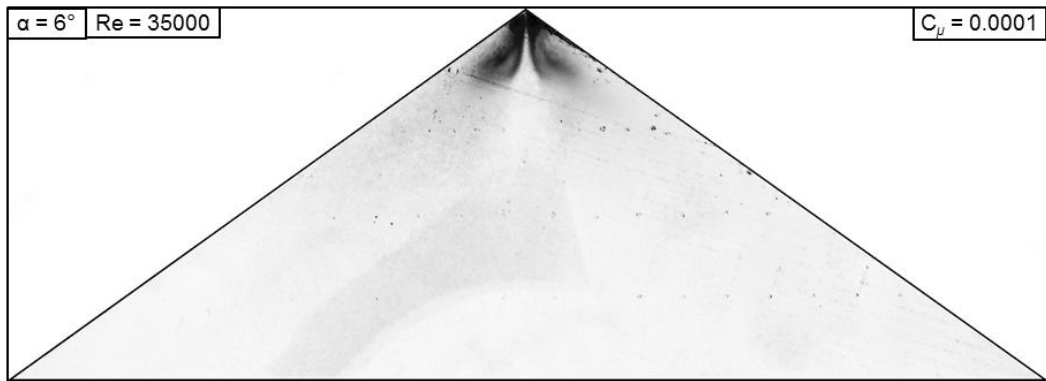
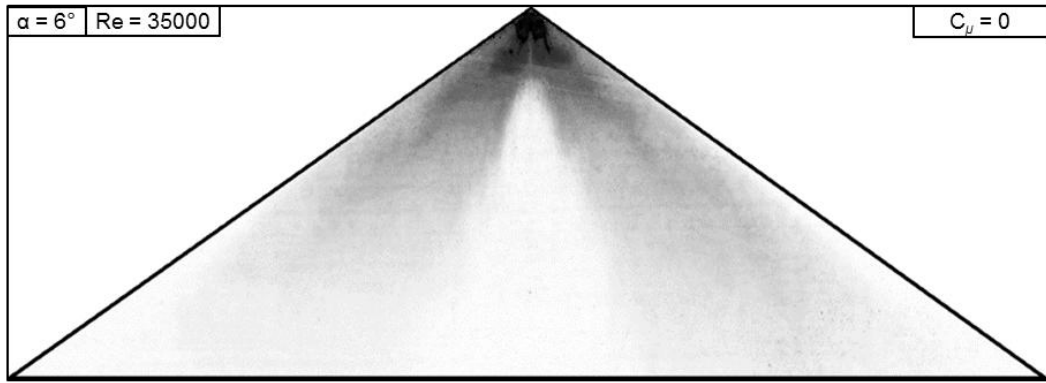


Figure 3-19 Surface flow visualization at $\alpha = 6^\circ$ angle of attack, $Re = 3.5 \times 10^4$ and at different momentum coefficients

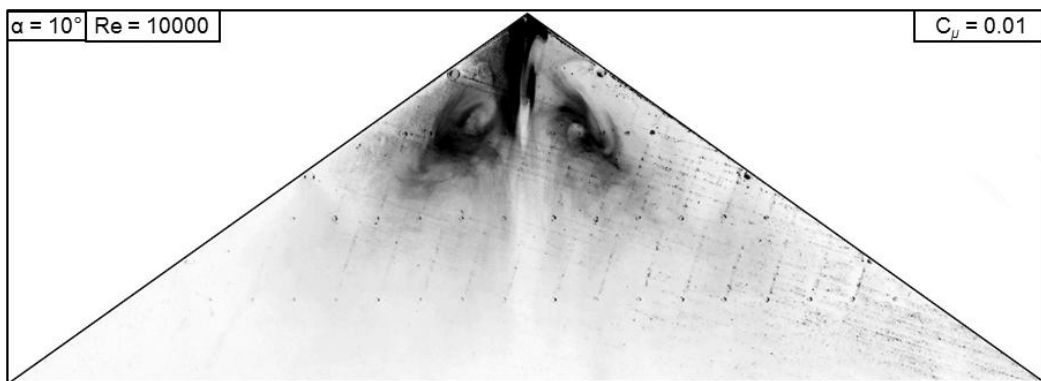
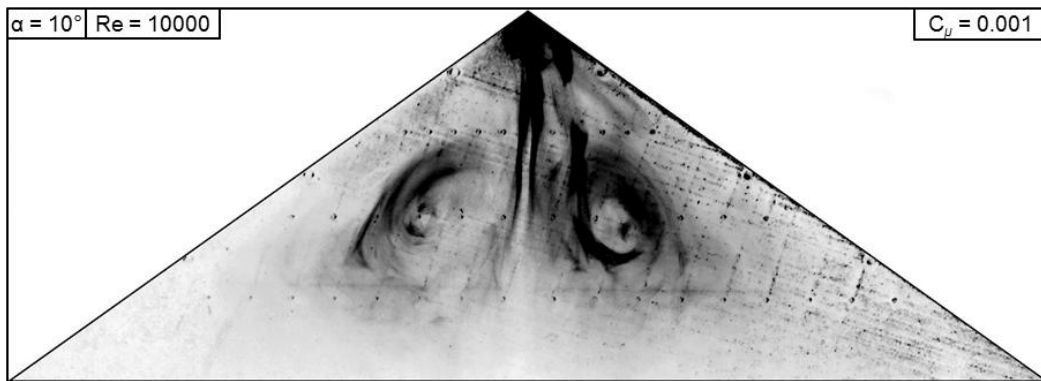
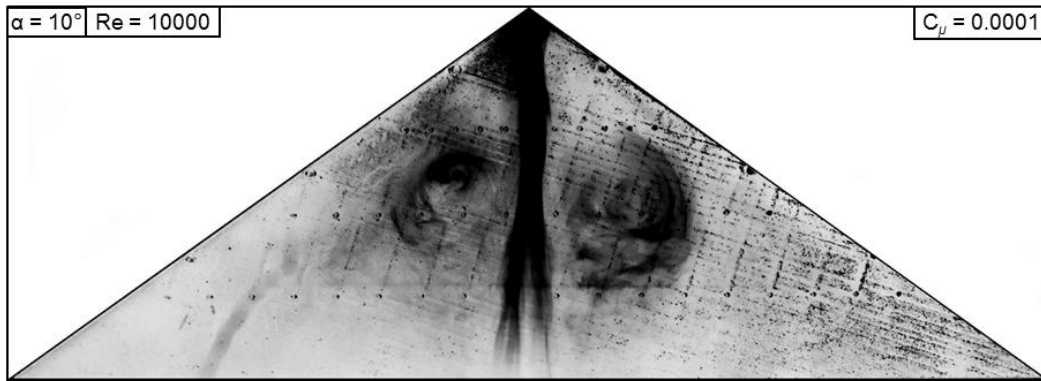
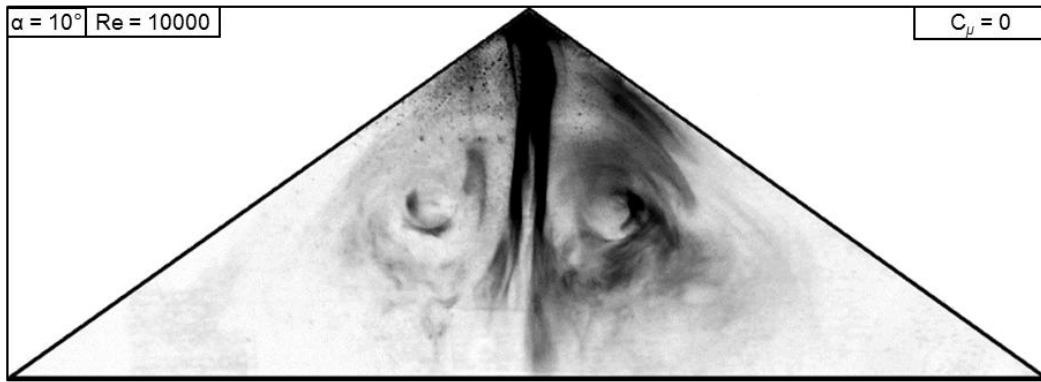


Figure 3-20 Surface flow visualization at $\alpha = 10^\circ$ angle of attack, $Re = 10^4$ and at different momentum coefficients

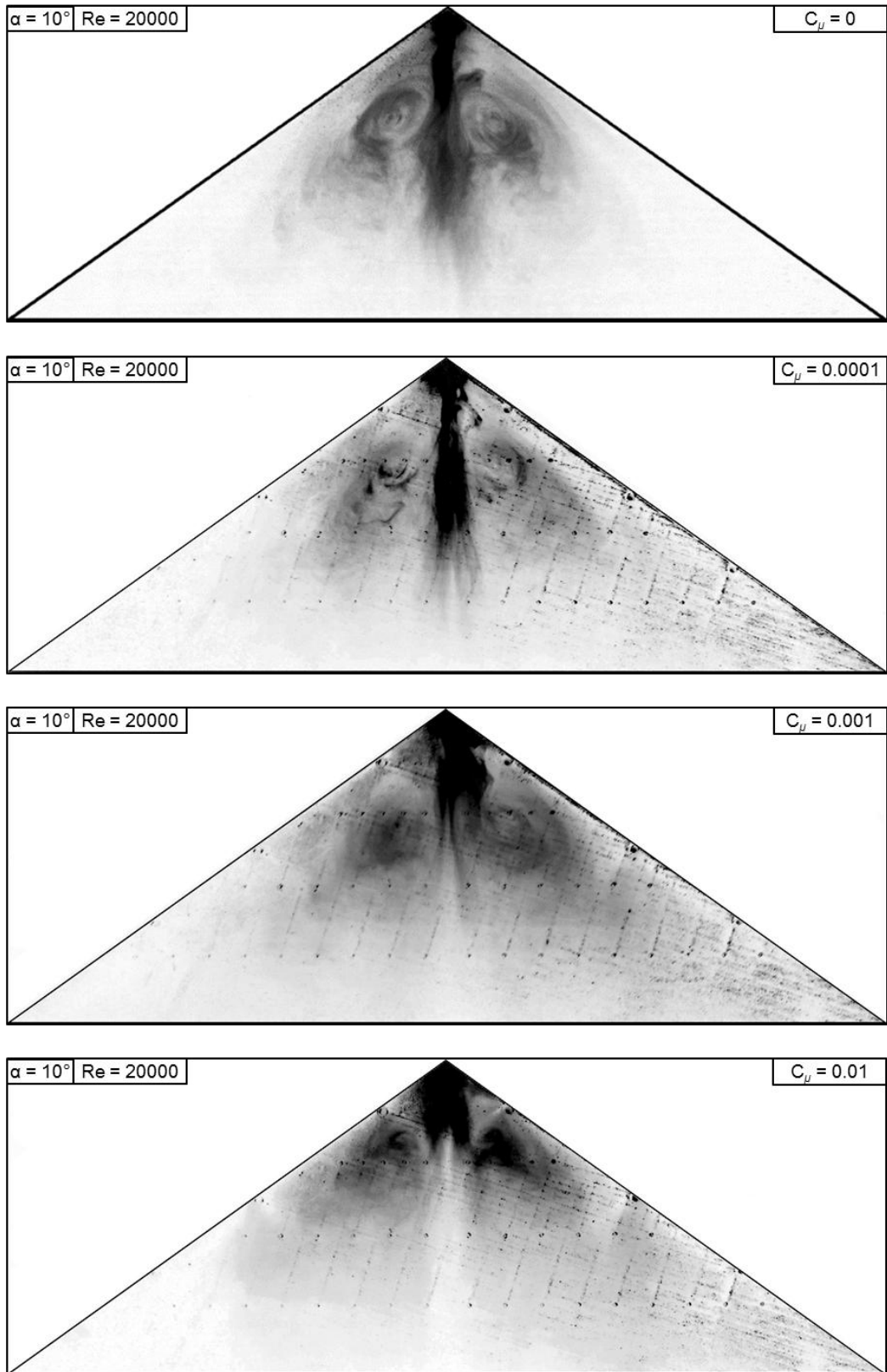


Figure 3-21 Surface flow visualization at $\alpha = 10^\circ$ angle of attack, $Re = 2 \times 10^4$ and at different momentum coefficients

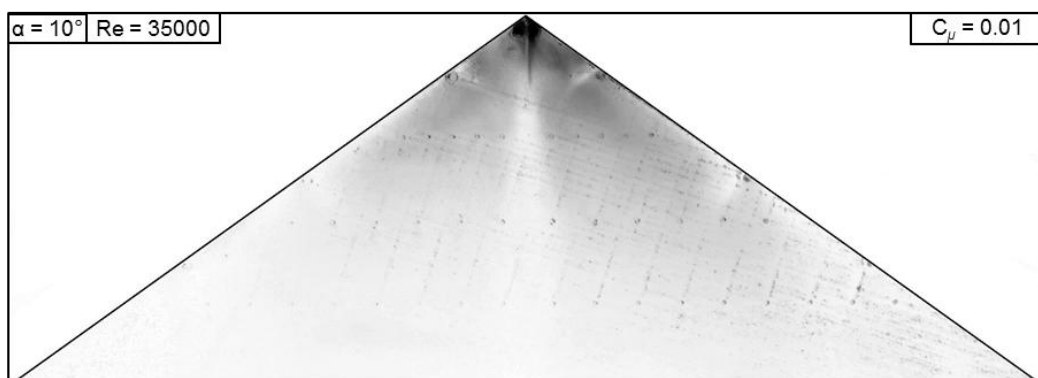
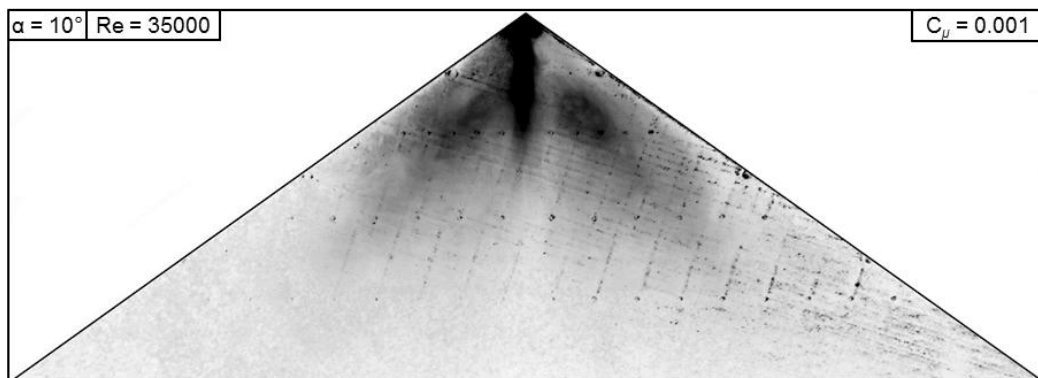
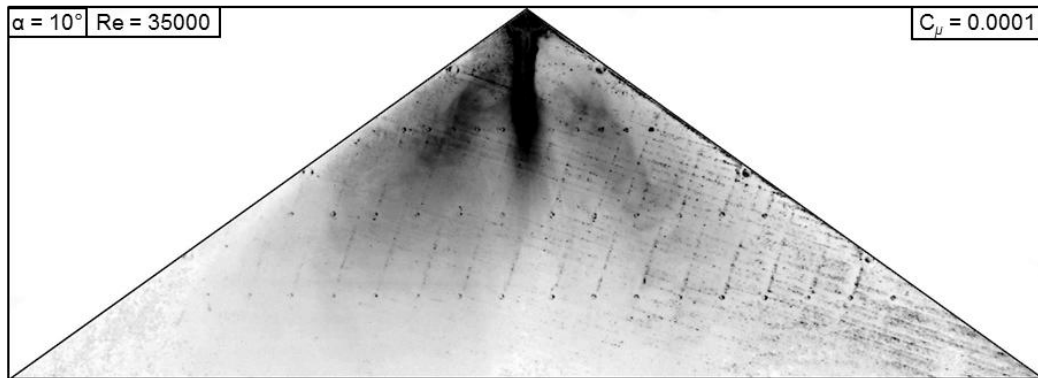
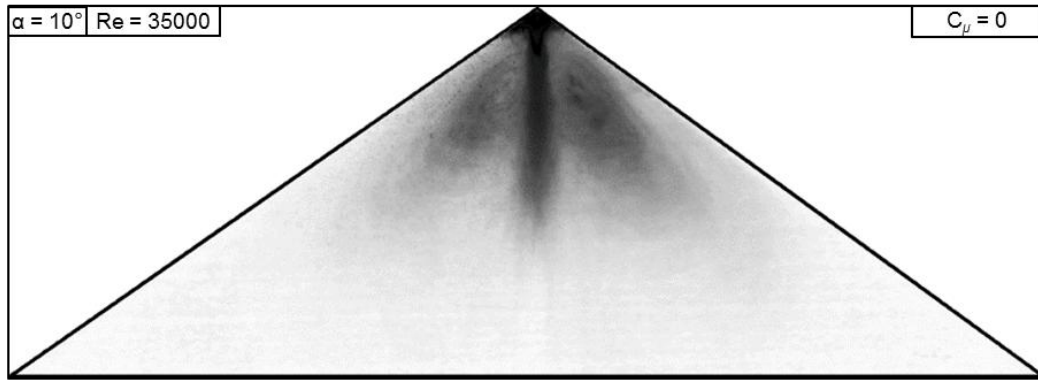


Figure 3-22 Surface flow visualization at $\alpha = 10^\circ$ angle of attack, $Re = 3.5 \times 10^4$ and at different momentum coefficients

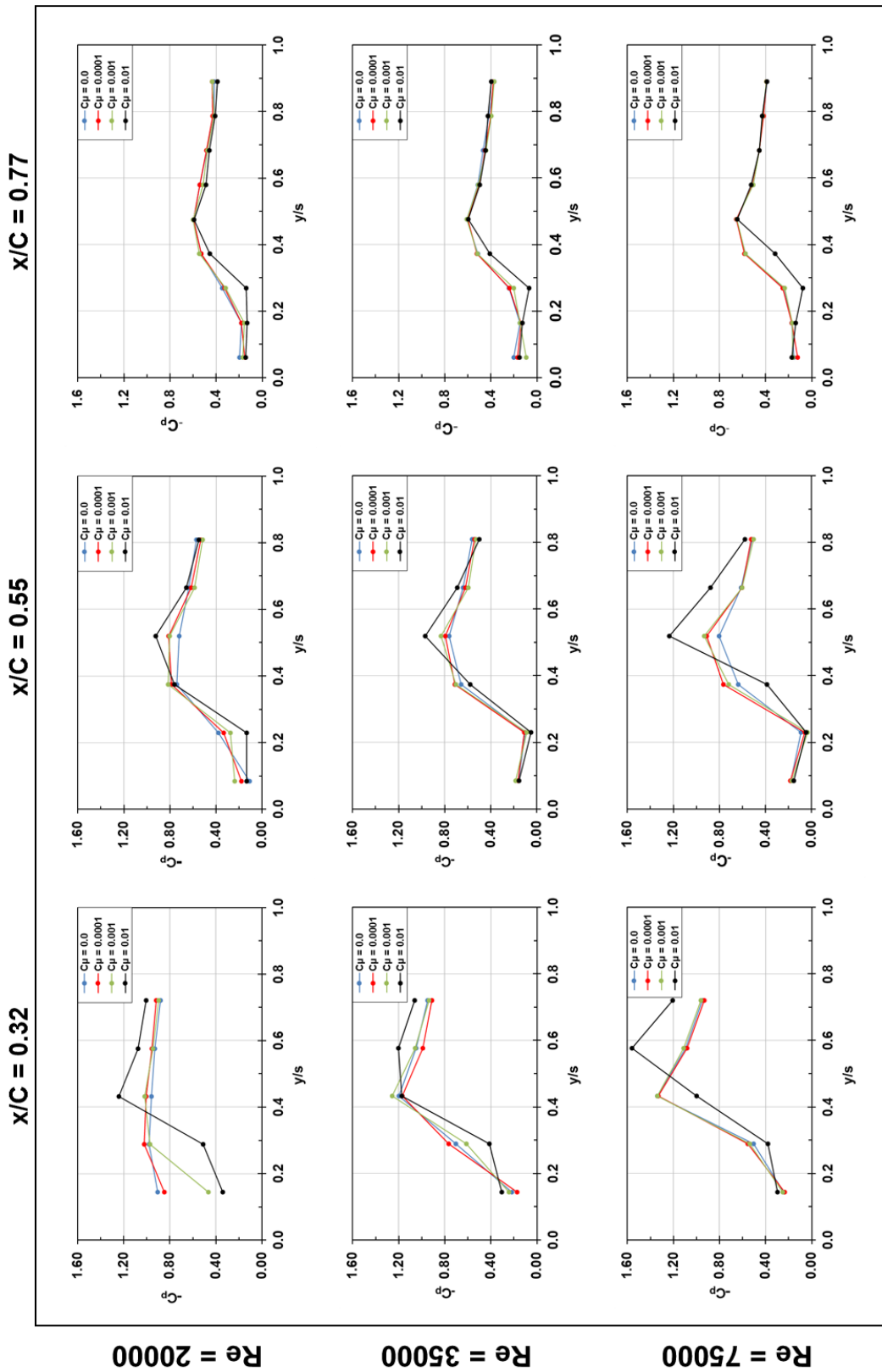


Figure 3-23 Spanwise $-C_p$ plots at $\alpha = 6^\circ$ angle of attack on chordwise distances of $x/C = 0.32$, 0.55 and 0.77 and different Reynolds numbers

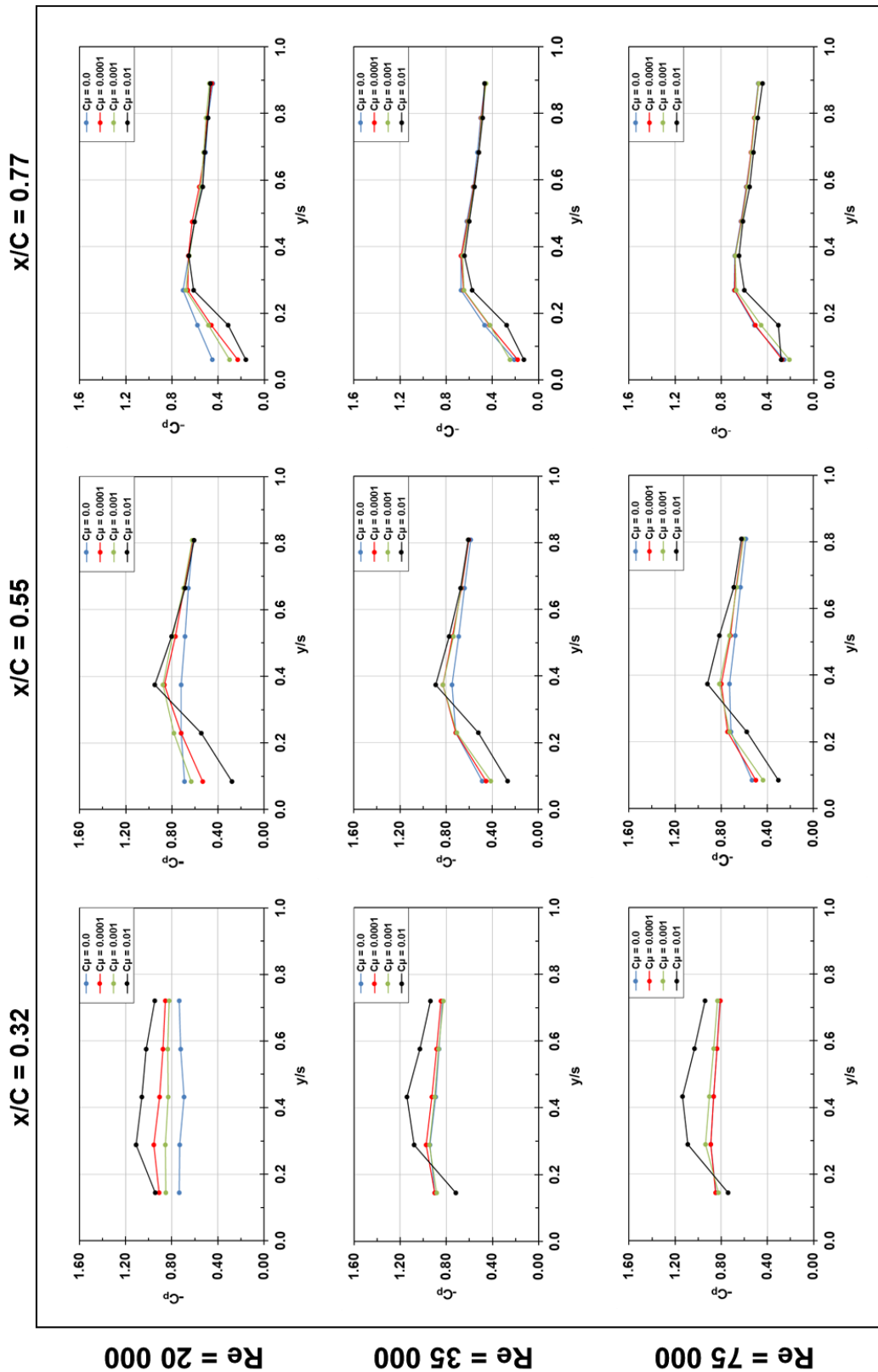


Figure 3-24 Spanwise $-C_p$ plots at $\alpha = 10^\circ$ angle of attack on chordwise distances of $x/C = 0.32, 0.55$ and 0.77 and different Reynolds number

CHAPTER 4

CONCLUSION AND FUTURE WORK

4.1. Conclusion

This present study aims to investigate the flow structure on a low swept delta wing of $\Lambda = 35^\circ$ and the effect of active flow control technique using steady blowing through the leading edge of the wing. The experiments were conducted to study the effect attack angle from $\alpha = 3^\circ$ to $\alpha = 10^\circ$ and Reynolds number from $Re = 10^4$ to $Re = 10^5$. Laser illuminated smoke based flow visualization technique was used at three cross flow planes corresponding to pressure measurement stations and also at a plane passing through the core of leading edge vortices. Quantitative analysis was applied on the velocity data collected by Laser Doppler Anemometry (LDA) technique at the core of leading edge vortices and also at the points with a normal distance of 5 mm from wing surface. Mean and unsteady pressure measurements were also performed at three different chordwise distances. The power spectral densities of velocity measurements were computed to understand the unsteady behavior of the flow in detail. Furthermore, air has been blown from wing leading edge at different flow rates corresponding to momentum coefficients of 0.0001 , 0.001 and 0.01 . Effect of blowing was investigated for attack angles of $\alpha = 6^\circ$ and $\alpha = 10^\circ$ for the range of Reynolds number from $Re = 10^4$ to 7.5×10^4 .

From the study that has been carried out, the following main conclusions have been achieved:

- The location of vortex breakdown moves upstream toward apex of the wing by increasing Reynolds number at angle of attacks that leading edge vortices exist.
- At the angles attack corresponding to stall conditions, increasing Reynolds number leads to reduction in the size on the wing surface that is covered by three-dimensional separated flow structure. In contrary, with increasing angle of attack this swirling pattern extends towards the trailing edge on the wing surface.
- As seen in Taylor and Gursul's [7] study, the flow reaches to an asymptotic condition at the Reynolds numbers higher than a specific value. As a result, further increase in Reynolds number does not cause a considerable influence on the flow structure.
- The peaks of suction pressure that represent core of leading edge vortices decreases along the chord. Significant reduction in suction pressures are witnessed downstream of the vortex breakdown location.
- The highest pressure fluctuations occur between the reattachment region and the leading edge vortex core at vortical structures.
- The spectra of velocity measurements at vortex core contains relatively noticeable peaks at $Re = 10^4$ upstream of the vortex breakdown location in the St range between 1 and 3. In the occurrence of three-dimensional separated flow, relatively larger amplitude are detected close to the center of swirling pattern.
- Steady blowing through leading edge of the wing is quite effective in preventing three-dimensional surface separation at practical injection conditions.
- At $\alpha = 6^\circ$, increasing the momentum coefficient decreases the size of three-dimensional separated structure and once $C_\mu = 0.01$ is reached, successful generation of leading edge vortices is apparent. The successful

control is achieved at lower momentum coefficients compared to the studies at literature. In addition, although the flow control causes substantial changes in flow structure at $\alpha = 10^\circ$ for the tested momentum coefficients, it is still not sufficient to alter the flow structure from stall regime to leading edge vortex structure.

- Considering the wing surface from apex to the trailing edge, pressure distributions and smoke visualizations indicate that, the effect of flow control on flow structure reduces from apex to trailing edge, where it is the highest at the apex region and the lowest at the trailing edge region.

4.2. Recommendations for future work

Although the results presented here have demonstrated the effectiveness of active flow control technique, which is steady blowing through the leading edge of the wing, it could be further studied in the following ways:

- Velocity measurements are needed to be carried out with LDA velocity measurements at vortex core and near wing surface to ultimately compare the velocity spectra for the controlled case with the absence of control flow with the normal flow structure can be useful to better clarification of leading edge blowing effect on flow behavior. Moreover, Spectral analysis of pressure data can also be functional in exploring how the flow structure alters by applying flow control technique.
- Force-balance measurements can be conducted on the wing model to establish the correctness of the aerodynamic characteristics of the wing inferred from the flow field measurements carried out in the present study.
- Different blowing pattern with the same total momentum coefficient can be performed to understand whether it is possible to enhance the effect of leading edge blowing on flow structure particularly at high angles of attack.

- Unsteady leading edge blowing with more parameters could be considered in future studies. Moreover, shape of holes from which air is injected and their distances from the wing leading edge could also be investigated and compared with the current results.

REFERENCES

- [1] Williams, N. M., Wang, Z., & Gursul, I. (2008). Active flow control on a nonslender delta wing. *Journal of Aircraft*, 45(6), 2100-2110.
- [2] Gursul, I., Wang, Z., & Vardaki, E. (2007). Review of flow control mechanisms of leading-edge vortices. *Progress in Aerospace Sciences*, 43(7), 246-270.
- [3] Polhamus, E. C. (1971). Predictions of vortex-lift characteristics by a leading-edge suction analogy. *Journal of aircraft*, 8(4), 193-199.
- [4] Williams, N. M., "Active Flow control on a Nonslender Delta Wing", (PhD thesis, University of Bath, 2009).
- [5] Payne, F. M., Ng, T., Nelson, R. C., & Schiff, L. B. (1988). Visualization and wake surveys of vortical flow over a delta wing. *AIAA journal*, 26(2), 137-143.
- [6] Gursul, I. (2005). Review of unsteady vortex flows over slender delta wings. *Journal of Aircraft*, 42(2), 299-319.
- [7] Taylor, G. S., & Gursul, I. (2004). Buffeting flows over a low-sweep delta wing. *AIAA journal*, 42(9), 1737-1745.
- [8] Gordnier, R. E., & Visbal, M. R. (2005). Compact Difference Scheme Applied to Simulation of Low-Sweep Delta Wing Flow. *AIAA journal*, 43(8), 1744-1752.
- [9] Jin-Jun, W., & Wang, Z. (2008). Experimental investigations on leading-edge vortex structures for flow over non-slender delta wings. *Chinese Physics Letters*, 25(7), 2550.
- [10] Yavuz, M. M., & Rockwell, D. (2006). Identification and control of three-dimensional separation on low swept delta wing. *AIAA journal*, 44(11), 2805-2811.
- [11] Yaniktepe, B., & Rockwell, D. (2004). Flow structure on a delta wing of low sweep angle. *AIAA journal*, 42(3), 513-523.
- [12] Garg, A. K., & Leibovich, S. (1979). Spectral characteristics of vortex breakdown flowfields. *Physics of Fluids (1958-1988)*, 22(11), 2053-2064.
- [13] Gursul, I. (1994). Unsteady flow phenomena over delta wings at high angle of attack. *AIAA journal*, 32(2), 225-231.

- [14] Menke, M., Yang, H., & Gursul, I. (1999). Experiments on the unsteady nature of vortex breakdown over delta wings. *Experiments in Fluids*, 27(3), 262-272.
- [15] Gordnier, R. E., & Visbal, M. R. (2003). Higher-order compact difference scheme applied to the simulation of a low sweep delta wing flow. *AIAA paper*, 620.
- [16] Gursul, I., Gordnier, R., & Visbal, M. (2005). Unsteady aerodynamics of nonslender delta wings. *Progress in Aerospace Sciences*, 41(7), 515-557.
- [17] Lawford, J. A. (1966). Low-speed wind tunnel experiments on a series of sharp-edged delta wings. H. Majesty's Stationery Office.
- [18] Gad-el-Hak, M., & Blackwelder, R. F. (1985). The discrete vortices from a delta wing. *AIAA journal*, 23(6), 961-962.
- [19] Yavuz, M. M., Elkhoury, M., & Rockwell, D. (2004). Near-surface topology and flow structure on a delta wing. *AIAA journal*, 42(2), 332-340.
- [20] Farnsworth, J., Cannelle, F., Ciuryla, M., & Amitay, M. (2007). Control of the stingray UAV at low angles of attack. *AIAA paper*, 321, 2007.
- [21] Ol, M. V., & Gharib, M. (2003). Leading-edge vortex structure of nonslender delta wings at low Reynolds number. *AIAA journal*, 41(1), 16-26.
- [22] Taylor, G. S., Schnorbus, T., & Gursul, I. (2003). An investigation of vortex flows over low sweep delta wings. *AIAA paper*, 4021, 2003.
- [23] Lawson, M. V. (1964). Some experiments with vortex breakdown (Water tunnel flow visualization on slender delta wings reveal vortex breakdown formation to be a nonaxisymmetric stability). *ROYAL AERONAUTICAL SOCIETY, JOURNAL*, 68, 343-346.
- [24] Yavuz, M. M., & Rockwell, D. (2006). Control of Flow Structure on Delta Wing with Steady Trailing-Edge Blow. *AIAA journal*, 44(3), 493-501.
- [25] Ho, Steven. "Unsteady aerodynamics and adaptive flow control of micro air vehicles." PhD diss., University of California, Los Angeles, 2003.
- [26] Polhamus, E. C. (1971). Predictions of vortex-lift characteristics by a leading-edge suction analogy. *Journal of aircraft*, 8(4), 193-199.
- [27] Kohlman, D. L., & WENTZ, JR, W. H. (1971). Vortex breakdown on slender sharp-edged wings. *Journal of Aircraft*, 8(3), 156-161.
- [29] Lamar, J. E., & Campbell, J. F. (1984). Vortex flaps-advanced control devices for supercruise fighters.

- [30] Spedding, G. R., Maxworthy, T., & Rignot, E. (1987, July). Unsteady vortex flows over delta wings. In Proc. 2nd AFOSR Workshop on Unsteady and Separated Flows. Colorado Springs (Vol. 283, p. 288).
- [31] Deng, Q., & Gursul, I. (1996). Effect of leading-edge flaps on vortices and vortex breakdown. *Journal of aircraft*, 33(6), 1079-1086.
- [32] Yang, H., & Gursul, I. (1997). Vortex breakdown over unsteady delta wings and its control. *AIAA journal*, 35(3), 571-574.
- [33] Hong, J. S., Celik, Z. Z., & Roberts, L. (1996). Effects of leading-edge lateral blowing on delta wing aerodynamics. *AIAA journal*, 34(12), 2471-2478.
- [34] Margaritis, P., & Gursul, I. (2004). Effect of steady blowing on wing tip flowfield. In 2nd AIAA Flow control conference (pp. AIAA-2004). University of Bath.
- [35] Celik ZZ, Roberts L. Vortical flow control on a delta wings by lateral blowing. AIAA 94-0509, 32nd aerospace sciences meeting and exhibit, January 10–13, 1994, Reno, NV.
- [36] Wood, N. J., & Roberts, L. (1988). Control of vortical lift on delta wings by tangential leading-edge blowing. *Journal of Aircraft*, 25(3), 236-243.
- [37] Greenwell, D. I., & Wood, N. J. (1994). Roll moment characteristics of asymmetric tangential leading-edge blowing on a delta wing. *Journal of aircraft*, 31(1), 161-168.
- [38] Mitchell, A. M., & Délerly, J. (2001). Research into vortex breakdown control. *Progress in Aerospace Sciences*, 37(4), 385-418.
- [39] Gu, W., Robinson, O., & Rockwell, D. (1993). Control of vortices on a delta wing by leading-edge injection. *AIAA journal*, 31(7), 1177-1186.
- [40] Johari, H., Olinger, D. J., & Fitzpatrick, K. C. (1995). Delta wing vortex control via recessed angled spanwise blowing. *Journal of aircraft*, 32(4), 804-810.
- [41] McCormick, S., & Gursul, I. (1996). Effect of shear-layer control on leading-edge vortices. *Journal of aircraft*, 33(6), 1087-1093.
- [42] Campbell, J. F. (1976). Augmentation of vortex lift by spanwise blowing. *Journal of Aircraft*, 13(9), 727-732.
- [43] Bradley, R. G., & Wray, W. O. (1974). A conceptual study of leading-edge-vortex enhancement by blowing. *Journal of aircraft*, 11(1), 33-38.
- [44] Guillot, S., Gutmark, E. J., & Garrison, T. J. (1998). Delay of vortex breakdown over a delta wing via near-core blowing. *AIAA Paper*, 98-0315.

- [45] Mitchell, A. M., Barberis, D., Molton, P., Dé, J., & Iery. (2000). Oscillation of vortex breakdown location and blowing control of time-averaged location. *AIAA journal*, 38(5), 793-803.
- [46] Phillips, S., Lambert, C., & Gursul, I. (2003). Effect of a trailing-edge jet on fin buffeting. *Journal of aircraft*, 40(3), 590-599.
- [47] Wang, Z. J., Jiang, P., & Gursul, I. (2007). Effect of thrust-vectoring jets on delta wing aerodynamics. *Journal of Aircraft*, 44(6), 1877-1888.
- [48] Tropea, C., Yarin, A. L., & Foss, J. F. (Eds.). (2007). *Springer handbook of experimental fluid mechanics* (Vol. 1). Springer.
- [49] Dantec Dynamics. "Laser Optical Measurement Systems and Sensors." Accessed September 21, 2014. <http://www.dantecdynamics.com/measurement-principles-of-lda>.
- [50] Saragiots, C., "Lomb normalized periodogram." Accessed September 10, 2013. <http://www.mathworks.com/matlabcentral/fileexchange/22215-lomb-normalized-periodogram>.
- [51] Fox, R. W., McDonald, A. T., & Pritchard, P. J. (2006). *Introduction to fluid mechanics*. John Wiley & Sons.
- [52] Kline, S. J., & McClintock, F. A. (1953). Describing uncertainties in single-sample experiments. *Mechanical engineering*, 75(1), 3-8.